UNIVERSITY OF SOUTHAMPTON

FACULTY OF PHYSICAL SCIENCES AND ENGINEERING

Optoelectronics Research Centre

Semiconductor Waveguides for Mid-infrared Photonics

by

Li Shen

Thesis for the degree of Doctor of Philosophy

December 2015

UNIVERSITY OF SOUTHAMPTON

ABSTRACT

FACULTY OF PHYSICAL SCIENCES AND ENGINEERING
Optoelectronics Research Centre

Doctor of Philosophy

SEMICONDUCTOR WAVEGUIDES FOR MID-INFRARED PHOTONICS

by Li Shen

Mid-infrared semiconductor photonics is an emerging field with wide ranging applications. One stream of research is focused on extending the well-developed silicon-based waveguide platforms into longer wavelength regimes because of the inherent transparency window of silicon in the mid-infrared regime as well as its favourable nonlinear properties. Alternative approach is to investigate the optical properties of new materials (i.e. germanium) that offer favourable properties such as broader transparency windows and large nonlinearities, etc.

In this thesis, two types of novel mid-infrared waveguide platforms were investigated. The first was the semiconductor optical fibres, an innovative platform that incorporates the functional semiconductors within the robust fibre geometry. A range of different core materials were characterised from the telecommunications band into the mid-infrared regime including polycrystalline silicon, hydrogenated amorphous silicon and hydrogenated amorphous germanium. Particularly, the large nonlinearity of the hydrogenated amorphous silicon core fibres was measured systematically cross this wavelength regime previously unknown for these fibres. With the knowledge of the key nonlinear parameters including nonlinear absorption and refraction, supercontinuum generation was demonstrated in the mid-infrared where the two-photon absorption was negligible. The measurements in the mid-infrared represent the first characterisation of the material beyond 1.55 μm.

The second platform was the germanium on silicon waveguides, which can be fabricated using similar techniques to the silicon integrated waveguides and are thus compatible with the widely used complementary metal-oxide-semiconductor platform. The results presented in this thesis represent the first comprehensive linear and nonlinear transmission loss characterisations of this new class of waveguide for selected mid-infrared wavelengths. By exploiting the free carriers and two-photon absorption mechanisms, high speed all-optical modulation was demonstrated across selected mid-infrared wavelengths.

Contents

List of Figures

List of Tables

Declaration of Authorship

I, Li Shen , declare that the thesis entitled *Semiconductor Waveguides for Mid-infrared Photonics* and the work presented in the thesis are both my own, and have been generated by me as the result of my own original research. I confirm that:

- this work was done wholly or mainly while in candidature for a research degree at this University;
- where any part of this thesis has previously been submitted for a degree or any other qualification at this University or any other institution, this has been clearly stated;
- where I have consulted the published work of others, this is always clearly attributed;
- where I have quoted from the work of others, the source is always given. With the exception of such quotations, this thesis is entirely my own work;
- I have acknowledged all main sources of help;
- where the thesis is based on work done by myself jointly with others, I have made clear exactly what was done by others and what I have contributed myself;
- parts of this work have been published as: See List of Publications

Signed:.....

Date:.....

Acknowledgements

Here I shall acknowledge a few people who have contributed to this thesis and my growth throughout the whole PhD journey. Time goes by fast, I am sincerely grateful for the help, encouragement and support form my colleagues, friends and beloved family members during the past four years PhD study at Optoelectronics Research Centre. It has been fantastic for working and living with your guys, I shall work on with the valuable knowledge and precious experience gained here for the rest of life.

Firstly, I thank my supervisors Prof. Anna Peacock and Dr. Noel Healy. I am grateful as I am the luck person whom was given the precious opportunity to study in the ORC and provided such an interesting project with trust. Four years ago everything was fresh to me when I came to the UK. It was the first time that me a boy born in a small town travelled thousands of miles away from my homeland. I had no idea about the new project and a little frustrating in the beginning. I thank your helpful guidance and encouragement. I can't forget that Anna taught me how to solve the linear partial differential equation after 7pm and Noel trained me the experimental skills again and again. I thank Dr. Priyanth Mehta my labmates for your kind help during the first two years of my PhD. Dr. Noel Healy and Dr. Priyanth Mehta taught me how to prepare a silicon fibre for test and launch the beam into the micro-size fibre core as the starting skill for my PhD project. They have also generously been my urgent supply for lab necessities and helped me solve thousands of problems in my experiments very timely.

I would like to thank my group colleagues: Dr. Natasha Vukovic, Dr. Limin Xiao, Fariza Hanim Suhailin, and Haojie Zhang. They have taught me knowledge and skills, offered me suggestions on my project, given me a hand in the lab, and shared equipment with me. Thank you so much guys. I gratefully thank colleagues in the Silicon Photonics group for providing me silicon and germanium chips, teaching me basic skills about silicon photonics, and generously giving me access to their lab resources: Prof Graham Reed, Dr Goran Mashanovich, Dr David Thomson, Dr Colin Mitchell, Dr Milos Nedeljkovic, and Jordi Soler Penades. I would like to thank my colleages and friends in the ORC: Dr. Ping Hua, Dr. Sima Chaotan, Dr. Xin Yang, Dr. Alexander Heidt, Dr. Yongmin Jung, Dr. Zhixin Liu, Dr. Yutong Feng, Dr. Jin Yao, Dr. Eric Numkam, Dr. Lin Xu, Dr. Zhihong Li, Dr. Qian Wang, Dr. Jing He, Mr. Di Lin, Ms. Qiongyue Kang, Mr. Jingyu Zhang, Ms. Meng Zhang and Mr. Zilong Wang. They have given me useful suggestions on my project, helped me in the lab, and kindly loaned equipment with me. Thank you guys for accompanying me during the past four years.

I gratefully thank the ORC and the China Scholarship Council, who have provided me with the studentship that has allowed me to pursue my PhD degree.

Last but not least, I thank my family: my parents Xianhong Shen and Lilin Cheng, for giving birth to me and bringing me up. I am grateful that you are the kindest parents of the world who always support and encourage me throughout my life. Special thanks are dedicated to my wife Yuanhao Wu for your endless love and understanding, which is beyond words but is my forever motivation to move on. I understand it is really not easy for you in the past four years as most of time I could not accompany with you but it is you made the best time of my life.

The last word of acknowledgement I have saved for all my friends who have been with me all these years and made my life better. Wish everyone all the best for the future.

Nomenclature

3PA	three-photon absorption
a-a	allowed-allowed
a-f	allowed-forbidden
a-Ge:H	hydrogenated amorphous germanium
a-Si	amorphous silicon
a-Si:H	hydrogenated amorphous silicon
BESOI	bond and etch-back silicon-on-insulator
BOX	buried oxide
CMOS	complementary metal-oxide-semiconductor
c-Si	crystalline silicon
CVD	chemical vapour deposition
CW	continuous wave
e-beam	electron-beam
FCA	free carrier absorption
FCD	free carrier dispersion
FEM	finite element method
f-f	forbidden-forbidden
FOM	figure of merit
FWHM	full width half maximum
FWM	four-wave mixing
Ge-on-Si	germanium-on-silicon
GVD	group-velocity dispersion
HPCVD	high pressure chemical vapordeposition
LA	longitudinal acoustic
LCD	liquid-crystal display
LO	longitudinal optical
LTD	low temperature drawing
MCD	molten core drawing
MI	modulation instability
mid-IR	mid-infrared
MMI	multimode interference
MPA	multiphoton absorption

NA	*numerical aperture*
NLSE	nonlinear Schrödinger equation
NRZ	non-return-to-zero
OEO	optical-electronic-optical
OOK	on-off-keying
OPO	optical parametric oscillator
PAPF	pressure assisted physical filling
PbSe	lead selenide
PCF	photonic crystal fibre
PIT	powder-in-tube
p-Si	polycrystalline silicon
QCL	quantum cascade laser
RIE	reactive ion ecthing
RMS	root mean square
RZ	return-to-zero
SEM	scanning eletron microscopes
SHIM	scanning helium ion microscope
SIMOX	separation by implanted oxygen
SiPSi	silicon-on-porous
SOI	silicon-on-insulator
SOS	silicon-on-sapphire
SPM	self-phase modulation
SRH	Shockley-Read-Hall
TD	threading dislocation
TE	transverse mode
THG	third harmonic generation
TM	transverse magnetic
TO	transverse optical
TPA	two-photon absorption
WDM	wavelength-division multiplexing
XAM	cross-absorption modulation
XPM	cross-phase modulation
ZDW	zero-dispersion wavelength
ZnSe	zinc selenide

Chapter 1

Introduction

1.1 Introduction to semiconductor photonics

Semiconductors are a group of materials having electrical conductivities intermediate between metals and insulators. These materials, principally those of group-IV elements or III-V compounds, have dominated the microelectronic industry for the past half century. This is largely due to the fact that the conductivity of these materials can be varied over orders of magnitude by changes in temperature, optical excitation and impurity content. Devices based on semiconductor materials have revolutionized the electronics industry and changed our daily lives, finding use in functional devices such as computers, mobile phones etc. The exponential growth of the internet bandwidth means that developments in the microelectronics industry can just about follow Moore's Law by employing multicore structures and scaling more transistors on a single chip. However, the optical communication network is suffering from an electronic bottleneck of high speed data transmission and processing due to large amount of optical-electronic-optical (OEO) conversion devices throughout the whole network. One possible solution is to create an all-optical network eliminating OEO conversion regenerators in conventional networks, thus greatly increasing the network speed. All-optical networks require high-performance optoelectronic devices that can emerge photonics and microelectronics seamlessly [1]. These devices must have the capabilities of optical signal processing, for example, optical interconnects and routers, as well as decent optical waveguiding properties. From this point of view, semiconductor photonics which uses semiconductor materials as an optical medium has the potential to integrate optical and electronic components onto a single chip and provide optical interconnection between neighboring components, eventually may leading to all-optical network systems.

Soref and Petermann produced much of the pioneering work in the late 1980s and early 1990s to introduce semiconductor materials to photonics. This work, and many of the subsequent efforts, mainly focused on passive waveguides, switches, and modulators

[1, 2, 3, 4]. Continuous advancements in this interesting research area have been achieved since late 1990s. A large number of optoelectronic devices have been demonstrated by different research groups in silicon photonics, e.g. passive waveguides, modulators, filters, integrated photodiodes, lasers and amplifiers, etc [5, 6, 7]. Semiconductor materials like silicon have a transparency window covering a wide range of wavelengths from the near-infrared to the mid-infrared (mid-IR), and exhibit many excellent optical properties including large optical damage thresholds, tunable free carrier effects and strong optical nonlinear effects. Compared with the most commonly used silica waveguides, semiconductor materials have larger refractive indices so that when clad in low index materials such as silica, the optical mode size of the waveguide can be scaled down to nanometer dimensions ($< 1\,\mu\mathrm{m}^2$). This is useful when developing nonlinear signal processing devices such as all-optical regenerators.

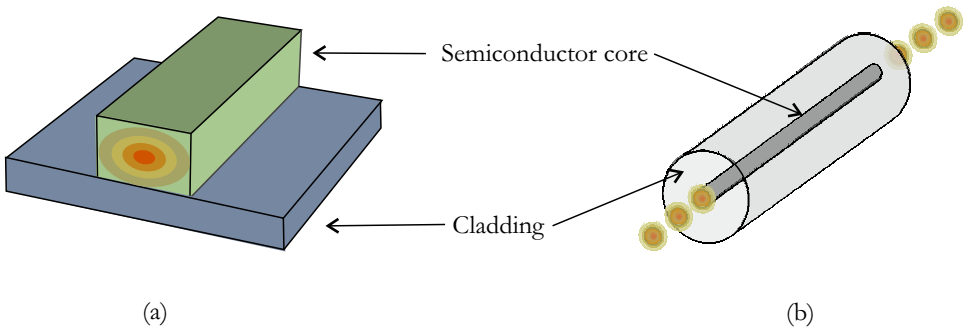

Figure 1.1: Schematic diagrams for two types of semiconductor waveguides primarily investigated in this thesis, (a) semiconductor rectilinear waveguide and (b) semiconductor core optical fibre.

In the past few decades, most of the semiconductor photonics research has been based on silicon rectilinear waveguides in the near infrared wavelength region, and in particular telecom wavelengths. Commercial products employing these devices including active optical cables (Luxtera) and variable optical attenuators (Kotura) have been released to the market. Complementing this research, a new class of semiconductor core optical fibres has emerged, which could provide an elegant route to unify the semiconductor materials with the glass fibre infrastructures used in telecom systems. Figure 1.1 compares and contrasts these two types of optical waveguide fabricated with semiconductor core materials. Though silicon is currently the favoured material of choice for semiconductor photonics in the telecoms region, other materials are emerging as interesting candidates for other wavelength regions, such as the mid-IR. For this project, both silicon and germanium are investigated as they have high optical nonlinearity and cover important wavelength regions. Germanium has been chosen in this project because of its longer mid-IR transmission window and high nonlinearity as well as its compatibility with existing fabrication techniques.

1.2 Mid-infrared group-IV semiconductor photonics

The mid-IR regime (2 to 20 μm) covers both atmospheric transmission windows (3 − 5 μm and 8 − 12 μm) and the material "fingerprint region" for various chemical and biological molecules. Thus it is proving to be very important for a wide range of applications including sensing, medical diagnostics, free space communications, thermal imaging, and infrared countermeasures [8]. The short-wave infrared between 2 to 3 μm is the most interesting spectral regime for nonlinear silicon optics as this is beyond the nonlinear TPA region, before the nonlinear refractive index drops. Moreover, the well-established silicon-on-insulator (SOI) platform can still be used in this wavelength regime [9, 10]. This short-wave infrared wavelength regime has recently emerged a strong candidate for the next generation communication system [11]. Current research work is focusing on transferring existing technologies developed for the near infrared to the mid-IR by modifying the waveguide design and seeking new material composition e.g. sapphire, germanium [12, 13].

Both silicon and germanium have a good optical transparency in the mid-IR (up to 7.8 μm for silicon and 14 μm for germanium) and can exhibit strong nonlinear optical effects [14]. Semiconductor optical fibres of which the core is made from silicon or germanium are only able to support wavelengths up to 3.6 μm due to strong absorption of the silica cladding beyond this wavelength. The germanium-on-silicon (Ge-on-Si) waveguides structure is similar to that illustrated in Figure 1.1(a). The top layer is the germanium core and the bottom cladding layer is made of silicon. This Ge-on-Si waveguide has an even boarder transmission window up to 8 μm. Thus these two semiconductor waveguides platforms are promising for mid-IR applications and are chosen as the main investigate focus of this project.

Nonlinear effects in semiconductor materials (mainly in silicon) could be exploited for numerous applications within in the mid-IR regime in areas such as signal processing, sensing and biologic imaging [15]. Since nonlinear processes require high peak power, they are often investigated using short pulses. Owning to their high refractive index, semiconductor waveguides typically offer tight light confinement and enhanced nonlinearities, it is possible to observe nonlinear effects over short waveguide lengths and with low powers. These have been largely unexplored in the mid-IR. Hence, this project presents the first comprehensive study of the novel mid-IR waveuides made from semiconductor materials. Linear and nonlinear characterizations were performed for two proposed semiconductor waveguides from near infrared to the mid-IR and applications such as all-optical modulation, parametric amplification and supercontinnum have been demonstrated.

1.3 Thesis outline

Chapter 1 presents the background and motivation of this PhD project. It outlines the thesis structure, summarises the key achievements of this PhD study, details my contributions, and acknowledges valuable help I received during the experiments and thesis writing.

Chapter 2 reviews the state of the art regarding semiconductor waveguides in the literature. Different fabrication techniques of semiconductor core optical fibre are introduced and the basic optical properties of semiconductor core optical fibres are described. Various group IV material platforms are also reviewed with their advantages and disadvantages in the mid-IR regime. This chapter also summarises the recent progress on the nonlinear applications of these mid-IR waveguides.

Chapter 3 provides a theoretical foundation for the semiconductor waveguides investigated in this PhD work. Topics include the material properties and optical effects which must be considered in all applications of semiconductor waveguides. It begins with the theoretical background that describes optical pulse propagation in the semiconductor waveguides, accounting for the linear loss, nonlinear absorption, dispersion and particularly the effects of free carriers which is unique in semiconductors. The equations associated with these parameters are used for the simulations to analyse the experimental characterizations in the following chapters.

Chapter 4, 5 and 6 are at the heart of this thesis. Presented in these chapters are the experimental measurements of the material properties and transmission characteristics of novel silicon and germanium optical waveguides from the near infrared to the mid-IR regime. The two most commonly developed types of semiconductor waveguides: fibres and planar waveguides are presented and characterised for different wavelengths extending to the mid-IR region. The material quality of the waveguides are characterised by scanning electron microscopes (SEM) and Raman spectroscopy measurements. For semiconductor core optical fibres, this thesis focuses on the fibres of which the core is comprised of silicon or germanium. The linear optical properties of a range of fibres are measured and compared against the different core materials and deposition conditions. For the planar waveguide, most efforts are focused on developing a germanium waveguide platform for the mid-IR wavelength regime. The Ge-on-Si waveguides are proposed and compared with the existing mid-IR waveguide platforms.

Chapter 5 extends the investigations of nonlinear properties of silicon core fibres to the mid-IR regime. In this chapter, the comprehensive numerical and experimental detail are discussed including the nonlinear absorption and refraction in the silicon optical fibres. Through numerical fitting of the experimental data with the modified nonlinear Schrödinger equation and free carriers rate equation, the nonlinear absorption and refractive index coefficients are determined. A nonlinear figure of merit is used to

compare silicon fibres with other silicon waveguides to highlight the advantages of the use in the mid-IR regime. By exploiting the high nonlinearity in the mid-IR regime, supercontinuum generation was demonstrated in a a-Si:H core fibre with small core size (1.7 μm).

Chapter 6 investigates the nonlinear absorption in Ge-on-Si waveguides and presents a systematic study across the two-photon absorption (TPA) edge. The nonlinear absorption coefficients are determined via a similar fitting method previously used for the silicon core fibre. The large nonlinear absorption is exploited to demonstrare all-optical modulation in the novel Ge-on-Si waveguides at mid-IR wavelengths via both free-carrier absorption (FCA) and TPA.

Finally, Chapter 7 summarises the work over the PhD period and outlines future experimental possibilities to follow the work presented in this report. Semiconductor waveguide fabrication, linear optical characterisations, nonlinear absorption and refraction measurements, supercontinuum generation and mid-IR all-optical modulation formed the main part of the thesis.

1.4 Key achievements

Here lists a brief summary of the key achievements during the author's PhD study:

1. The linear and nonlinear transmission properties of hydrogenated amorphous silicon (a-Si:H) core fibres are characterized from the near infrared up to the edge of the mid-IR regime. The results show that this material exhibits linear losses in the range of $0.3 - 7\,\mathrm{dB/cm}$, over the entire wavelength range (1.5 - 2.7 μm). By measuring the dispersion of the nonlinear Kerr and TPA parameters we have found that the nonlinear figure of merit ($\mathrm{FOM_{NL}}$) increases dramatically over this region.

2. Demonstration of an octave-spanning supercontinuum in a a-Si:H core fibre when pumped in the mid-IR regime. The broadband supercontinuum extends from the edge of the telecommunications band into the mid-IR (1.64 - 3.37 μm).

3. The linear transmission properties of Ge-on-Si waveguide are characterized from the band edge up to the mid-IR regime. The results show that this waveguide exhibits low linear losses in the range of $2.5 - 6\,\mathrm{dB/cm}$, over the broad mid-IR wavelength range from 2 - 3.8 μm.

4. Demonstration of first all-optical modulation in a Ge-on-Si rib waveguide over the mid-IR wavelength range of 2 - 3.2 μm using a FCA scheme with a modulation depth of $\sim 5\,\mathrm{dB}$ and a response time $< 18\,\mathrm{ns}$.

5. The nonlinear absorption properties of a Ge-on-Si waveguide have been characterized across the TPA transmission window. Exploiting the large nonlinear absorption near the bandedge, ultrafast all-optical modulation is achieved with a modulation depth of $\sim 8\,\mathrm{dB}$ and a response time $< 5\,\mathrm{ps}$.

1.5 Contributions and acknowledgements

The author is responsible for all the work presented in this thesis under the supervision of Prof. Anna Peacock and Dr. Noel Healy.

Fabrication of the semiconductor core optical fibres in Chapter 4 were performed at Pennsylvania State University by Dr. Todd Day, Hiu Yan Cheng and Subhasis Chaudhuri. The optical microscope images, the a-Si:H Raman measurements, and optical transmission measurements were performed by myself with the assistances from Dr. Noel Healy and Dr. Priyanth Metha. For the supercontinuum generation presented in Chapter 5, Dr. Lin Xu has assisted me during the experiments.

Fabrication of the Ge-on-Si waveguides used in this thesis were performed by Dr. Milos Nedeljkovic, Dr. Colin Mitchell and Jordi Soler Penades. The SEM images of germanium-on-silicon waveguide were taken by Dr Colin Mitchell. Part of the linear transmission measurements in Ge-on-Si were performed by Jordi Soler Penades. The thulium doped fibre amplifier used in Chapter 6 was built and provided by Dr. Alexander Heidt and Dr. Zhihong Li. Dr. Shaiful Alam, Dr. Radan Slavík and Dr. Yutong Feng have provided $2\,\mu$m semiconductor diode lasers and driver mount. The lock-in detection system was built by myself with assistance from Dr. Priyanth Mehta and Dr. Noel Healy.

The general MATLAB code structure for the simulation analysis in this thesis was provided by Prof. Anna Peacock and modified by myself for the different material systems and new waveguide designs. Simulations of the simplified coupled-mode equations were coded by Dr. Priyanth Mehta initially for the silicon core fibre and modified by myself for the use in the Ge-on-Si waveguides.

Chapter 2

Literature review

2.1 Introduction

In this chapter, a brief introduction to the group IV semiconductor waveguides is given. Silicon and germanium, the waveguide materials used in this thesis, are discussed from the fundamental optical properties through to devices. The chapter also reviews the recent progress in the nascent field of semiconductor waveguides for the mid-infrared (mid-IR) wavelength regime. Various mid-IR waveguide platforms are introduced and typical nonlinear applications based on these platforms are given to indicate the potential use in this increasingly important region.

2.2 Basic optical properties of silicon and germanium

Silicon and germanium offer rich optoelectronic functionality. Furthermore, compared to silica that is mostly used for optical fibres, they also have desirable properties such as broad transmission windows as well as high optical nonlinear susceptibilities. They are also compatible with many existing fabrication approaches and hence they are currently the favoured materials for the group IV photonics applications. Figure 2.1 is a comparison of the optical transmission in silicon and germanium with silica shown as a reference. This section presents a brief discussion of the material characteristics of silicon and germanium. Figure 2.2 shows the refractive indices of these materials as a function of wavelength which all show a slight decrease with an increase of the wavelength. The corresponding coefficients for the two semiconductors and the silica material used for the calculation are from Frey *et al.* and Barnes *et al.* [16, 17].

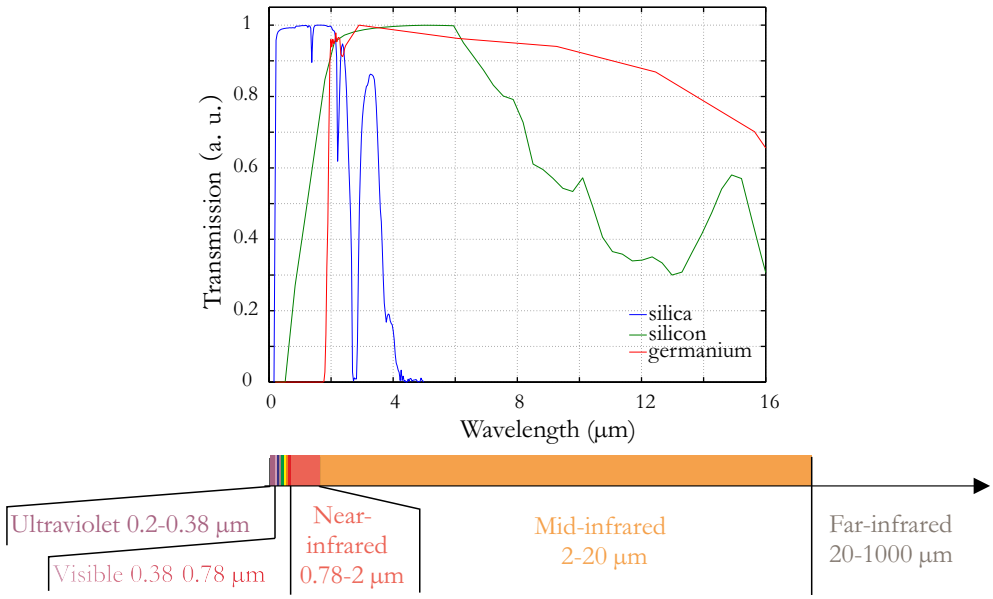

Figure 2.1: Transmission profiles of silica (blue), silicon (green), and germanium (red).

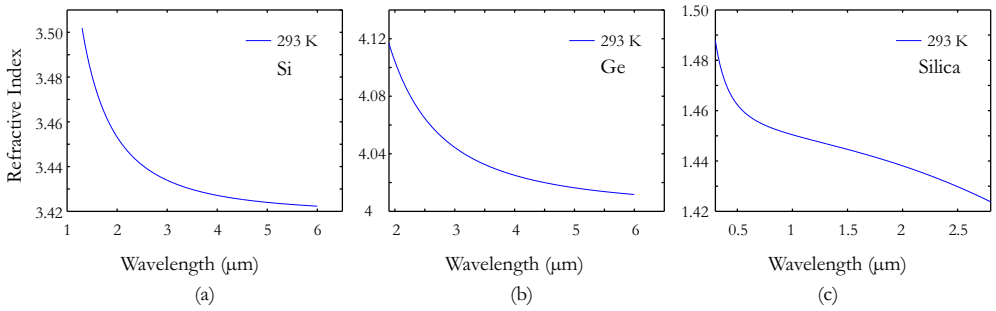

Figure 2.2: Refractive index of (a) silicon, (b) germanium, and (c) silica as a function of wavelength.

2.2.1 Silicon

Silicon is the seventh most abundant element in the universe and the second most abundant element in the earth's crust. It was first isolated by Jöns Jacob Berzelius in 1823 by heating chips of potassium in a silica container and then carefully washing away the residual by-products. Silicon is becoming one of the most popular semiconductor material for photonics applications in the near infrared wavelength regime. Much of this interest stems from the well-established fabrication facilities that exist due to the large investment on silicon microprocessors. However it also has favourable optical properties such as a wide transparency window (1.3 - 7.8 μm), high damage threshold, and large third order nonlinearity $\chi^{(3)}$ (around a hundred times larger than that of silica). As the bandgap energy of crystalline silicon is 1.12 eV, the telecommucation wavelengths is located in its low transmission window, thus making it suitable for photonics applications

at these wavelengths. As shown in Figure 2.2, silicon has a higher refractive index than that of silica, which is the favoured cladding material, so the light is confined tightly in the core area due to the high index contrast. These properties makes silicon a very useful material for wide ranging nonlinear applications. Following the first demonstration of Raman amplification by Jalali's group in 2003 [18], most of the important nonlinear processes around the telecommunication band including supercontinuum generation [19], wavelength conversion [20], and parametric light amplification [21] have been extensively investigated in this material.

Amorphous silicon (a-Si) is the non-crystalline form of silicon. As it is cheap and easy to fabricate, it has been used for solar cells and thin-film transistors in liquid-crystal display (LCD) displays. Although a-Si has high optical loss due to the dangling bonds associated with its disordered nature, these can be passivated via the incorporation of hydrogen [22]. Hence, hydrogenated-amorphous silicon (a-Si:H) has much lower optical loss compared with amorphous silicon. Thus, a-Si:H is emerging as an alternate material for the integration of silicon photonics. In addition, compared to crystalline silicon, a-Si:H has many advantages such as a higher Kerr nonlinear coefficient n_2, low fabrication costs and a larger bandgap energy [23]. The band edges of a-Si:H have extended tails and the band gap energy is commonly estimated to be $E_g = 1.7\,eV$. This is because the Si-H bond has a higher binding energy than the Si-Si bond, so that the average binding energy of the hydrogenated material is larger than that of pure silicon [24]. The larger bandgap suggests that the nonlinear absorption should be comparatively modest at telecom wavelengths which is important for many nonlinear applications. In the past few years, a-Si:H has been demonstrated as a very promising material for nonlinear optics based applications in both photonic chips and optical fibres for the telecom wavelength [25, 26, 27, 28].

2.2.2 Germanium

Germanium was discovered in 1885 by Clemens Winkler who named the element in the honor of his homeland, Germany. As the bandgap energy of germanium is 0.67 eV, the optical transmission of germanium starts from $1.9\,\mu m$ but extends well into the mid-IR which is shown in Figure 2.1. Figure 2.2(b) shows the refractive index of germanium as a function of wavelength, from which it can be seen the refractive index of germanium is larger than 4 up to $6\,\mu m$. Also, germanium has a larger third order nonlinear susceptibility (four times than that of silicon), when combined with the tight mode confinement, Ge-on-Si is a suitable waveguide platform to explore various nonlinear optical devices for the mid-IR wavelength regime [29]. Compared to silicon, it has an even higher refractive index, allowing for tighter mode confinement. In addition to the silica clad germanium waveguides (germanium optical fibre and planar germanium on insulator waveguide),

germanium-on-silicon (Ge-on-Si) waveguides can also be constructed because the refractive index of germanium is higher than silicon, thus enabling wave guiding. It is due to these excellent properties that germanium is considered for nonlinear application in the mid-IR. Since the goal of this thesis is to evaluate the suitable semiconductor waveguide platform for mid-IR photonics, germanium core fibre and Ge-on-Si waveguides are chosen as two examples that could allow for transmission to longer wavelengths, with detail descriptions being presented in the following chapters.

2.3 Semiconductor optical fibres

The first example of semiconductor core optical fibre was demonstrated in 2006 by a collaboration between researchers from the Pennsylvania State University and the Optoelectronics Research Centre at the University of Southampton (PSU/ORC). To fabricate this fibre this team used a high pressure chemical vapour deposition (HPCVD) method to fill semiconductors into silica fibre templates with air-holes inside [30]. This techniques is very flexible and a variety of semiconductor optical fibres have been fabricated from both elemental semiconductors, such as silicon and germanium [31], as well as compound semiconductors like zinc selenide (ZnSe) [32]. This technique has also been extended to fabricate microstructure fibres by filling semiconductor material into a variety of silica templates with different dimensions [33]. Following this pioneering work, other approaches have been applied to fabricate semiconductor core fibres by research groups from the Max Planck Institute for the Science of Light (Germany), Clemson University (US) and Norwegian University of Science and Technology, Virginia Polytechnic Institute (US) and Massachusetts Institute of Technology (US). This section presents a brief summary of these fabrication methods and discusses the basic materials and optical properties of various semiconductor core optical fibres.

The molten core drawing (MCD) technique was developed by the Ballato group at Clemson University. In this method a rod of single crystal or polycrystalline semiconductor is sleeved inside a silica cladding to fabricate the semiconductor fibre preform [34, 35, 36, 37]. The preform is then drawn into fibre using a conventional fibre draw tower at the silica glass transition temperature, which is above the typical melting points of the semiconductor core materials (1414 °C for silicon and 938 °C for germanium). This drawing technique can be used to fabricate long lengths of semiconductor optical fibre, but the minimum obtainable core sizes are limited to be of the order of tens of microns, which is due to the significant diffusion of oxygen from the silica into the semiconductor material ($> 60\%$) during the high temperature drawing process. Using this method the group has fabricated optical fibres with group IV semiconductors and III-V compound core materials. For example, a silicon core fibre drawn to have a core diameter of approximately 60 μm and length of 30 m was reported to have linear transmission loss of 2.7 dB/cm at 1.53 μm and very low loss value of 4.3 dB/m at 2.94 μm in the mid-IR.

To date, this method has also produced the record lowest loss of the germanium core fibres, with a value of 0.7 dB/m measured at 3.39 μm in a large core diameter of 300 μm. The current focus of this research group is to find more appropriate glass compositions (e.g. chalcogenide) for use as cladding materials that offer better compatibility with the molten semiconductors to compensate the thermal mismatch and reduce the losses further [38, 39]. It is worth noting that further optimization to the MCD technique was applied by introducing alkaline-earth interface modifiers as reactive diffusion barriers between the silica cladding and the semiconductor core. This allowed for the fabrication of fibres with core diameters down to 10 μm and optical losses below 4 dB/cm at 1.55 μm by a research group from Norwegian University of Science and Technology [40].

The Russell group at the Max Planck Institute developed a method to selectively fill the holes in microstructure fibres using a pressure assisted physical filling (PAPF) method [41]. The first example of this technique was the photonic crystal fibre (PCF) with integrated micron-sized germanium wire. In this fabrication process, pure germanium was pumped into the selected holes of a PCF at a pressure of $\sim$ 6 MPa and a temperature of $\sim$ 1000 °C. Using this technique, semiconductor core optical fibres of up to a few centimetres long can be achieved with core sizes of a few microns. The particular example of the Ge-PCF was shown to exhibit strongly polarization dependent transmission losses, with extinction ratios as high as 30 dB. However, the light guiding in this waveguide was actually in the silica.

The Pickrell group from Virginia Polytechnic Institute demonstrated a silicon fibre using a method similar to MCD called the powder-in-tube (PIT) method [42]. The silicon fibre was draw from a preform made by densely packing silicon powder into silica tubes with millimetre internal diameters. The fibres could be fabricated over length scales on the order of centimetres, with core diameters from tens of micrometres to a few hundred micrometres. As with MCD case, this method also suffered from defects at the silicon-silica boundaries along the fibre length due to the thermal mismatch between materials. It is worth noting that the PIT method was the first to fabricate n-doped (phosphorus) silicon core optical fibres by using doped silicon powder as a starting material [43]. The lowest transmission losses reported were more than 250 dB/cm at 1.5 μm for doped silicon core. This is not surprising as doped material will absorb more light than intrinsic material.

Researchers from the Fink group at Massachusetts Institute of Technology have applied the low temperature drawing (LTD) approach to fabricate amorphous chalcogen-semiconductors with other low melting temperature materials. This method has been applied to fabricate several long fibre structures and devices with unique optical [44], electrical [45], thermal [46], and acoustic functionality [47]. For example, a fibre has been fabricated which could be used to deliver optical power at 10.6 μm for medical applications [48]. It is also worth to note that the Fink Group has recently developed preform-to-fibre fabrication technique using the redox reaction between aluminum (Al)

Material	Wavelength (μm)	Loss value (dB/cm)	Core diameter (μm)	Group
a-Si:H	1.55	0.8	6	PSU/ORC [50]
p-Si	1.3	2.7	150	Clemson [34]
p-Si	2.2	0.99	6	PSU/ORC
p-Si	2.94	0.043	50	Clemson [34]
p-Si	1.55	4.0	10	NTNU [40]
d-Si	1.55	250	15	Virgina [42]
a-Ge:H	2.7	10	6	PSU/ORC
c-Ge	3.39	0.7*	300	Clemson [51]

Table 2.1: Comparison of lowest measured losses and corresponding core size reported in the literature. Hydrogenated amorphous silicon, a-Si:H; polycrystalline silicon, p-Si; doped silicon, d-Si; hydrogenated amorphous germanium, a-Ge:H; crystalline germanium, c-Ge. Abbreviations: Collaboration between the Pennsylvania State University and the Optoelectronics Research Center at the University of Southampton (PSU/ORC), Clemson University (Clemson), Norwegian University of Science and Technology (NTNU), Virginia Polytechnic Institute (Virginia). The linear loss unit for C-Ge is in [dB/m].

and silica (SiO_2) [49]. The preform consists of one piece of Al wire (3 cm long, 250 μm diameter) placed inside a silica tube. The preform with the Al core is then heated up to 2200 °C in Argon atmosphere and pulled into metre-long fibres with outer diameters of $\sim$ 500 μm. During the fibre draw, Al melts and reacts with the surrounding silica cladding, to reduce silicon atoms out of the silica. The silicon atoms accumulate during this process and finally occupy the entire core, resulting in a silicon core fibre with silica cladding. However, as yet, no optical guiding has been reported for these fibres, so little is known about their photonic properties.

Summarising the efforts of the abovementioned groups towards reducing the losses in the semiconductor core fibres, Table 2.1 provides a compilation of the lowest measured lowest loss values for a variety of semiconductor optical fibres, with core size and citation specified. Loss values less than 3 dB/cm are now being regularly reported, which are comparable with those of the well-developed semiconductor planar waveguides. These low loss values open up the potential for exploring nonlinear effects in the semiconductor core fibres platforms. In order to observe nonlinear effects in the semiconductor core fibres, the fibre core size and length are also needed to take into account and will be discussed in Chapter 5.

2.4 Planar based semiconductor waveguides

Over the past few decades, a large number of functional photonic devices have been fabricated and demonstrated using semiconductor materials, most of which have been

based on the well-developed silicon-on-insulator (SOI) platform. Driven by the fast increasing bandwidth needed to cope with the increasing demands on telecommunications systems, silicon is favoured for optoelectronic integration because its compatible with complementary metal-oxide-semiconductor (CMOS) technology, and its potential as a monolithic platform. Silicon is also an inexpensive material and its transparency window covers the full optical communications windows. Most of the silicon waveguides used in the near infrared regime around 1.3 μm and 1.55 μm are based on the SOI platform. The waveguides based on SOI platform have small footprint because of the tight optical confinement. SOI waveguides can be fabricated by the standard nanolithography. Low loss SOI waveguides can be obtained by minimizing the scattering loss of the etched sidewalls and improving the material purity through fabrication optimization. The lowest loss achieved in shallow rib waveguides based on SOI is as low as 0.272 ± 0.012 dB/cm at 1.55 μm [52]. Using this platform, many functional devices such as wavelength-division multiplexing (WDM), resonators [53], high speed modulators [6] and photodetectors [54] have been realized.

Similar to silica optical fibres, most of the important nonlinear processes have been studied extensively in silicon waveguides on-chip, including two-photon absorption (TPA), free carrier absorption (FCA), self-phase modulation (SPM), cross-phase modulation (XPM) and four-wave mixing (FWM) etc [55, 56]. One of the most popular nonlinear processes is supercontinuum generation which has been demonstrated in a silicon waveguide by making use of ultra short pulses as higher-order solitons [57, 58]. Recently, the generation of a spectral supercontinuum were demonstrated in a few centimetres long single silicon wire waveguide with spectral width from first 350 nm to much broad bandwidth [19, 56, 59]. Other investigations included the first demonstration of a XPM based interferometric switching in SOI waveguides [60]; format conversion of a 10 Gbit/s non-return-to-zero on-off-keying (NRZ-OOK) to a return-to-zero (RZ) data stream [61]; multiplexing up to a data rate of 42.7 Gbit/s using XPM [62]; FWM based signal processing for all-optical signal regeneration; amplification [63, 64]; signal reshaping and timing jitter reduction at low powers [65]. Furthermore, nonlinear applications of silicon waveguides in the mid-IR regime have attracted increased interests of late due to its lower losses compared to that at the near infrared wavelengths [14].

2.5 Waveguide platforms for the mid-infrared

Driven by the recent increased interest of mid-IR photonics as discussed in Section 1.2, a range of group IV semiconductor platforms have been proposed [66]. Passive waveguides are the basic elements needed to exploit more complex optical and electronic functionality in the mid-IR region. By carefully designing the waveguide dimensions, low loss waveguides have been demonstrated in a SOI rib waveguide with very low loss values of $0.6-0.7$ dB/cm at 3.39 μm for both TE and TM polarizations [67]. The mode leakage to

the substrate is the main source of losses as the size of the guided mode grows bigger for longer wavelengths. However, as the absorption of the buried SiO_2 material increases significantly for wavelengths longer than 3.6 μm, this limits the use of SOI platforms for longer mid-IR wavelengths. Hence, alternative material combinations and novel waveguide designs will have to be used for the mid-IR wavelength range. Researchers in this field have proposed several alternative platforms based on different materials and waveguide structures such as silicon-on-sapphire (SOS), silicon-on-porous silicon (SiPSi), suspended silicon and Ge-on-Si. Figure 2.3 shows the predicted transparency ranges of the group IV material waveguide platforms. The advantages and disadvantages of these waveguides will be briefly reviewed by the following standards: transparency window, fabrication complexity and cost.

SOS was primarily used as an alternative for SOI wafers by the electronics industry as sapphire is an excellent electrical insulator, preventing stray currents caused by radiation from spreading to nearby circuit elements. However, sapphire has a large transparency window from 0.4 μm to 5.5 μm so it is ideal to replace silicon dioxide as the cladding material for mid-IR applications. A SEM image of a SOS waveguide facet can be seen in Figure 2.4(a). Propagation losses of 3.6 dB/cm at 3.4 μm, 4.3 dB/cm at 4.5 μm, 1.9 dB/cm at 5.08 μm, and 4 dB/cm at 5.5 μm for SOS waveguides have been achieved [12, 68, 69, 70]. But sapphire is not a cost effective material and only transparent up

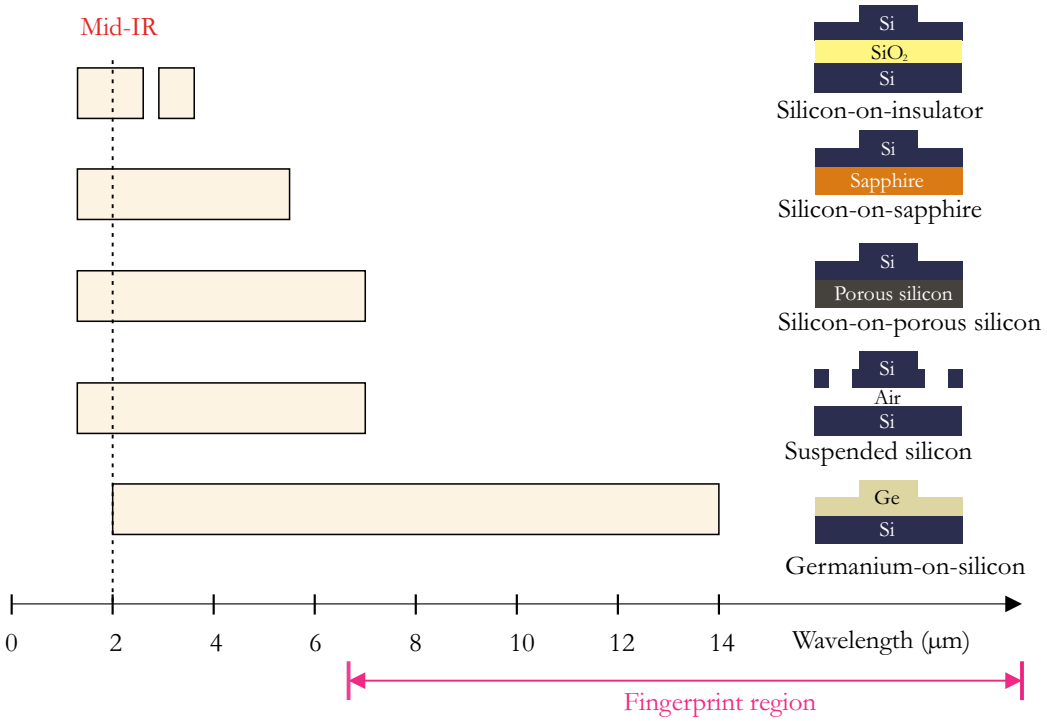

Figure 2.3: Approximate transparency windows in the $0 - 20\,\mu$m range for selected the group-IV material platforms for the mid-IR regime. Transparency is defined here as fundamental loss of the bulk material < 1 dB/cm, and wavelength limits for the ranges are from Ref. [66].

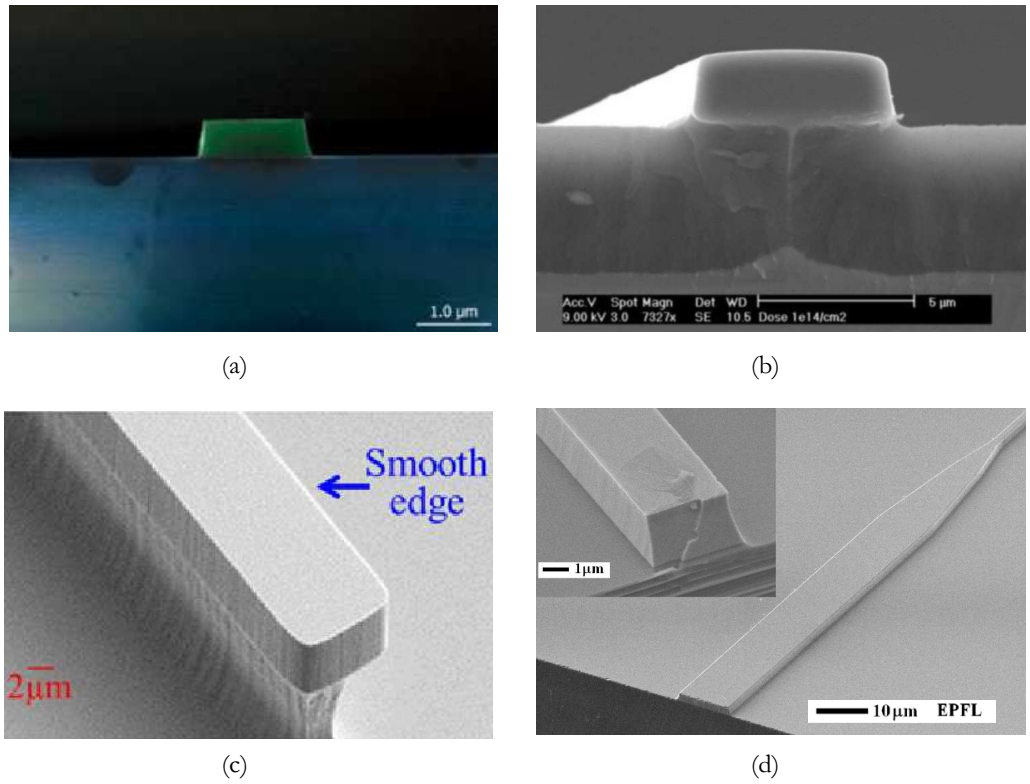

(a) (b)

(c) (d)

Figure 2.4: SEM images of various waveguide platforms for the mid-IR wavelenths. (a) SOS (reproduced from [12]). (b) SiPSi (reproduced from [67]). (c) Suspended silicon (reproduced from [73]). (d) Ge-on-Si (reproduced from [13]).

to $\sim 5.5\,\mu$m which limits its operational wavelength range. Another consideration when using SOS for photonics is that, due to the hardness of sapphire, it is extremely difficult to polish the facets. Polishing SOS waveguide facets by focused ion beam milling was investigated, though at considerable additional expense [68].

Porous silicon is fabricated by electrochemical partial dissolution of silicon. Thus it still maintains a large transparency window in the mid-IR regime, but the refractive index can be tuned from a value of 1.4 to 3 by changing the preparation conditions [71]. Hence, by replacing the silicon oxide with porous silicon, the waveguides can be fabricated to guide light at longer mid-IR wavelengths. A SEM image of a SiPSi waveguide cross section is shown in Figure 2.4(b). The propagation loss was measured to be 3.9 dB/cm at $3.39\,\mu$m which is attributed to increased surface roughness [67].

Suspended silicon waveguides have been proposed, whereby the silicon dioxide cladding is replaced by air to minimize the absorption at longer wavelengths. A SEM image of a suspended silicon waveguide is illustrated in Figure 2.4(c). Cheng *et al.* designed and characterized a 340 nm high silicon rib waveguide with an undercut buried oxide (BOX), with loss of 3 dB/cm at a wavelength of $2.75\,\mu$m [72]. Lower loss waveguides (2.7 dB/cm at $2.75\,\mu$m) have been demonstrated along with a Y branch splitter by Lin et al [73]. More recently, Soler-Penades *et al.* have reported a propagation loss of 3.4 dB/cm

at 3.8 μm in a suspended waveguide with sub-wavelength grating lateral cladding [74]. Such waveguides can support wavelengths up to $\sim$ 7 μm as it is only limited by the inherent loss of silicon. The disadvantages of the suspended silicon waveguides is that the fabrication process is very complex and the structures are not mechanically stable.

Although Ge-on-Si platforms have long been proposed as potential candidates for mid-IR applications [75], it is only fairly recently in 2012 that the first Ge-on-Si waveguide emerged [13]. A SEM image of the cross section of this waveguide can be seen in Figure 2.4(d). At around 5.0 μm, the loss for single mode strip waveguide was reported by Malik *et al.* to be $2.3 - 3.5$ dB/cm for TE polarization and $3 - 4$ dB/cm for TM polarization [76]. Chang *et al.* measured the propagation loss is 2.5 to 3.0 dB/cm at a wavelength of 5.8 μm using a quantum cascade laser (QCL). Moreover, there have also been reports of evanescent waveguide sensors [77] and wavelength (de)multiplexers [78]. As germanium has material absorption loss less than 1 dB/cm from $2 - 16$ μm, although the silicon substrate exhibits high absorption for $\lambda > 7.8$ μm, Ge-on-Si waveguides may have acceptable losses all the way to 16 μm if the mode overlap with the substrate is minimized. Thus, this material platform is expected to have the widest range of operation of all those discussed, and the detailed description of fabrication and characterisations of this waveguide will be presented in Section 4.4.4.

2.6 Mid-infrared nonlinear photonics in semiconductor waveguides

Compared to the well explored telecom wavelength regime, the transmission properties of semiconductor waveguides in the mid-IR regime have not received as much attention. However, owing to the low losses (both linear and nonlinear losses) in this regime, more interest has been raised to exploit the nonlinear optical effects in these waveguides. As discussed before, silicon is normally transparent and exhibits low propagation losses at near-infrared wavelengths, but it begins to strongly absorb light at high input intensities due to TPA and FCA. However, this absorption can be dramatically reduced when the pump wavelength is beyond 2.2 μm, which is the threshold for TPA to occur for crystalline silicon. As a result, the mid-IR regime has been regarded as a promising spectral regime for nonlinear applications. Jalali first presented the idea of silicon as a gain medium in this region through the development of a Raman laser [7], and following this, researchers from his group demonstrated a silicon Raman amplifier at 3.39 μm with 12 dB gain [79]. Parametric amplification and parametric generation of mid-IR light in silicon waveguides using FWM has been reported by different groups [64, 80]. Both of these demonstrations employed pump wavelengths near the TPA edge of 2200 nm, where TPA and the associated FCA are low. Furthermore, by pumping beyond 2.2 μm, Kuyken *et al.* demonstrated supercontinuum generation in silicon spanning three-quarters of an octave from 1535 to 2525 nm [81]. More recently, this same group demonstrated

an octave-spanning mid-IR frequency comb in a silicon nanophotonic wire waveguide pumped at 2290 nm [10].

For germanium, although the Kerr nonlinearity of germanium is predicted to be larger than that of silicon, the nonlinear effects in germanium have not yet been exploited. This is due to the fact that the low loss germanium waveguides have only recently been demonstrated and also difficulties of finding a high power laser source above the TPA limit of germanium ($> 3.7\,\mu$m). Thus, only early measurements of the nonlinear coefficients in bulk germanium have been reported at selected mid-IR wavelengths using the Z-scan technique [82, 83, 84]. From these nonlinear absorption of germanium is found to be three orders of magnitude larger than silicon at its peak value. Our group and collaborators have fabricated low loss germanium waveguides on silicon substrates that have allowed for the first characterization of their nonlinearities, and these results will be presented in Chapter 6.

2.7 Literature review summary

In this chapter, I have reviewed the existing literature relating to the mid-IR waveguide platforms and describe the use of group-IV material (mainly silicon and germanium) to explore mid-IR photonics. Both the fibre and planar based waveguide platforms have been reviewed. From the discussions, semiconductor waveguides made from silicon and germanium have been shown to be very promising candidates for mid-IR waveguides in terms of ease of fabrication and wide transparency. Following this review, detailed investigations including linear and nonlinear characterisations of these two the mid-IR semiconductor waveguide platforms will be presented in the later chapters.

Chapter 3

Background

3.1 Introduction

In this chapter, the fundamentals of optical waveguiding and lightwave propagation in waveguides are discussed, with emphasis on semiconductor waveguides using group IV elements as the guiding medium. These waveguides form the basic blocks to build optical devices and integrated circuits for group IV photonics. The light confinement and propagation in the waveguides are determined by their geometry and material properties. The equation that governs optical pulse propagation in the waveguides is presented with a description of the basic transmission parameters, such as attenuation and dispersion. The nonlinear parameters are also included to build a comprehensive model to describe the nonlinear effects during wave propagation in the semiconductor waveguides. This chapter provides the theoretical background for this PhD project and presents a numerical model to investigate the optical properties of these waveguides.

3.2 Waveguide characteristics

3.2.1 Waveguide structure

Optical waveguides can be divided into two main types: (i) optical fibres with a cylindrical core surrounded by cladding and (ii) planar-based rectilinear waveguides. Figure 3.1 shows the cross-sections of these two waveguides and the corresponding refractive index profile. The direction of propagation of the optical field is along the z-axis. For the semiconductor optical fibre, the refractive index of the core material (n_1) is higher than that of the silica cladding (n_2). In the planar-based slab waveguides (the simplest rectilinear waveguides), considering the simplest case when the refractive index of the cladding and substrate is the same, the refractive index of the core material (n_1) is also higher. In

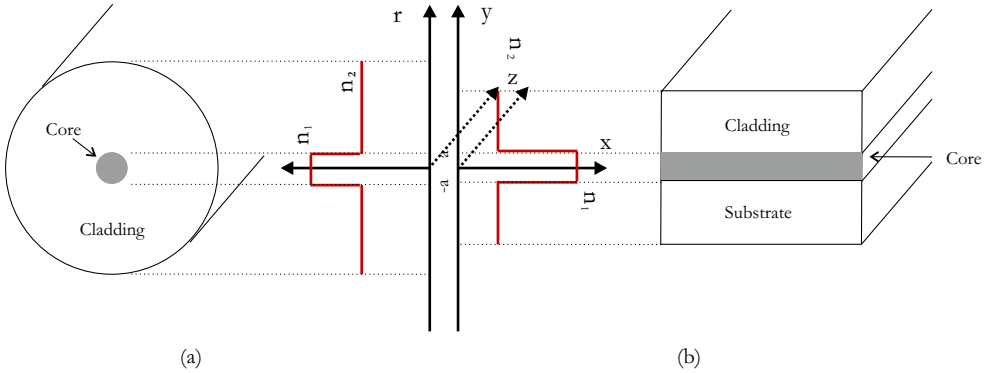

Figure 3.1: Basic structure and refractive-index profile of the optical waveguides: (a) step-index fibre, (b) planar slab waveguide.

both cases, light is confined in the core area via total internal reflection because of the refractive index difference between the high index core and the low index cladding or substrate.

The refractive index difference Δ of these two basic semiconductor waveguide is defined as follow [85]:

$$\Delta = \frac{n_1^2 - n_2^2}{2n_1^2} \cong \frac{n_1 - n_2}{n_1}. \tag{3.1}$$

The *numerical aperture (NA)* is defined to denote the maximum light acceptance angle of a waveguide:

$$NA = n \sin \theta_{\max} = \sqrt{n_1^2 - n_2^2}. \tag{3.2}$$

The large value of NA of a waveguide means that light rays with different incident angles can be transmitted in the core. The modes of a waveguide are formed by a group of light rays at a discrete angle of propagation. In the semiconductor optical fibre or slab waveguide (the slab width is much larger than the height), a *normalized frequency* V can be defined to describe the number of the modes in the symmetric waveguides shown in Figure 3.1.

$$V = \frac{2\pi a}{\lambda} \sqrt{n_1^2 - n_2^2}, \tag{3.3}$$

where $2a$ is the core dimension or slab height, and λ is the wavelength in vacuum. The normalized frequency V gives a general parameter to compare the mode propagation characteristics of the waveguides (independent of the waveguide structure). Typically for a step-index fibre, when $V < 2.405$ it will only allow singe-mode operation, while the higher-order modes are cut-off [86]. For a slab waveguide, when $V < V_c = \pi/2$, it

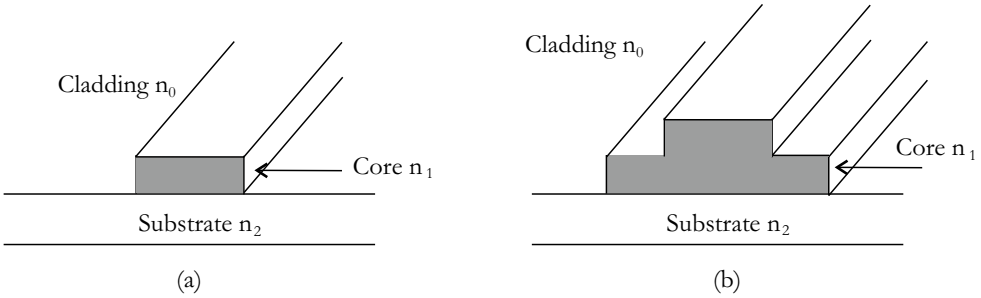

Figure 3.2: (a) Strip waveguide and (b) rib waveguide.

only allows singe-mode operation [85]. This condition will give a relation between the waveguide dimension or refractive index profile with the cut-off wavelength.

3.2.2 Modal properties

Following derivations from Maxwell's equations, the electric and magnetic field distributions in a waveguide can be described by the wave equations [85]. Depending on the waveguide geometry, either cylindrical or cartesian coordinate systems are chosen for the wave equations.

For semiconductor optical fibres, the fields are expressed in cylindrical coordinates, thus the wave equations can be written as

$$\frac{\partial^2 E_z}{\partial r^2} + \frac{1}{r}\frac{\partial E_z}{\partial r} + \frac{1}{r^2}\frac{\partial^2 E_z}{\partial \theta^2} + [k^2 n(r,\theta)^2 - \beta^2]E_z = 0 \tag{3.4}$$

$$\frac{\partial^2 H_z}{\partial r^2} + \frac{1}{r}\frac{\partial H_z}{\partial r} + \frac{1}{r^2}\frac{\partial^2 H_z}{\partial \theta^2} + [k^2 n(r,\theta)^2 - \beta^2]H_z = 0. \tag{3.5}$$

Here E_z and H_z are the field distributions for the transverse electromagnetic modes. β is the propagation constant, and the free space wavenumber $k = 2\pi/\lambda$.

For the simplest case of a slab planar waveguide, the following wave equations can be used to describe the electric and magnetic field distributions of the optical wave in the x-y plane [87]:

$$\frac{d^2 E_y}{dx^2} + (k^2 n^2 - \beta^2)E_y = 0, \tag{3.6}$$

$$\frac{d}{dx}\left(\frac{1}{n^2}\frac{dH_y}{dx}\right) + \left(k^2 - \frac{\beta^2}{n^2}\right)H_y = 0, \tag{3.7}$$

where E_y and H_y are the field distributions for transverse electric (TE) mode and transverse magnetic (TM) mode. The boundary conditions of the waveguide region are needed when solving the Equations 3.6 and 3.7 .

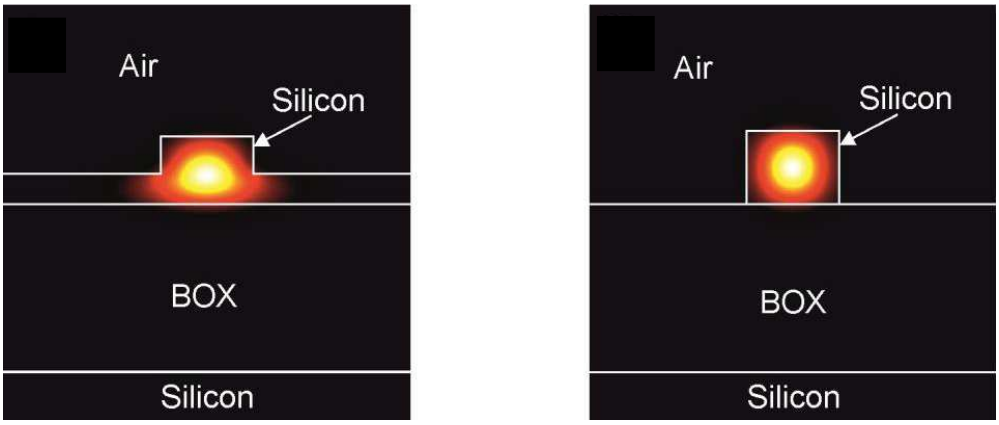

Figure 3.3: Fundamental mode profiles for different waveguide structures (a) strip waveguide and (b) rib waveguide. The mode images are reproduced from Ref. [90]

For the strip or rib waveguides shown in Figure 3.2, a similar analysis can be used but it is impossible to solve the wave equation analytically. In practice, numerical methods are used to analyze the strip or rib waveguides, and more detailed analysis can be found in Ref [85].

Each β in the wave equations corresponds to a guided mode in the waveguide. An effective refractive index related to the propagation constant β is defined as:

$$n_{\text{eff}} = \frac{\beta(\omega_0)}{k_0}. \tag{3.8}$$

In all the cases, the wave equations for $\tilde{E}_z$ can be solved by using the method of separation of variables [88]:

$$E_z(\mathbf{r}, t) = F(x, y)A(z, t)\exp[-i\beta(\omega_0)z]. \tag{3.9}$$

$F(x, y)$ is the mode distribution, β is the propagation constant, and $A(z, t)$ is the slowly varying temporal pulse. The last component in Equation 3.9 corresponds to the optical phase. $F(x, y)$ is the solution of the wave equations and corresponds to different spatial modes supported by either a fibre or a planar wavguide.

Specifically for an optical fibre, the mode distribution $F(x, y)$ is an m^{th}-order Bessel solution of the wave equations. For each integer m, the eigenvalue equations in general has several (n) solutions for β which corresponds to different modes with index mn. The detail solutions of the eigenvalue equations are not included here, as it can be found in many textbooks [85, 89]. Figure 3.3 shows the profiles of the fundamental modes for the three most commonly used optical waveguides.

In a waveguide, another important mode property is the effective mode area, which describes the mode distribution and confinement in the x-y plane. This can be defined as,

$$A_{\text{eff}} = \frac{\left[\int_{-\infty}^{\infty}\int_{-\infty}^{\infty}|F(x,y)|^2 dxdy\right]^2}{\int_{-\infty}^{\infty}\int_{-\infty}^{\infty}|F(x,y)|^4 dxdy}. \tag{3.10}$$

In general, semiconductor waveguides exhibits highly multimode nature because of the high refractive index contrast. Thus careful waveguide designs are required to realise single-mode operation.

3.2.3 Optical pulses

In order to investigate the pulse propagation in a semiconductor waveguide, a description of an optical pulse is required. If only considering the temporal variation of the pulse along the propagation direction z, typically the optical field, $A(z,t)$, can be expressed as a Gaussian envelope with phase $\phi(t)$:

$$A(z,t) = \sqrt{P_0(z)}\exp\left(-\frac{t^2}{2T_0^2}\right)\exp[i\phi(t)], \tag{3.11}$$

where z is the propagation distance, $P_0(z)$ is the peak optical power and T_0 is the half-width (at $1/e$-intensity point). For a Gaussian pulse, practically full width half maximum (FWHM) is used in place of T_0, the two are related as

$$T_{\text{FWHM}} = 1.665T_0. \tag{3.12}$$

The pulses from some laser sources like femtosecond laser pumped optical parametric oscillator (OPO) exhibit a frequency chirp. The chirp of an optical pulse is usually understood as the time dependence of its instantaneous frequency. Thus a chirped Gaussian pulse can be expressed as:

$$A(z,t) = \sqrt{P_0(z)}\exp\left(-\frac{1+iC}{2}\frac{t^2}{T_0^2}\right)\exp[i\phi(t)], \tag{3.13}$$

where C is the chirp parameter. For a Gaussian like pulse, if there is a chirp on the initial pulse, the spectral width will be broadened. The time-bandwidth product of a pulse is defined as the product of its temporal duration and spectral width. The minimum possible timebandwidth product is obtained for bandwidth-limited pulses. Thus a chirped pulse is not transform-limited and the time-bandwidth relation becomes $\Delta\omega T_0 > 0.44$ (note, the temporal duration and spectral width are the FWHM values). The absolute value of the chirp $|C|$ can be estimated by calculating the time-bandwidth product of the pulse.

Alternatively, a hyperbolic secant pulse is used in the context of optical solitons and pulse emitted from mode-locked fibre lasers and this pulse can be described as follows:

$$A(z,t) = \sqrt{P_0(z)}\text{sech}\left(\frac{t}{T_0}\right)\exp\left(-\frac{iCt^2}{2T_0^2}\right)\exp[i\phi(t)], \tag{3.14}$$

For a hyperbolic secant pulse, T_{FWHM} is the related to the pulse width as

$$T_{\text{FWHM}} = 1.763T_0. \tag{3.15}$$

The minimum time-bandwidth product for an unchirped hyperbolic secant pulse is approximately 0.315.

The temporal optical field can be expressed in the frequency domain simply through the Fourier transform $\mathscr{F}\{A(z,t)\}$:

$$\tilde{A}(z,\omega) = \int_{-\infty}^{\infty} A(z,t)\exp(i\omega t)dt. \tag{3.16}$$

The temporal optical field and the optical spectrum can only be transformed through the Fourier transform and the inverse Fourier transform when both temporal amplitude and phase of the optical pulse is known.

3.2.4 Linear losses

Light propagating in semiconductor core waveguides will experience attenuation from different mechanisms. The linear transmission losses in semiconductors, primarily originate from two sources: scattering and absorption. As both are wavelength dependent, the total linear loss is related to the wavelength of the light transmitted in the waveguide. For a certain wavelength, the transmitted power $P_{_T}$ is given by:

$$P_{_T} = P_{_I}\exp(-\alpha_{_l}L), \tag{3.17}$$

where $\alpha_{_l}$ is the linear loss coefficient, $P_{_I}$ is the power launched into the waveguide and L is the waveguide length. $\alpha_{_l}$ is more commonly expressed in decibels per unit length:

$$\alpha_{\text{dB}} = -10\log\left(\frac{P_{_T}}{P_{_I}}\right)/L = 4.343\alpha_{_l}. \tag{3.18}$$

In this thesis, the unit for linear loss is in [dB/cm] as semiconductor waveguides exhibit linear loss on this order. As mentioned, the linear losses of semiconductor waveguides are related to the operation wavelength. Material absorption is intrinsic to the materials used for the waveguide core and cladding. The scattering losses tend to arise from the material surface roughness or imperfections in the bulk material. The contribution to the

main linear attenuation mechanisms affecting transmission in particular semiconductor waveguides will be described in Chapter 4.

3.2.5 Dispersion

When an electromagnetic wave propagates in an optical waveguide or bulk media, the phase velocity of the wave depends on its frequency ω. This phenomenon, referred to as dispersion, manifests through the wavelength dependence of the refractive index $n(\lambda)$. For a short optical pulse, the fibre dispersion is critical to describe its propagation. Mathematically, the dispersion can be accounted for by expressing the mode propagation constant β as a Taylor series expansion about the center frequency ω_0 of the pulse spectrum:

$$\beta(\omega) = n(\omega)\frac{\omega}{c} = \beta_0 + \beta_1(\omega - \omega_0) + \frac{1}{2}\beta_2(\omega - \omega_0)^2 + \cdots, \tag{3.19}$$

where

$$\beta_m = \left(\frac{d^m\beta}{d\omega^m}\right)_{\omega=\omega_0} (m = 0, 1, 2, \cdots). \tag{3.20}$$

The parameters β_m represent the mth order dispersion. In this work, due to the relatively short waveguide length, only the first two dispersion coefficients β_1 and β_2 are needed to calculate the dispersion of the optical pulses. The parameters β_1 and β_2 are related to the refractive index $n(\omega)$ and its derivatives through the following equations:

$$\beta_1 = \frac{1}{v_g} = \frac{1}{c}\left(n + \omega\frac{dn}{d\beta}\right), \tag{3.21}$$

$$\beta_2 = \frac{1}{c}\left(2\frac{dn}{d\beta} + \omega^2\frac{d^2n}{d\omega^2}\right), \tag{3.22}$$

where v_g is the group velocity. The group velocity represents the velocity at which the envelope of the pulse propagates and can be expressed using $v_g = c/n_g$, whereby n_g is the group index. Since β_1 is related to v_g, the different spectral components of a pulse propagate at different velocities, causing the pulse to spread in time. The parameter β_2, referred to as the group-velocity dispersion (GVD), represents the dispersion of the group velocity which causes the pulse to spread. If $\beta_2 < 0$ then blue-shifted wavelengths travel faster than red-shifted wavelengths. This is the anomalous dispersion regime. Similarly, when red-shifted wavelengths travel faster than blue-shifted wavelengths is $\beta_2 > 0$. This is the normal dispersion regime [91]. When $\beta_2 = 0$ this is the zero-dispersion wavelength (ZDW) and higher order terms from the Taylor expansion (e.g. $m = 3$ and 4) are required to calculate the exact dispersion at this point.

In semiconductor waveguides, the GVD consists of the material dispersion and waveguide dispersion. The first is due to the wavelength dependence of the refractive index $n(\lambda)$

and the second relates to effective refractive index (n_{eff}), which is determined by the waveguide geometry and dimensions [92].

3.2.5.1 Material dispersion

The refractive index $n(\lambda)$ in semiconductor material is well approximated by the *Sellmeier equation* [16]:

$$n^2(\lambda) = 1 + \sum_{i=1}^{m} \frac{S_i(T)\lambda^2}{\lambda^2 - \lambda_i^2(T)}, \tag{3.23}$$

where λ is the wavelength, and $S_i(T)$ are the strengths of the resonance features in the material at $\lambda_i(T)$. These parameters are experimentally determined coefficients estimated by fitting the measured refractive indices at different wavelengths λ and temperatures T. The *Sellmeier equation* provides all the information required to establish the wavelength dependent refractive index of a material.

For silicon, the following modified Sellmeier expression derived by Edwards *et al* produced the best fit to the experiment data [93],

$$n^2(\lambda) = \varepsilon + \frac{\mathrm{A}}{\lambda^2} + \frac{\mathrm{B}\lambda_1^2}{(\lambda^2 - \lambda_1^2)}, \tag{3.24}$$

where $\lambda_1 = 1.107\,\mu$m, $\varepsilon = 1.16858 \times 10^1$, $\mathrm{A} = 9.39816 \times 10^{-1}$ and $\mathrm{B} = 8.10461 \times 10^{-3}$.

For germanium, the modified Sellmeier expression was used to calculate the refractive index developed by Barnes and Piltch [94]:

$$n^2(\lambda) = \mathrm{A} + \frac{\mathrm{B}\lambda^2}{(\lambda^2 - \mathrm{C})} + \frac{\mathrm{D}\lambda^2}{(\lambda^2 - \mathrm{E})}, \tag{3.25}$$

where $\mathrm{A} = 18.28156$, $\mathrm{B} = 6.72880$, $\mathrm{C} = 0.44105$, $\mathrm{D} = 0.21307$ and $\mathrm{E} = 3870.1$.

Using the above equations, the wavelength dependences of the refractive index for silicon and germanium were calculated and shown in the Figure 2.2, which provides the basic optical properties of these two semiconductor material and can be used to calculate the GVD for a given waveguide.

3.2.5.2 Waveguide dispersion

In step-index waveguides, smaller wavelengths of arbitrary transverse distribution will be more tightly confined in the core. Larger wavelengths will have a broadened distribution and thus be less confined. This dependence of field distribution on wavelength leads

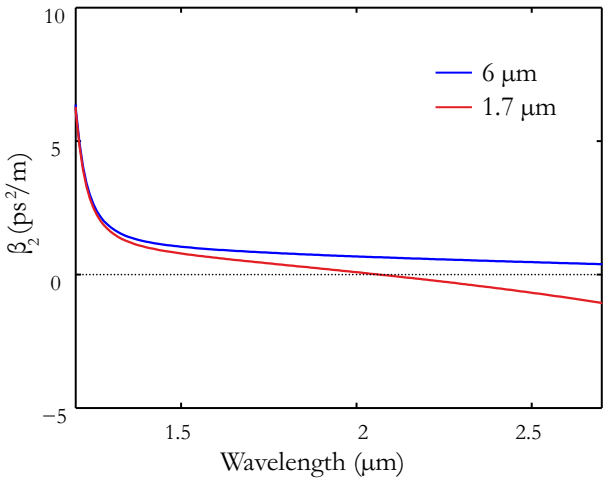

Figure 3.4: Simulated group velocity dispersion for 6 μm and 1.7 μm diameter core a-Si:H fibres.

to a perturbation in the effective refractive index, thereby modifying the propagation constant β. As discussed in Section 3.2.2, calculations of β are determined by numerically solving the spatial solution to Maxwell's equations. This solution is known as the eigenvalue equation [96]. The eigenvalue equation relates β to an optical waveguide's dimensions and refractive indices at a given wavelength.

The GVD of a waveguide with given dimensions can be calculated using the finite element method (FEM) to solve the eigenvalue equations. Figure 3.4 shows the calculated dispersion curves for two specific silicon core fibres with different core diameters, illustrating how the waveguide geometry can affects the GVD. For an example, GVD calculations for the hydrogenated amorphous silicon (a-Si:H) core fibres are presented here. These a-Si:H core fibres will be used for the nonlinear characterisations in Chapter 5 where these pre-determined dispersion properties are critical for the simulation work for short pulse propagation. As the material dispersion for a-Si:H is not well documented, in the simulations an approximation was made using the Sellmeier equation for c-Si [97], which was modified slightly to reflect the higher refractive index of the a-Si:H material ($n \sim 3.6$ at 1.55 μm). Similar approaches have been adopted by several groups working on-chip [98, 99], and shown to provide reasonable agreement with the measured dispersion for their a-Si:H waveguides [100]. For a core diameter of 6 μm, the light only exhibits normal dispersion within this wavelength region while the smaller 1.7 μm core silicon fibre has a ZDW at around 2.1 μm. From the calculations of the GVD, it demonstrates the capability to engineer the dispersion by simply scaling down the waveguide core size. As widely used in the planar silicon waveguides, manipulation of waveguide dimensions provides a large degree of freedom for tailoring the waveguide dispersion to compensate the large normal material dispersion caused by the high refractive index contrast [95]. Dispersion engineering is critical for many nonlinear applications that require phase matching.

3.3 Waveguide nonlinearities

A high power propagating eletromagnetic field will locally modify the optical properties of the material. Nonlinearities in silicon and germanium all originate from the interactions of the optical field with electrons and phonons. The relation between an induced polarization $\mathbf{P}(\mathbf{r},t)$ and an electric field $\mathbf{E}(\mathbf{r},t)$ is typically expressed as a power series in the electric field [101]:

$$\mathbf{P}(\mathbf{r},t) = \varepsilon_0(\chi^{(1)}\mathbf{E}(\mathbf{r},t) + \chi^{(2)}\mathbf{E}^2(\mathbf{r},t) + \chi^{(3)}\mathbf{E}^3(\mathbf{r},t) + \cdots). \tag{3.26}$$

Here ε_0 is the vacuum electric permittivity and $\chi^{(i)}$ are the ith-order optical susceptibilities. The real part of $\chi^{(1)}$ is associated with the real part of the refractive index, whereas the imaginary part of $\chi^{(1)}$ describes loss or gain, which has been described in Section 3.2.4:

$$n(\omega) = 1 + \frac{1}{2}\mathbf{Re}[\tilde{\chi}^{(1)}(\omega)], \tag{3.27}$$

$$\alpha(\omega) = \frac{\omega}{nc}\mathbf{Im}[\tilde{\chi}^{(1)}(\omega)], \tag{3.28}$$

where $\tilde{\chi}(\omega)$ is the Fourier transform of $\chi^{(1)}(t)$.

The second-order susceptibility term $\chi^{(2)}$ is absent in centrosymmetric crystals such as silicon and germanium, hence it will not be discussed in this thesis. The lowest nonlinearity in silicon and germanium materials are from the $\chi^{(3)}$ susceptibility. Third-order nonlinearities are especially important in these materials as they exhibit a wide variety of phenomena such as SPM and TPA [15]. Figure 3.5 illustrates typical effects from the induced polarization. For the third-order nonlinearities, a nonlinear coefficient γ is defined to describe the semiconductor waveguide's nonlinear strength:

$$\gamma = \frac{k_0 n_2}{A_{\text{eff}}} + \frac{i\beta_{\text{TPA}}}{2A_{\text{eff}}}, \tag{3.29}$$

where n_2 refers to the nonlinear refractive index and β_{TPA} is the TPA coefficient. The relationship between these terms of the $\chi^{(3)}$ susceptibility will be described in the following sections.

3.3.1 Nonlinear absorption

Nonlinear absorption in semiconductors caused by TPA corresponds to the excitation of an electron in the valence band to the conduction band while absorbing two photons. Another absorption mechanism called free carrier absorption (FCA) can be caused by absorption due to the free carriers in the conduction band. For short pulse propagation in silicon and germanium, TPA is the main nonlinear absorption effect over the regime

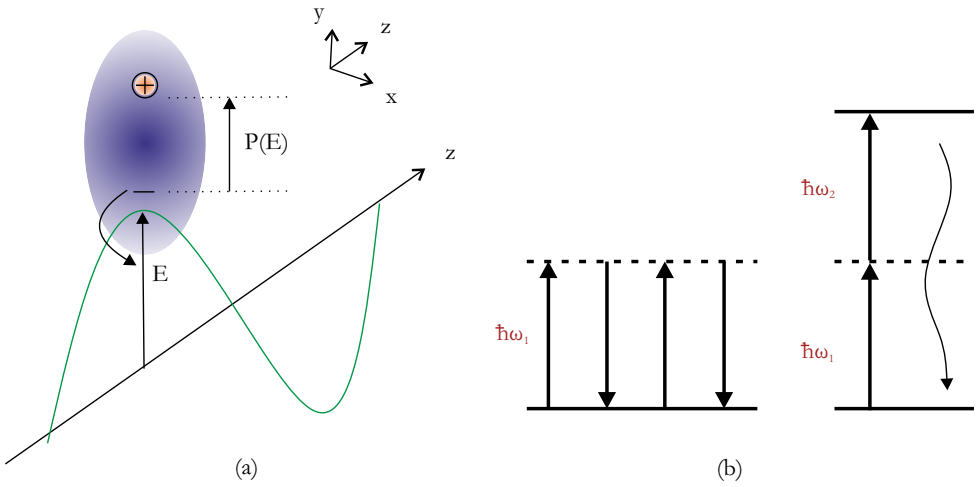

Figure 3.5: (a) An electromagnetic wave with electric field **E** passing through an atom and thereby inducing a dipole oscillation **P**. (b) Third-order nonlinear dipole transitions, showing SPM and TPA.

below their TPA edge wavelengths: 2.2 μm for silicon and 3.7 μm for germanium. When the sum of the energy of the photons exceeds the band gap energy, the two photons will be absorbed and excite an electron from the valence band to the conduction band, resulting in the generation of a free carrier (electron-hole pair). Figure 3.6 shows the schematic TPA process in semiconductor material. In silicon, TPA is three-particle process during which the absorption is assisted through phonon transitions allowing carriers to bridge the forbidden region because of the indirect nature of the band gap in [102, 103]. While in germanium, both indirect-gap and direct-gap TPA can occur, and their strengths are related to the operation wavelengths because of the different band gap energies of the indirect and direct band [104]. Typically, the TPA process can be classified as degenerate and non-degenerate depending on the frequencies of the absorbed photons. In the degenerate TPA, two identical photons are absorbed, while the photons absorbed in the non-degenerate case are of different frequencies. In this thesis, only the degenerate case is considered.

The depletion of optical power as a result of TPA depends on the TPA coefficient β_{TPA}, which can be defined through the $\chi^{(3)}$ nonlinearity [95]:

$$\beta_{\text{TPA}} = \frac{3\omega}{2\varepsilon_0 c^2 n_0^2} \mathbf{Im}[\tilde{\chi}^{(3)}(\omega)]. \tag{3.30}$$

Where c is the speed of light in vacuum and n_0 is the refractive index.

3.3.2 Free carrier density and absorption

The role played by free carriers depends very much on their lifetime (the time before they relax back down to the valence band). The carrier lifetime in a semiconductor parameter

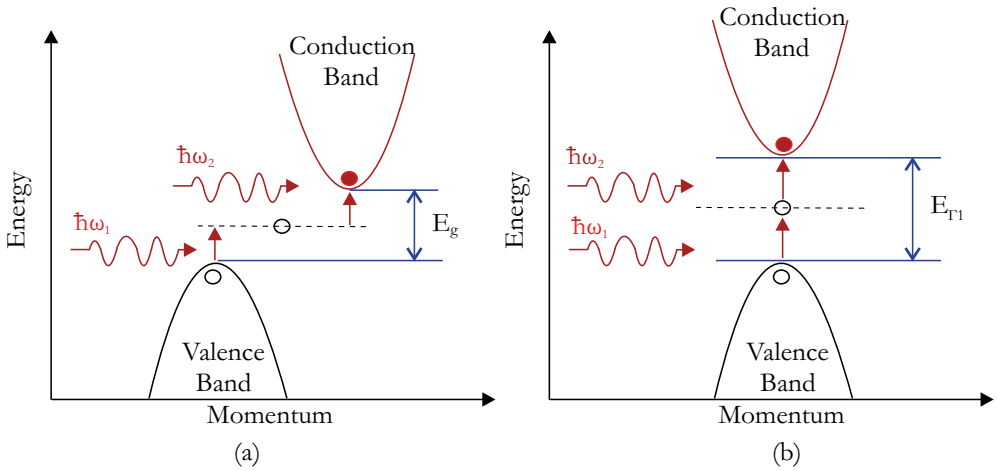

Figure 3.6: TPA of indirect bandgap (a) and direct bandgap (b) in semiconductor material.

is very sensitive to the structure and the density of lattice defects due to impurities. It is related to the material growth/deposition process as well as the contaminants, which can interact with lattice and structure defects. The recombination lifetime of most electronic devices is not a critical parameter due to the small distances that free carriers diffuse over. Compared to electronic components, the bulky size of photonic devices can cause carriers to remain mobile for large periods of time, from nanoseconds to microseconds, limiting their operating speed and efficiencies. Lifetime measurements are ideal for monitoring material performance as they are non-destructive and can reveal deep-level impurities of a semiconductor. This section focuses on the excited state carrier dynamics and investigates the lifetimes in silicon.

Figure 3.7 shows a selected number of photon excitation processes of free carries in the form of energy-momentum diagrams. Process [i] of Figure 3.7 shows the the carrier

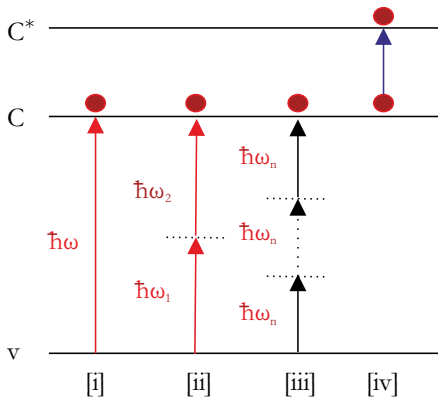

Figure 3.7: Energy level diagrams for photon excitation of free carriers and FCA. [i] Single photon absorption, [ii] TPA, [iii] MPA and [iv] FCA.

transition from valence band (V) to conduction band (C) by singe photon absorption. Process [ii] and [iii] of Figure 3.7 show the the carriers generated by TPA and multiphoton absorption (MPA). FCA is an intraband absorption. A photon's energy is absorbed by an electron already in the conduction band (C), raising it to a higher state of energy (C*), as shown in the process [iv] of Figure 3.7. Because the excited state transition in the process [iv] is small, the required input photon energy is very low. Carrier recombination is the opposite of generation and occurs as a result of interactions with other electrons, holes, photons, or the vibrating crystal lattice itself. The carrier recombination processes can be classified as radiative and non-radiative recombination, depending on whether a photon is generated.

In Figure 3.8(a), when an electron moves from its conduction band state into the empty valence band state associated with the hole during the radiative recombination, a photon is emitted because of the energy released during this process. This recombination typically happens in direct bandgap semiconductors. The radiative recombination is neglectable in silicon as it is an indirect band gap material and the probability of photon emission is limited by the crystal momentum mismatch.

Thermalisation is a type of intraband recombination, as the transitions occur within the band as shown in Figure 3.8(b). In this process, the exchange of energy between carriers and phonon is small but frequent. At thermal equilibrium, the thermal generation is balanced with thermal recombination.

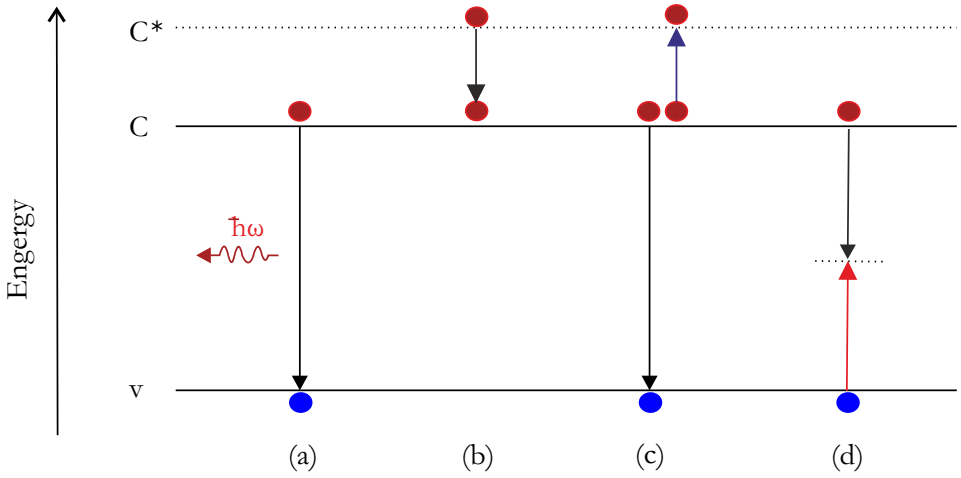

Figure 3.8: Carrier recombination mechanisms in semiconductors. C is conduction band, V is valence band. (a) Radiative recombination. (b) Theramlisation. (c) Auger recombination. (d) Shockley-Read-Hall recombination.

Auger recombination is a process in which an electron and a hole recombine in a band-to-band transition, but now the resulting energy is given off to another electron or hole. If the energy is transferred to an electron in the conduction band, it will get an increase in kinetic energy, which will normally be lost when the electron relaxes to the band edge. This is demonstrated in Figure 3.8(c). Auger processes are most important where carrier densities are high, which is the case for highly doped materials, or at high temperatures. Thus, Auger recombination is minimal in the intrinsic silicon (c-Si) or a-Si:H studied in this thesis.

The process in Figure 3.8(d) is known as Shockley-Read-Hall (SRH) recombination, also called trap-assisted recombination. The transition of carriers is between the conduction band and the new localized state (dashed line) introduced by an impurity and/or material defect. Such energy states are called deep-level traps and once the trap is filled it cannot accept another carrier. In the second step, the carrier may move to an empty valence band state or be re-excited to the conduction band, thereby completing the recombination. This recombination process in silicon is largely dependent on the material purity. Dangling bond defects which will be described in Chapter 4 are an example of localized states which could lead to SRH recombination in a-Si:H material.

Free carriers in a semiconductor vary in concentration depending on the input optical intensity and their presence leads to optical absorption. This type of absorption is due to optical transitions between electronic states in the same band, it is therefore necessary to understand the dynamics of the carrier density since their concentrations are heavily influenced by the input of optical pulses. When free carriers are generated, lateral diffusion (along x, y, z directions) and recombination will impact the total free carrier density defined as:

$$\Delta\alpha_{\text{FCA}} = \frac{e^3\lambda_0^2}{4\pi^2c^3\varepsilon_0 n}\left[\frac{N_e}{\mu_e(0.26m_0)^2} + \frac{N_h}{\mu_h(0.39m_0)^2}\right], \tag{3.31}$$

where e is the electronic charge, λ_o is the vacuum wavelength, c is the speed of light, ε_o is the permittivity of free space, n is the refractive index, $N_{e,h}$ is the electron and hole densities, $\mu_{e,h}$ is the electron and hole mobilities, and m_0 is the free electron rest mass. In the two-band approximation it is valid to assume equal densities of electron and hole carriers such that $N_e = N_h = N$ [105]. For a pulsed input, Equation 3.31 can then be simplified to [57]:

$$\Delta\alpha_{\text{FCA}} = \frac{e^3\lambda_0^2}{4\pi^2c^3\varepsilon_0 n}\left[\frac{1}{\mu_e(0.26m_0)^2} + \frac{1}{\mu_h(0.39m_0)^2}\right]N_c(z,t) \tag{3.32}$$

$$= \sigma_{\text{FCA}}N_c(z,t). \tag{3.33}$$

In the TPA window of the semiconductors, where the incident photon energy is between $E_g/2$ and E_g, the free carrier density N_c is related to the TPA parameter and can be

determined via the rate equation [106]:

$$\frac{\partial N_c(z,t)}{\partial t} = \frac{\beta_{\text{TPA}}}{2h\nu_0}\frac{|A(z,t)|^4}{A_{\text{eff}}^2} - \frac{N_c(z,t)}{\tau_c}, \tag{3.34}$$

where τ_c is the carrier lifetime.

3.3.3 Nonlinear refraction

Nonlinear refraction in semiconductor waveguides is due to the change of refractive index and originates from the third order susceptibility $\chi^{(3)}$. It is also called the optical Kerr effect. Besides the fundamental Kerr effect SPM, which is shown in Figure 3.5(b), there are also other nonlinear effects are related to the nonlinear refraction, including cross-phase modulation (XPM), third harmonic generation (THG) and four-wave mixing (FWM). The nonlinear processes that involve generation of new frequencies far away from the pump (e.g., THG and FWM) are not efficient if the phase matching condition is not satisfied. Thus, in order to investigate phase match related nonlinear processes, more careful waveguide designs are required. Two main nonlinear effects (SPM and FWM) in the semiconductor core fibres will be investigated in this thesis, and so in the basic principles are described in this section. The nonlinear refractive index n_2 is related to the real part of the $\chi^{(3)}$ susceptibility by [95]:

$$n_2 = \frac{1}{cn_0^2\varepsilon_0}\frac{3}{4}\mathbf{Re}(\chi^{(3)}). \tag{3.35}$$

3.3.3.1 Self-phase modulation

SPM is commonly observed when a short pulse travels through a nonlinear medium. SPM is a direct consequence of the Kerr nonlinearity, during which the refractive index of the waveguide medium will change due to propagation of high power intense light. The change of the refractive index will modify the spectral composition of the very same pulse. As a consequence, SPM leads to broadening of the pulse spectrum. When the light is propagating in the waveguide, the refractive index changes with the intensity as follows:

$$n(I) = n_0 + n_2 \cdot I, \tag{3.36}$$

where n_0 is the linear refractive index.

The nonlinear phase shift induced by the change in refractive index can be described by [88]:

$$\phi_{\text{NL}}(t) = n_2 I(t) k_0 z. \tag{3.37}$$

This nonlinear phase shift is linearly dependent on the input optical intensity $I(t)$ and the propagation length L. If a CW signal propagates through the waveguide, the phase change stays constant as a function of time. However, when a short pulse propagates through a waveguide, the phase change varies over time because of the varying intensity profile [107]. To account for the effects of the linear losses which are larger in a semiconductor waveguide, an effective length is defined as

$$L_{\text{eff}} = \frac{1 - \exp(-\alpha_l L)}{\alpha_l}. \tag{3.38}$$

Thus, Equation 3.37 can be rewritten as,

$$\phi_{\text{NL}}(t) = \gamma L_{\text{eff}} |A(t)|^2. \tag{3.39}$$

The nonlinear frequency shift induced by this nonlinear phase change is a direct consequence of the time dependence of $\phi_{\text{NL}}(t)$,

$$\delta\omega(t) = -\frac{\partial \phi_{\text{NL}}(t)}{\partial t} = -\gamma L_{\text{eff}} \frac{\partial}{\partial t} |A(t)|^2. \tag{3.40}$$

The time dependence of $\delta\omega(t)$ is referred to as frequency chirping as discussed in Section 3.2.3. The chirp induced by SPM increases in magnitude with the propagated distance. The new frequency components are generated continuously and hence cause the spectral broadening.

3.3.3.2 Four-wave mixing

FWM is a parametric process in which the optical media plays a passive role except for mediating interaction among several optical waves. In the FWM process, the refractive index is involved in the modulation, and a phase-matching condition must be satisfied. The nonlinear polarization that describes the FWM process can be obtained using the standard derivations from Equation 3.26 [88]:

$$\text{P}_{\text{FWM}} = \frac{3\varepsilon_0}{4} \chi^{(3)} [2E_1 E_2 E_3 \exp(i\theta_+) + 2E_1 E_2 E_3^* (i\theta_-) + \cdots], \tag{3.41}$$

where θ_+ and θ_- are defined as:

$$\theta_+ = (\beta_1 + \beta_2 + \beta_3 - \beta_4)z - (\omega_1 + \omega_2 + \omega_3 - \omega_4)t, \tag{3.42}$$

$$\theta_- = (\beta_1 + \beta_2 - \beta_3 - \beta_4)z - (\omega_1 + \omega_2 - \omega_3 - \omega_4)t. \tag{3.43}$$

Equation 3.42 corresponds to the case in which three photons transfer their energy to a single photon. In general, the phase-matching condition is difficult to satisfy for this process to occur in semiconductor waveguides, and thus the efficiencies is low. The most common case in FWM process is that two photons at frequencies ω_1 and ω_2 are annihilated while two photons at frequencies ω_3 and ω_4 are created simultaneously such that

$$\omega_1 + \omega_2 = \omega_3 + \omega_4, \tag{3.44}$$

In the case of degenerate FWM ($\omega_1 = \omega_2$), the energy conservation condition can be expressed by:

$$2\omega_p = \omega_s + \omega_i, \tag{3.45}$$

where ω_p, ω_s and ω_i represent the frequencies of the pump, signal and idler. In this case, a strong pump at ω_p can creates two sidebands located symmetrically at frequencies ω_s and ω_i. The frequency shift Ω can be described as:

$$\Omega = |\omega_p - \omega_s| = |\omega_i - \omega_p|, \tag{3.46}$$

The phase-matching condition for this process can be obtained by setting the first component in Equation 3.43 equal to zero:

$$2\beta_p - \beta_s + \beta_i = 0. \tag{3.47}$$

The phase-mismatch $\Delta\kappa$ is defined as:

$$\Delta\kappa = \beta_s + \beta_i - 2\beta_p \tag{3.48}$$

$$= (\tilde{n}_s\omega_s + \tilde{n}_i\omega_i - 2\tilde{n}_p\omega_p)/c, \tag{3.49}$$

where $\tilde{n}_p$, $\tilde{n}_s$ and $\tilde{n}_i$ are the effective mode indices for the pump, signal and idler light.

Following standard deviations demonstrated by Agrawal, the phase mismatch can be divided into the linear part Δk_l and nonlinear part Δk_{nl} [88]:

$$\Delta\kappa = \Delta k_l + \Delta k_{nl}. \tag{3.50}$$

Here Δk_l and Δk_{nl} represent the mismatch occurring as a result of dispersion and the nonlinear effects, respectively.

The dispersion contribution Δk_l can be approximated in terms of the frequency shift Ω in Equation 3.46 using the expansion of the propagation constant in Equation 3.19 [108],

$$\Delta k_l \approx \beta_{2p}\Omega^2 + (\beta_{4p}/12)\Omega^4, \tag{3.51}$$

where β_{2p} and β_{4p} are the dispersion parameters at the pump frequency ω_p. The pump-induced nonlinear phase shift resulting from the SPM and XPM [88] can be described as follow

$$\Delta k_{nl} = 2\gamma_p P_p. \tag{3.52}$$

Hence, the phase-matching condition can be written as:

$$\beta_{2p}\Omega^2 + (\beta_{4p}/12)\Omega^4 + 2\gamma_p P_p = 0. \tag{3.53}$$

For pump wavelengths not to close to the ZDW, we can ignore the higher order contribution of dispersion. The simplified phase-match condition can be written as:

$$\beta_{2p}\Omega^2 + 2\gamma_p P_p = 0. \tag{3.54}$$

From this equation, anomalous dispersion with negative β_{2p} is required to achieve efficient FWM. If the pump is located close to the ZDW where $|\beta_{2p}|$ is small, higher order dispersion should be taken into consideration in the phase-matching condition and FWM can occur in the normal dispersion regime. For the wavelength range investigated in this thesis, the approximation solution of Equation 3.54 is enough for our analysis, which will be described in Chapter 5.

3.4 Optical wave propagation in semiconductor waveguides

3.4.1 Generalized nonlinear Schrödinger equation

The nonlinear Schrödinger equation (NLSE) is used to describe nonlinear pulse propagation in an optical waveguide [88]. Equation 3.55 is the standard form used for silica optical fibres and includes the effects of dispersion through β_i, the effect of nonlinearity through γ and fibre loss through the parameter α_l. The pulse amplitude A has the units

$W^{1/2}$, i.e., $|A|^2$ is the optical power.

$$\frac{\partial A}{\partial z} + \frac{i}{2}\beta_2\frac{\partial^2 A}{\partial T^2} + \frac{i}{6}\beta_3\frac{\partial^3 A}{\partial T^3} + \cdots + \frac{\alpha}{2}A = i\gamma|A|^2 A. \tag{3.55}$$

where $\beta_i (i = 1, 2, 3, \cdots)$ represents the ith material's optical dispersion in optical medium and γ is defined as (without including TPA):

$$\gamma = \frac{2\pi n_2}{\lambda A_{\text{eff}}}, \tag{3.56}$$

where A_{eff} is the effective area as defined in Section 3.2.2.

For semiconductor materials, it is necessary to modify the basic NLSE to include the effects of TPA, FCA, and free carrier dispersion (FCD). By ignoring higher order dispersion terms, the generalized NLSE can be written by [106]:

$$\frac{\partial A(z,t)}{\partial z} = -\frac{i\beta_2}{2}\frac{\partial^2 A(z,t)}{\partial t^2} + i\gamma|A(z,t)|^2 A(z,t) - \frac{1}{2}(\alpha_l + \sigma_f)A(z,t). \tag{3.57}$$

Here γ is now the modified nonlinear parameter, and σ_f is the free carrier contribution, respectively. Both the Kerr and TPA contributions should be included in the nonlinear coefficient γ as defined in Section 3.3.

Similarly, the free carrier contribution is also complex: $\sigma_f = \sigma(1 + i\mu)N_c$, where σ is the FCA coefficient and μ governs the FCD. Since σ_f depends on N_c, Equation 3.57 is solved in conjunction with Equation 3.34 repeated here for completeness.

$$\frac{\partial N_c(z,t)}{\partial t} = \frac{\beta_{\text{TPA}}}{2h\nu_0}\frac{|A(z,t)|^4}{A_{\text{eff}}^2} - \frac{N_c(z,t)}{\tau_c},$$

To determine the length scales over the dispersive and nonlinear effects dominate the dispersion length L_D and nonlinear length L_{NL} are defined as follows:

$$L_D = \frac{T_0^2}{\beta_2}, \tag{3.58}$$

$$L_{NL} = \frac{1}{\gamma P_0}. \tag{3.59}$$

By comparing these different lengths, an estimate of which effects dominate during the pulse propagation can be obtained. If the waveguide length $L << L_D$ and $L << L_{NL}$, neither dispersive nor nonlinear effects play a significant role during the pulse propagation. When the waveguide length is longer or comparable to the L_D and L_{NL}, both dispersion and nonlinearity need to be considered in the pulse propagation. In this case, a fascinating manifestation results from the interplay between dispersive and nonlinear effects is the optical solitons, of which the pulse do not change or follow a periodic evolution pattern along the propagation direction. A paremeter N is defined is

introduce as the soliton order

$$N^2 = \frac{L_D}{L_{NL}} = \frac{\gamma P_0 T_0^2}{|\beta_2|}. \tag{3.60}$$

For fundamental soliton ($N = 1$), GVD and SPM balance each other so that the pulse shape and spectrum stay the same. In the case of higher-order solitons, SPM dominates initially but followed by the GVD resulting in pulse contraction, this is commonly happened in the nonlinear processes during supercontinuum generation. A soliton period z_0 was defined as

$$z_0 = \frac{\pi}{2} L_D = \frac{\pi}{2} \frac{T_0^2}{|\beta_2|} \approx \frac{T_{\mathrm{FWHM}}^2}{2|\beta_2|}. \tag{3.61}$$

The detailed description for the soliton propagation can be found in Ref. [88], the simple definition presented in this section will provide the background knowledge of the our analysis of spectral evolution in Chapter 5.

3.4.2 Split-step Fourier method

In the generalised NLSE (Equation 3.57), and free carrier density equation (Equation 3.34), there are two primary effects that contribute to the pulse profile evolution along the silicon fibre. The split-step Fourier method [109] can be used to solve these coupled nonlinear equations. Firstly, it is clearer to write Equation 3.57 in the form below

$$\frac{\partial A}{\partial z} = (\hat{D} + \hat{N})A, \tag{3.62}$$

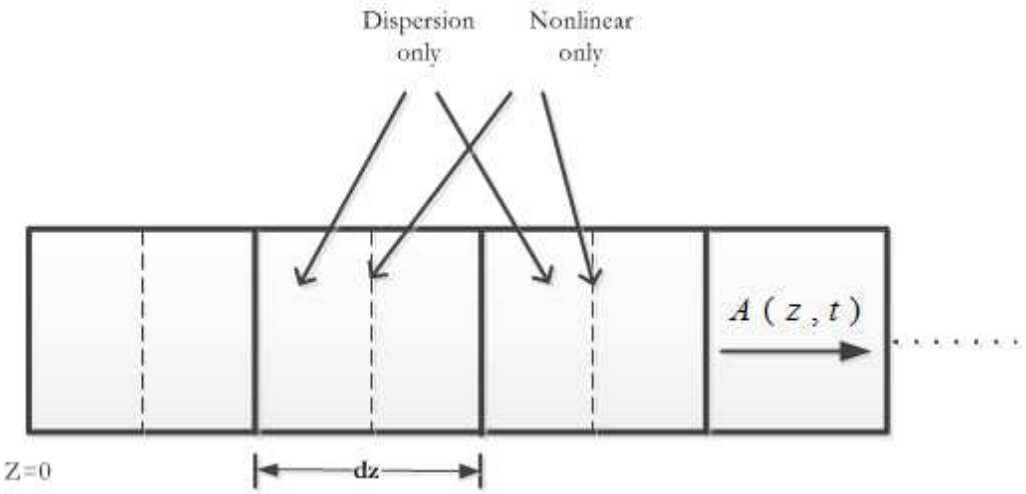

Figure 3.9: Schematic illustration of the split-step Fourier method used for numerical simulations.

where there are two operators that represent linear loss, dispersion and nonlinear effects separately on pulse propagation. These operators are given by:

$$\hat{D} = -\frac{i\beta_2}{2}\frac{\partial^2}{\partial t^2} + \frac{\beta_3}{6}\frac{\partial^3}{\partial t^3} - \frac{\alpha_l}{2}$$
$$\hat{N} = (\frac{ik_0 n_2}{A_{\text{eff}}} - \frac{\beta_{TPA}}{2A_{\text{eff}}})|A|^2 - \frac{\sigma N_c}{2}. \tag{3.63}$$

These linear and nonlinear effects take place at the same time during the pulse propagation. However, the split-step Fourier method obtains an approximate solution by assuming that when propagating the optical field over a small distance dz, the linear loss, the dispersion and nonlinear effects can be assumed to act independently, as illustrated in the Figure 3.9. After each D step, the carrier density N_c was solved from Equation 3.34 and substituted back into N of Equation 3.63.

This split-step Fourier based numerical approach can provide a good approximation to the final solution if the step size of operators in each domain is chosen properly. The analysis of the nonlinear effects observed in the semiconductor waveguides in this thesis is mainly based on the simulation of these coupled equations. These will provide the basic understanding of the nonlinear properties and pulse propagation in the semiconductor waveguides.

Chapter 4

Semiconductor waveguide fabrication and characterisation

4.1 Introduction

In this chapter, the fabrication of the semiconductor waveguides is discussed in detail. I will begin with the fabrication of the semiconductor optical fibre. Next, the fabrication of planar-based semiconductor waveguides is presented using the most common silicon-on-insulator (SOI) platform as an example. The main part of this chapter will comprise of comprehensive studies of both these waveguide platforms from the near-infrared to the mid-infrared (mid-IR) regime. The experiments include material characterisation using Raman analysis and scanning electronic microscope (SEM) to establish material quality. These are followed by measurements of the optical transmission properties at specified wavelengths for the different waveguides. These experiments provide useful information for the subsequent nonlinear characterisations of the waveguides and also help us optimise the fabrication conditions to achieve the low loss waveguides in the mid-IR wavelength. Specifically, I present the first investigations of the mid-IR light transmission properties of semiconductor wavaguides with different geometries and materials including polycrystalline silicon (p-Si) fibre, hydrogenated amorphous silicon (a-Si:H) fibre, hydrogenated amorphous germanium (a-Ge:H) fibre and the newly emerged germanium-on-silicon (Ge-on-Si) planar waveguides.

4.2 Semiconductor optical fibre fabrication

The semiconductor core, silica clad fibres can be fabricated via various methods as discussed in Section 2.3. The fibres used in this PhD project were fabricated via the high pressure chemical vapor deposition (HPCVD) technique [30], Figure 4.1 shows a

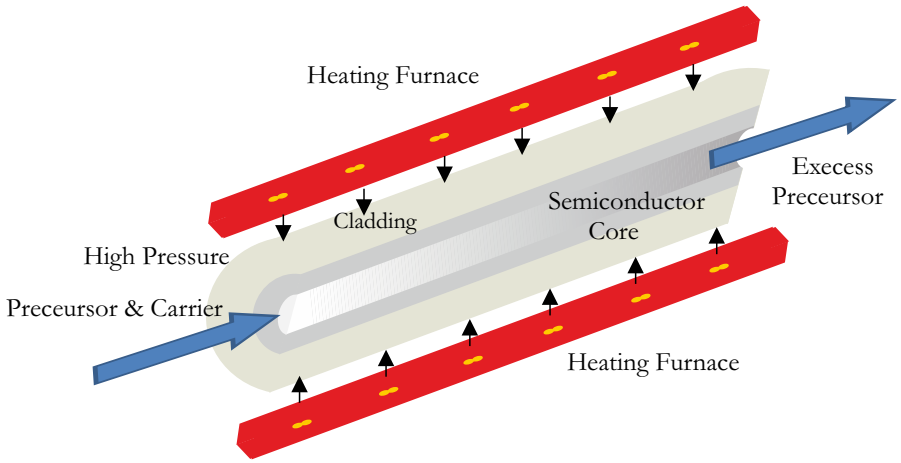

Figure 4.1: Illustration of the HPCVD technique for semiconductor core fabrication.

cross-sectional schematic of this process. In the HPCVD deposition process, the pores of the silica capillaries act as chemical reaction chambers in which the chemical precursors flow through the fibre's length assisted by the high pressures. The reactions are then initiated thermally using a tube furnace to deposit the material onto the capillary walls up to the point when the pore is completely filled [110]. Silica capillaries make excellent templates for materials deposition as their mechanical strength allows them to withstand the extreme deposition conditions required for the HPCVD method, they have especially smooth internal surfaces ($< 0.1\,\text{nm}$ RMS), and the dimensions of the internal hole can be easily scaled to the desired core size. The deposition process is conducted by forcing a mixture of a precursor gas, i.e. silane (SiH_4) for silicon core or germane (GeH_4) for germanium core, to flow through the central hole. Typically, the carrier gas is helium or hydrogen at $\sim 40\,\text{MPa}$ [30, 111] and the ratio between the precursor and carrier is approximately $1:19$. As an example, for a silicon deposition, the temperature setting could result in three distinct phases: P-Si, a-Si, or a-Si:H. The temperatures are typically set between $360-520\,^{\circ}\text{C}$ so that they are below the nucleation temperature $520\,^{\circ}\text{C}$ of silicon [112, 113]. This ensures that the material deposits in an amorphous state so that it adheres smoothly to the silica walls, thus minimizing the roughness at the silicon-silica interfaces. If required, crystallization to polysilicon can be performed after the deposition process via annealing at temperatures up to $1325\,^{\circ}\text{C}$ [119]. It has been found that by keeping the temperatures below $450\,^{\circ}\text{C}$, the out diffusion of hydrogen can be suppressed, resulting in the deposition of a-Si:H. As discussed in Section 2.2, the incorporation of hydrogen is important as it results in reduced absorption losses [114].

Using this HPCVD technique, our collaborators in PSU are able to routinely deposit a variety of elemental and compound semiconductors over lengths of several centimetres into the internal holes of the capillaries. So far, this technique has been able to fabricate silicon fibres with core sizes ranging from $1.7-6\,\mu\text{m}$ with excellent optical properties. In this thesis, our efforts focus on the a-Si:H material because of its advantageous nonlinear

properties, and low loss fibres are achievable in this phase. Another phase of silicon core fibre (p-Si) will also be described in this chapter. Finally, an example of a a-Ge:H core fibre is included for comparison although the development of these fibres is still in its infancy stage.

4.3 Planar-based semiconductor waveguide fabrication

In this section, a brief introduction to the fabrication of the planar semiconductor waveguides using the SOI platform is provided as an example. The SOI structure is composed of a uniform layer of SiO_2 sandwiched between a thick (hundreds of microns) silicon substrate and a thin surface layer of crystalline silicon [115]. The thickness of the crystalline silicon is typically 200 nm and the buried silicon dioxide layer is in the range of $1-7\,\mu$m, but this value can be varied significantly depending on the fabrication process. There are several methods that can be used for the manufacture of SOI substrates, of which the most common ones are separation by implanted oxygen (SIMOX), bond and etch-back SOI (BESOI) and wafer splitting. The detailed fabrication process can be found in the Ref. [87].

The layout of SOI waveguides were designed in the L-edit software. The waveguides structures were typically defined using electron-beam (e-beam) lithography [116] and reactive ion etching (RIE) [117]. In general, fabrication of a waveguide requires the following steps: wafer preparation, lithography, silicon etching and chip dicing. After preparation, the wafer will be free from particle contaminants and has been desorbed of any moisture and the wafer is immediately coated with a ZEP 520A photoresist. Following spinning the wafer is baked at 180 °C for 3 minutes. The wafer is written in the JEOL JBX-9300FS e-beam machine. A typical writing time is 15 minutes for a 3 cm × 2 cm chip filled with waveguide structures. Etching to define the waveguides then requires the controlled removal of material from the silicon wafer surface via a chemically reactive using SF_6 (25 sccm), C_6F_8 (45 sccm) chemistry at a pressure of 2 Pa and a temperature of 15 °C. After these steps, the wafer is diced into different chips. Other semiconductor wafer platforms like germanium, can be fabricated by a similar process flow, as will be described later in Section 4.4.4.

4.4 Optical transmission characterisation

In semiconductors, the intrinsic absorption mainly arises from the free electrons and resonances associated with bound electrons and ions. The extrinsic absorption mechanism is related to the material impurities and defect centres. Extrinsic scattering is presumed to come from stress birefringence, grain boundaries, precipitates, cracks and voids due

to thermal expansion mismatch, surface roughness, and diameter fluctuations. In order to reduce the losses, much of the interest has focused on optimising the fabrication conditions to minimize the extrinsic absorption and scattering. Hence, measuring the optical transmission properties of the semiconductor waveguides will give information for the material quality after fabrication. As the losses due to scattering are wavelength dependent, measuring the wavelength dependent values for the loss could provide information about which mechanisms are dominant in a specific waveguide. In the following sections, the loss mechanisms will be analyzed for the two types of semiconductor waveguides based on the experimental results.

For the semiconductor optical fibres, as discussed in Section 4.2, fibres with a variety of core materials can be fabricated by changing the deposition parameters and the precursors. The silica capillaries exhibit a surface roughness of 0.1 nm RMS [118], allowing the semiconductor core to assume the same surface quality during deposition [119]. Hence the surface scattering is expected to be less pronounced in the semiconductor core, silica cladding optical fibres. Volume and surface imperfections are difficult to isolate quantitatively, though the total scatter from a waveguide can be observed by measuring the top-scattered light along the waveguide and fitting the intensity decay with an exponential curve.

In contrast, the surface roughness of the semiconductor planar waveguides can be as large as 3 nm RMS. Both waveguide size and propagation loss should be taken into account when evaluating the performance of a specific type of waveguide. According to the loss mechanism, propagation losses can be divided into two parts: (i) the intrinsic loss (such as defect and carrier absorption) and (ii) the extrinsic loss (such as sidewall scattering and radiation into the substrate). The former is the main loss mechanism for doped waveguides, while the later one becomes significant when the sizes of waveguides are very small (such as the SOI nanowire waveguides), due to the non-negligible field intensity at the silicon surface and the roughness at the interface. In particularly, sidewall roughness introduced by imperfect etching, will result in scattering at the interface between waveguide core and cladding, which becomes a major source of propagation loss. This scattering loss, typically around $0.2 - 3.0\,\mathrm{dB/cm}$ for SOI waveguides has been analysed by Yap *et al.* [120]. In this work, the absorption caused by the doping is not considered as the semiconductor materials in the waveguides investigated in this thesis are intrinsic.

4.4.1 Semiconductor waveguide preparation

4.4.1.1 Semiconductor optical fibre preparation

The quality of the fibre endface is of the utmost importance for free space light coupling into the semiconductor fibre core. Thus pre-treatment of the fibre facets is needed

before the transmission can be investigated. As the mechanical differences between the semiconductor core and the silica cladding is large, the standard cleaving techniques cannot be used for the semiconductor core fibre. Instead, a conventional fibre polishing technique is introduced to prepare the facet of a semiconductor core fibre mounted in a host thicker capillary, shown in the inset of Figure 4.2. The outer dimension of the silica capillary is normally around 125 μm and the fibre length under test is on the orders of centimetres. A low melting point wax is used to secure the fibre to the capillary. The wax is heated beyond its melting point ($\sim$ 63 °C), so that it can surround the semiconductor fibre inside the outer capillary. The mounted fibre is then immediately cooled down to solidify the wax. The fibre is polished using three different grade lapping films with reducing particles sizes (3 μm, 1 μm and 0.3 μm) attached onto the surface of the film. The polishing equipment and accessories are very similar to those used for standard silica fibres and the polishing machine used in this project is ULTRAPOL polishing machine manufactured by Ultratec. Following the mounting and polishing procedure, the semiconductor fibre are checked under a microscope and the cross-section and longitudinal images are given in Figure 4.2.

4.4.1.2 Planar based semiconductor waveguide preparation

Although grating couplers were commonly used for coupling light into planar waveguides, end-fire coupling approaches were chosen in this project as high peak power pulse will be used for the nonlinear characterisation. Similar to the semiconductor fibres, the waveguide end facets must be cleaved or polished to improve the facet quality. Cleaving approaches were used more often as they are fast and can produce good quality facets. However, the drawback of this method is that it is not very reliable and the chips can be damaged. Although polishing is time consuming and could cause some inconsistency between the facets of different waveguides, it is used when the difference in hardness

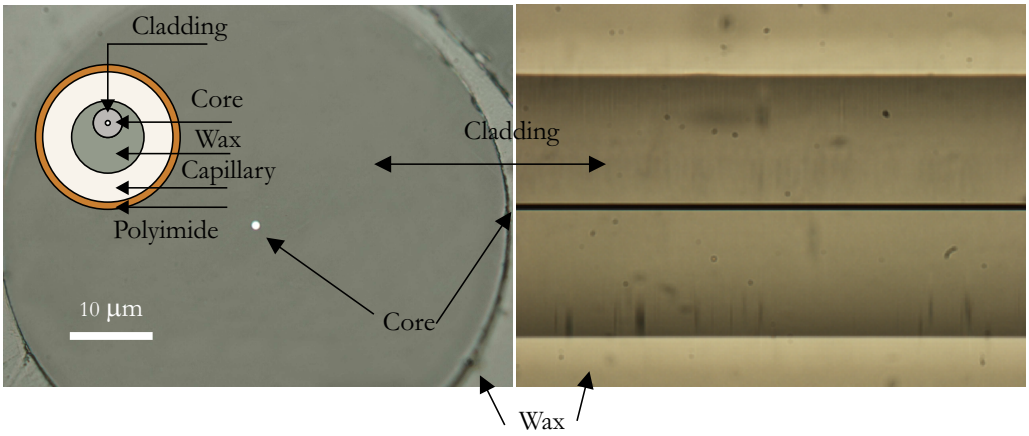

Figure 4.2: Semiconductor core fibre mounted into a capillary for polishing. The cross-section (left) and image from the top (right).

of the core/substrate material is too large as cleaving will not give good facet quality. Polishing is performed by lapping with rotating abrasive discs against the chip edge, thus smoothing the chip facet. A Metaserv 2000 Grinder/Polisher machine is used for this polishing. A protective layer is applied to the top of the chip surface during the polish process. For this project, Buehler mounting wax has been used for this purpose. The wax is heated to melt at temperatures above $\sim 100\,^{\circ}$C. When the top sides of the chip surface are evenly covered by the wax, the back surface (without waveguides) is affixed to a metal block designed as a support during the polishing. A piece of dummy silicon wafer is similarly attached to the opposite side of the metal block to balance the polish. Different discs were used for the polishing (silicon carbide for coarse polish and Al_2O_3 for fine polish). Once the polishing procedure is finished, the semiconductor waveguide is cleaned, ready for optical characterisation.

4.4.2 Linear loss measurement setup

The characterisation of the transmission properties is undertaken using the experimental setup shown in the Figure 4.3. Different laser sources were chosen depending on the waveguide types under test and will be described separately for each measurement. A variable attenuator was used to control the power coupled into the waveguide from the laser sources for linear loss measurements. The laser beam was launched into the waveguide core via a free space coupling lens and a second objective was used to capture the transmitted light and focus it onto a power meter or some other diagnostic equipment. A beam splitter (90/10) was placed before the input to capture the reflected light from

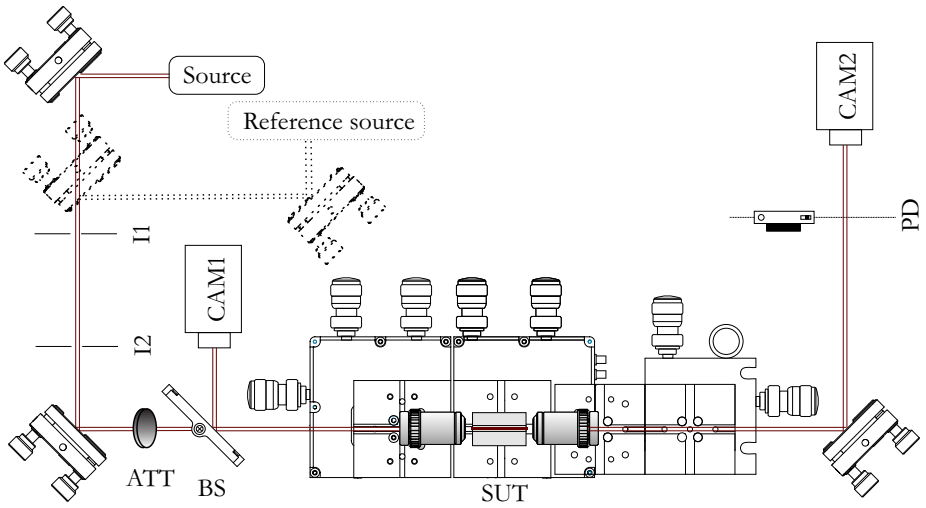

Figure 4.3: Experimental set-up for loss measurements. Iris (I1 & I2), camera (CAM), attenuator (ATT), beamsplitter (BS), sample under test (SUT), and optical power detector (PD). The dash lines represent the beam path of a near-infrared light when aligning the mid-IR wavelengths.

the waveguide input face with an imaging cameras (either a CCD or Pyroelectric array camera (Spricon Pyrocam™ III) depending on the operation wavelength of the laser source). This camera could monitor when the light was incident on the semiconductor core because of the higher refractive index induced larger reflection. The use of this camera ensured efficient coupling into the centre of the core so that the fundamental mode was primarily excited. The nano-positioning stages were adjusted by a set of three piezo-controllers to optimize the coupling conditions. The optical objective lenses used in the measurements were different for different wavelengths. Typically a fused silica objective with 0.65 NA (4.6 mm focal length) was used for wavelengths up to 2.5 μm. Either a ZnSe lens with a focal length of 6 mm or an aspheric chalcogenide lens with a focal length of 1.87 mm were selected for longer wavelengths, depending on the waveguide dimension. Different optical power detectors were also selected for the different wavelength regions. Germanium or indium gallium arsenide based photodetectors were used for wavelengths under 1.8 μm. A lead selenide (PbSe) pre-amplified photoconductive detector (Thorlab PDA20H) or a thermal power sensor (Thorlab S302C) were used for longer wavelengths, chosen by the power range measured. As the mid-IR wavelength is invisible to a convectional CCD camera and the resolution of the Spiricon mid-IR camera is not enough to image the input facet, a reference beam path using a near-infrared wavelength of ($\sim$ 1.5 μm) is used to aid the coupling, as shown by the dashed lines in Figure 4.3.

Using this configuration, the linear losses of the semiconductor waveguides were characterized using the cutback method [121]. The cutback method can eliminate the influence of additional losses (e.g. coupling loss, lens loss and bend loss) by comparing the optical transmission through a longer piece of waveguide to that of a shorter length. For semiconductor optical core fibres, the cutbacks were undertaken by reducing the fibre length through polishing. While for planar waveguide, an effective cutback method was applied by comparing the transmitted power through waveguides of different lengths, thus the loss value can be determined. This effective cutback method could avoid the error introduced through varying end facet quality when polishing off a certain waveguide length. However it requires consistence coupling to different waveguides. It is worth noting that other methods can also be used to measure the waveguide loss, i.e. Fabry-Perot cavity. In this technique, the Fabry-Perot resonances are tuned through precise temperature control using a narrow linewidth laser source and consequently the loss value can be extracted based on the Fabry-Perot fringes [122]. In this work, this method was not chosen because I did not have access to a narrow linewidth source at the mid-IR wavelengths. However, as the losses of the Ge-on-Si waveguides are on the order of 3 dB/cm, so the effective cutback method was deemed sufficient for this work. Figure 4.4 illustrates the principles of these two cutback methods employed for the fibre and chip-based platforms.

The linear loss can be simply calculated using the equation below:

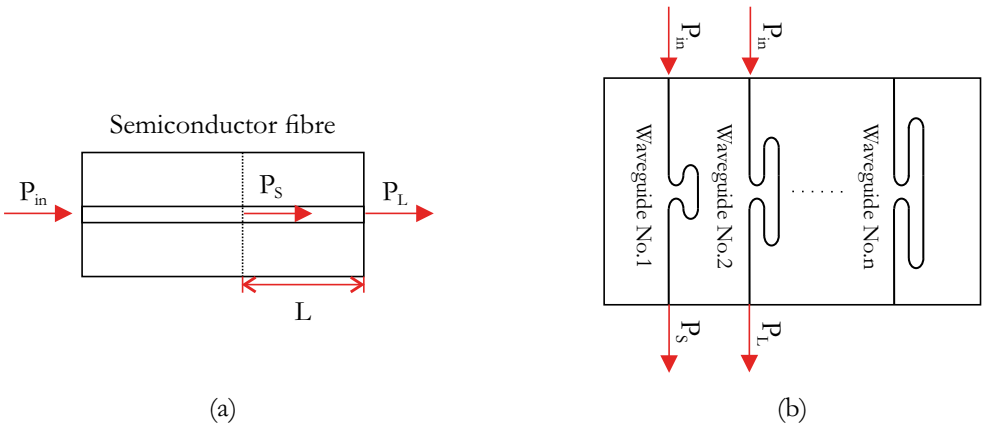

Figure 4.4: (a) Cutback variables for semiconductor core fibre. (b) Effective cutback method used for the semiconductor planar waveguide. Bend number and radius is the same for all waveguides.

$$\alpha_{L} = -10\log_{10}\left(\frac{P_{L}}{P_{S}}\right)/L. \tag{4.1}$$

Here P_L is the output power of the longer length, P_S is the output power of the short length and L is the length that was cut off or the length difference.

4.4.3 Semiconductor optical fibre characterisation

The main goal of this thesis is to investigate suitable waveguide platforms for the mid-IR wavelength, thus this work has extended these systematic experiments on the optical properties of the semiconductor optical core fibres into longer wavelength regime. These results could also help our collaborators optimise the fabrication conditions in the pursuit of lower fibre loss. The basic linear optical properties measured in this chapter will provide useful information for the investigation of the mid-IR nonlinear effects in the following chapter.

4.4.3.1 Hydrogenated amorphous silicon core fibre

As discussed in Section 2.2.1, the a-Si:H material has been demonstrated as a good material for low loss semiconductor waveguides due to the saturation of dangling bonds by hydrogen [123]. For this reason, the optical loss values of a-Si:H waveguides are approaching similar numbers with those achieved in crystalline silicon (c-Si) waveguides [124]. Since the first demonstration of the semiconductor core fibres in 2006 [30], much

Table 4.1: Deposition conditions and linear losses (at 1.55 μm) of the fabricated a-Si:H fibres.

a-Si:H fibre	Carrier	Temperature gradient (°C)	Loss value (dB/cm)	Core diameter (μm)
A	H_2	362–399	1.50	6
B	H_2	350–373	1.60	6
C	H_2	353–394	1.98	6
D	H_2	362–403	2.10	6
E	H_2	342–347	2.90	6
F	H_2	377–409	3.30	6
G	H_2	376–406	3.40	6
H	H_2	350–374	3.50	6
I	H_2	387–415	3.70	6
J	H_2	362–403	4.35	6
K	H_2	394–425	5.10	6
L	H_2	360–394	6.77	6
M	H_2	350–376	2.80	1.7
N	H_2	373–375	3.10	1.7

of the efforts in our research group have focused on developing low loss silicon core fibres for nonlinear photonics applications. So far, the lowest loss silicon core fibre (0.8 dB/cm at 1.55 μm) has been fabricated from a-Si:H material [50]. Hence, a-Si:H is the main choice of core material for the optical fibres investigated in this thesis. Figure 4.5(a) shows a Raman spectrum of a a-Si:H fibre core. This spectrum exhibits features indicative of a-Si with the presence of hydrogen (evidenced by the mode in the inset). The vibrational modes can be identified given their shift and energy. The strong broad peak around 480 cm^{-1} corresponds to the transverse optical (TO) mode and the two weaker subsidiary peaks are associated with the longitudinal acoustic (LA) and longitudinal optical (LO) modes of amorphous silicon [125]. For amorphous materials the mode resonances are broad and hence overlap as observed in Figure 4.5(a).

A large number of a-Si:H core fibres were fabricated at Pennsylvania State University and characterised in ORC. Table 4.1 summarises the key deposition details of the a-Si:H core fibres in the past three years. In this thesis, the linear losses characterisations of a-Si:H core fibres were first conducted using a laser diode at 1.55 μm, as the fibre characterisation technique was well established at this telecom wavelength. Although the relationship between the transmission loss and the deposition condition is extremely complex, a brief guideline could be obtained for the optimization of the fabrication process. Following the previous work in our group, the carrier gas was replaced by hydrogen from helium because the incorporation of additional hydrogen inside the fibre core is expected to reduce the transmission loss. The temperature gradient of the furnace is another important parameter for the fibre deposition. The middle section of the furnace must be set at a higher set temperature to ensure that the temperatures at the

edges of the furnace (which will be lower) are above the threshold for the deposition to occur. The temperature range was recorded for each deposition and listed in Table 4.1. As can be seen from linear loss results, it was found that a peak deposition temperature between $350 - 450\,^{\circ}\mathrm{C}$ usually produces fibres with good optical properties, while most fibres deposited out of this temperature range exhibited losses on the order of tens of dB/cm, or higher. Hence, all of the a-Si:H core fibres listed in Table 4.1 are fabricated within this temperature range. As can be seen from the Table 4.1, lower fabrication temperatures ($< 400\,^{\circ}\mathrm{C}$) normally produces lower loss values but will require longer deposition time. With the project ongoing, our collaborators at Pennsylvania State University can fabricate a-Si:H with consistent loss properties in the range of $1-7\,\mathrm{dB/cm}$ using the HPCVD technique. The next step of the project is to investigate the nonlinear effects in these highly nonlinear fibres. Hence, the nonlinear absorption and refraction measurements were conducted, will be described in Chapter 5. However, it is worth noting that it was the a-Si:H core fibres which exhibited a clean output spectrum during these measurements that were chosen for further optical investigations, as this was a good indication that the fibre core consisted of a uniform material. Overall, the fibres chosen in this thesis exhibited good optical properties both in terms of linear and nonlinear properties. After the optical characterisations, the deposition parameters of the a-Si:H fibres with good optical properties were feedback to the fabricators to help optimise of the fabrication process.

The characterisations were started in relatively large fibres with the core diameters of $6\,\mu\mathrm{m}$, then move to small fibre with the core diameter of $1.7\,\mu\mathrm{m}$, for which the coupling is more difficult and a $63\times$ was required for coupling this fibre. It is worth noting that by putting continuous efforts to optimise the deposition conditions, the losses of the $1.7\,\mu\mathrm{m}$ core fibres could drop to $\sim 3\,\mathrm{dB/cm}$, which is only slightly higher than those of the well developed $6\,\mu\mathrm{m}$ core fibres. These fibre will be used to demonstrate nonlinear application and the details will be given in Section 5.5.

Next characterisations of the transmission losses for two selected low loss a-Si:H core fibres (fibre D and fibre L) were then extended to the mid-IR regime. Two laser sources were used: (i) a Ti:sappire pumped femtosecond optical parametric oscillator (OPO Model Radiantis OPIUM) for the near infrared measurements spanning $1.45 - 2\,\mu\mathrm{m}$ and (ii) a continuous wave (CW) tunable Cr^{2+} : ZnSe laser (IPG Model SFTL-Cr-ZnSe-2300-1000) which covered the mid-IR wavelengths of $2 - 2.7\,\mu\mathrm{m}$. The loss values over the entire wavelength range are shown in Figure 4.5(b). During the measurements, the input and output powers were both monitored using power meters. In order to avoid the effects of nonlinear absorption when using the OPO, which had a pulse duration of 200 fs (FWHM) and a repetition rate of 80 MHz, the average coupled power was kept below $100\,\mu\mathrm{W}$. These results follow the same trend of decreasing loss for increasing wavelength observed in earlier measurements of the silicon core fibres [114], and in this amorphous material the main contributions to the losses are likely to be due to a combination

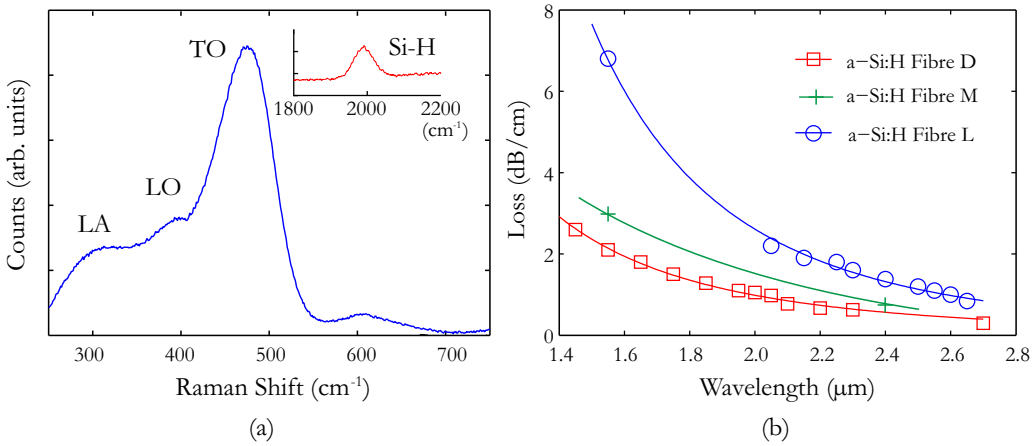

Figure 4.5: (a) Raman spectra of a-Si:H core fibre, showing the longitudinal acoustic (LA), longitudinal optical (LO), and transverse optical (TO) modes of the amorphous material. (b) Linear loss measurements as a function of wavelength.

of scattering from density fluctuations and some electronic absorption. The wavelength dependent losses exhibit good agreement to the λ^{-4} dependence associated with Rayleigh scattering, as shown in Figure 4.5(b).

The losses for fibre D are some of the lowest reported for a-Si:H waveguides that are usually within the range: $1-10\,\mathrm{dB/cm}$ at telecoms wavelengths [26, 126], and the value of $2.1\,\mathrm{dB/cm}$ at $1.55\,\mu\mathrm{m}$ is the lowest we have measured in a a-Si:H core fibre of several centimeters in length. Moreover, the losses in the range $2-2.3\,\mu\mathrm{m}$ are the first reported for this material in the mid-IR regime, and are all $\lesssim 1\,\mathrm{dB/cm}$, reducing to $0.62\,\mathrm{dB/cm}$ at $2.3\,\mu\mathrm{m}$. Additional measurements undertaken at $2.7\,\mu\mathrm{m}$ (the limit of the $Cr^{2+}:ZnSe$ laser) revealed that the losses continued to decrease down to $0.29\,\mathrm{dB/cm}$ which is the lowest value measured in the silicon core fibres.

For fibre sample M, the linear loss was also measured at $2.4\,\mu\mathrm{m}$, which is $0.8\,\mathrm{dB/cm}$, as shown in Figure 4.5(b). This is the record low loss for the $1.7\,\mu\mathrm{m}$ core a-Si:H fibre. Despite the small core fibre still possing higher loss than the frequently fabricated $6\,\mu\mathrm{m}$ core a-Si:H fibre, the less than $1\,\mathrm{dB/cm}$ in the mid-IR regime and significant reduced mode area make it promising for nonlinear applications.

4.4.3.2 Polycrystalline silicon core fibre

Despite the growing popularity of a-Si:H for nonlinear photonics, p-Si is still the favoured material choice for certain applications, i.e., Raman amplification as its level of crystallinity is close to c-Si. The p-Si core fibres investigated in this thesis are fabricated by post processing the deposited a-Si core fibre using thermal annealing [127, 128, 129].

The resulting fibres can have much smaller core diameter than those fabricated by the drawing methods which is critical for nonlinear applications.

Previous p-Si core fibres were fabricated from a-Si using a single step annealing process at a high temperature (1325 °C). In this thesis, a p-Si core fibre made using a newly developed two step annealing process was investigated. The fibre was first annealed at 530 °C for 3 days and then followed by high temperature annealing at 1300 °C for only 10 minutes. As discussed in Section 4.2, silicon begins to crystallise at temperatures around 520 °C, so this is the minimum temperature at which the fibre core can be annealed to form a p-Si core. By using a low temperature just above the nucleation temperature as the first annealing step, fewer nucleation points are formed, which can eventually grow to form big grains during the second high temperature annealing. The second anneal time must be kept short as silica undergoes a glass transition around 1300 °C, thus annealing above this temperature for long time would lead to a deformation of the cladding. In contrast to most planar electronic devices, HPCVD grown amorphous silicon optical fibres can withstand temperatures as high as 1300 °C for $\sim$ 10 minutes without cladding deformation. Thus I expect this two-step annealing process should be better for the formation of large grains in these fibres, ultimately decreasing the fibre loss.

In order to investigate the material quality of the annealed p-Si core fibre, Raman spectra of the p-Si core fibre samples and a crystalline silicon reference were collected using an excitation wavelength of 633 nm. After high temperature annealing all of the samples are highly crystalline, as shown in Figure 4.6(a) where the spectra are compared to a standard single crystal silicon. The silicon single crystal peak has a Lorentzian FWHM of 2.6 cm^{-1}, centered at 522 cm^{-1}. Our sample B (annealed at 530 °C and 1325 °C) exhibits a peak also centered at 522 cm^{-1} with a Lorentzian FWHM of 3.0 cm^{-1}. This

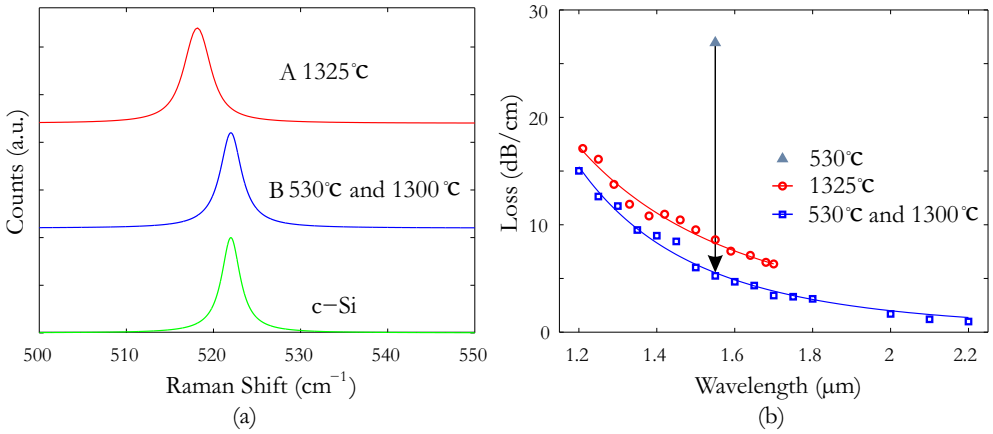

Figure 4.6: (a) Raman spectra of polycrystalline silicon core after annealing at different temperatures compared to standard single crystal silicon with FWHM of Lorentzian fits. (b) Linear loss measurements as a function of wavelength. The red curves were reproduced from [114].

is only slightly broader than the reference which indicates this sample is very close to single crystal silicon. Fibre sample A, which was only annealed at 1325 °C, has a peak with a FWHM of 3.3 cm^{-1} at a position of 518 cm^{-1} much further from the singe crystal reference. It is clear that this sample exhibit a broader linewidth and larger shift in the peak position associated with large tensile stress.

Optical transmission loss of the two step annealed sample B was measured at a telecommunication wavelength of 1.55 μm before and after the high temperature annealing. As shown in Figure 4.6(b), annealing at only 530 °C gives a high loss of 27 dB/cm. This is because at this point, the sample only has a few grains and a lot of defects. Moreover a significant amount of amorphous material is still present with lots of dangling bonds. After the high temperature annealing, the loss of this sample comes down significantly to 5.2 dB/cm, which is the lowest value recorded for a small core crystalline silicon fibre to date.

The characterisation of the optical transmission in sample B were then extended over a range of wavelengths into mid-IR regime. Two laser sources including a supercontinuum (Fianium SC-400) and a CW tunable Cr^{2+} : ZnSe laser (IPG Model SFTL-Cr-ZnSe-2300-1000) were used to access wavelengths from $1.3-1.8\,\mu$m and $2-2.2\,\mu$m respectively. The output power of the supercontinuum source was kept very low to minimize the nonlinear effects in the p-Si core fibre. Figure 4.6(b) shows the linear loss as a function of wavelength. The loss of the p-Si core fibre was fitted with a λ^{-4} dependency associated with Rayleigh scattering. The good agreement between the experimental results and the Rayleigh fit indicates the loss is primarily influenced by density fluctuations as expected for a polycrystalline material. The lowest measured optical loss is 0.99 dB/cm at $\lambda = 2.2\,\mu$m, the lowest value reported for a small core silicon fibre. The linear loss of a p-Si core fibre sample A is also plotted in the same figure for comparison [114]. It is obvious to see the reduction of linear loss across the entire wavelength region (e.g. an improvement of more than 4 dB/cm at 1.55 μm) for Fibre B. It can be attributed that higher crystallinity (larger crystal grains) and less defects are achieved by the two-step annealing process.

The low optical loss observed for these p-Si core fibres annealed in a two-step process should improve their performance in nonlinear applications, allowing for the development of compact all optical modulators, switches and Raman amplifiers that can operate well into the mid-IR wavelength regime.

4.4.3.3 Germanium core fibres

Germanium core fibres have been fabricated previously by both the HPCVD and molten core drawing (MCD) methods. However, the loss at 2 μm are still very high using both methods. In this thesis, I present the linear loss characterisation of an amorphous

germanium core fibre that has been fabricated to include a higher hydrogen content than previous attempts from 2 to 2.7 μm. The germanium is deposited at a lower temperature of 290 − 295 °C as the Ge-H bond is not as strong. Similar to the a-Si:H material, the incorporation of hydrogen is important to passivate the dangling bonds of the amorphous material.

As shown in Figure 4.7(a), the core material was characterized using micro-Raman spectroscopy. The broad peak in the Raman spectrum at around 280 cm^{-1} indicates the amorphous nature of the germanium core. This peak is close to the transverse optical Raman resonance of 278 cm^{-1} for amorphous germanium [131]. Evidence of hydrogenation is provided by the peak at $\sim$ 1900 cm^{-1}, as shown in the inset of Figure 4.7(a), which is associated with the Ge-H stretching mode.

Optical loss measurements of a-Ge:H fibres with a core diameter of 5.6 μm were performed over a range of mid-IR wavelengths. Using a continuous wave (CW) tunable Cr^{2+} : ZnSe laser (IPG Model SFTL-Cr-ZnSe-2300-1000), which covered the range of 2 − 2.7 μm. Wavelengths below 2 μm were not considered as they are too close to the band edge absorption. As germanium is invisible to the CCD cameras previously used in the characterisations of silicon fibre, a Spiricon camera was used to image the beam. The loss measurement method was similar to that used for silicon fibre in Section 4.4.3.1. The final transmission losses are presented in Figure 4.7(b) (Fibre B) showing a decrease in loss for increasing wavelength. Previous measurements conducted by Metha are also shown for comparision (Fibre A) [130]. Fibre B is fabricated with more hydrogen inside the fibre core due to the lower fabrication temperature (the deposition temperature for Fibre A is $\sim$ 300 °C). The a-Ge:H core fibre B has an optical loss of 25 dB/cm at 2 μm which is significantly lower than $\sim$ 40 dB/cm loss of fibre A. Compared to the previous fabricated a-Ge:H fibres, the results shows that the loss has been reduced by more than a factor of 10 at this wavelength. Although at these wavelengths the measured losses

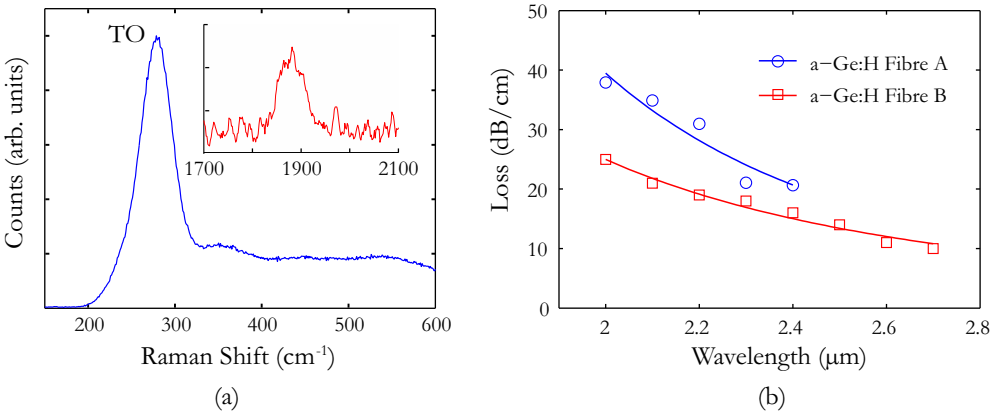

Figure 4.7: (a) Raman spectra of a a-Ge:H core fibre, the figure is reproduced from [130]. (b) Linear loss measurements as a function of wavelength.

are relatively high, they are comparable to those of the early amorphous silicon optical fibres measured at $\sim 1.55\,\mu$m, which have since been reduced by increasing the amount of hydrogen incorporation [132]. Also, the trend of decreasing loss for increasing wavelength indicates the loss could be further reduced at longer mid-IR wavelengths as the minimum loss is 10 dB/cm at $2.7\,\mu$m.

4.4.4 Germanium-on-silicon waveguide

The Ge-on-Si waveguides were briefly introduced in Section 2.5 as suitable candidates for the mid-IR wavelength region owning to their broad transmission window. For this project, the optical characteristics of the Ge-on-Si waveguide are investigated for the potential nonlinear applications in the mid-IR wavelength regime. The Ge-on-Si waveguides used in this project have been fabricated by both my colleagues from the Silicon Photonics group in University of Southampton and some in collaboration with the University of Ghent. The work presented here is the first wavelength dependence characterisation of these newly proposed waveguides for the mid-IR wavelength.

The starting Ge-on-Si wafers were fabricated by epitaxially depositing a micrometre thick germanium layer onto a silicon substrate using a chemical vapour deposition (CVD) method [133]. The germanium film is deposited on the silicon substrate at 450 °C using a precursor mixture of germane and hydrogen (1% GeH_4 in H_2). There is a 4.2% mismatch in the lattice constants between silicon and germanium which introduces high threading dislocation (TD) at the silicon-germanium interface. The TD will cause absorption of light which is one of the main mechanisms contributing to the optical loss. In order to reduce the defects, the Ge-on-Si wafers were subsequently thermally annealed at 850 °C for 3 minutes in N_2. During the annealing process, the TD of the germanium film reduces from $2\times10^{10}\,\mathrm{cm}^{-2}$ to approximately $10^7\,\mathrm{cm}^{-2}$ (or $10^8\,\mathrm{cm}^{-2}$) depending on the thickness [134].

The second step of the fabrication process is lithography and etching. To fabricate the patterned waveguides a SiO_2 hard mask was defined, which was deposited via plasma enhanced CVD, then patterned via e-beam lithography and RIE using an Ar/CHF_3 plasma. The photoresist was subsequently stripped and a further RIE step performed (SF_6/CHF_3 plasma) to form the waveguides. Finally, the SiO_2 mask was removed using a HF bath and the samples were cleaned and cleaved. Cleaving was chosen for the Ge-on-Si waveguide as the germanium layer was easily contaminated by the wax used during the polish process. Currently work is on-going to replace wax with new materials e.g. photoresistors to avoid the contaminations. I expect this approach will give a consistent facet quality in future.

The Ge-on-Si wavegudes investigated in this thesis were designed to have a rib structure with selected dimensions listed in Table 4.2. This is because the rib waveguide can be

Sample	Height (μm)	Etch depth (μm)	Width (μm)	Structure	Fabrication group
A	1.0	1.0	2.25	Rib	Ghent
B	1.0	1.0	1.75	Rib	Ghent
C	2.0	1.2	2.25	Rib	Soton

Table 4.2: Ge-on-Si waveguide parameters. Abbreviations: University of Ghent (Ghent), University of Southampton (Soton).

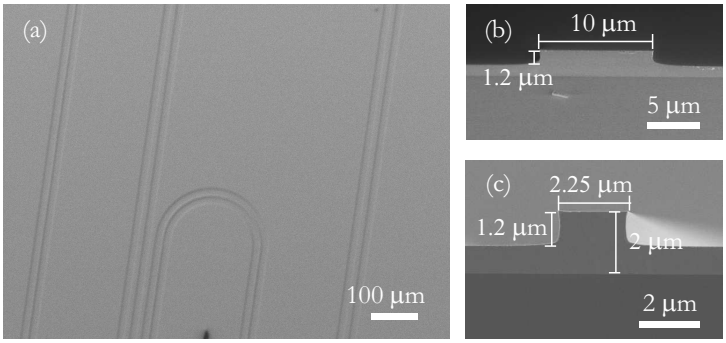

Figure 4.8: (a) SEM micrograph of Ge-on-Si rib waveguides. Here the straight sections correspond to the 10 μm wide coupling tapers, and the curved section is the smaller 2.25 μm wide core. (b) Cross-section of the input taper and (c) the core.

made to be larger for single mode conditions compared to the strip waveguide, thus making it easier to fabricate and offers greater tolerance of fabrication errors [135]. Also as the light mode extended to the slab region of the waveguide, its interaction with the etched sidewall is less and thus the transmission loss is lower. To facilitate coupling, input and output tapers were fabricated at each end, with a maximum width of 10 μm. Waveguides of different lengths were incorporated on the chip by introducing four identical bends, of varying separation, in each core section. Furthermore, the bends were designed to have a relatively large radius of 100 μm (see Figure 4.8), which ensured that their contribution to the overall losses was minimal. Figure 4.8 shows a scanning electron microscope (SEM) image of the patterned waveguides, from which both the wide tapered input and waveguide core (with bends) can be identified. SEM cross-sectional images of the input facet and waveguide core are then displayed in Figure 4.8(b) and 4.8(c), respectively, showing that the rib structure is well formed.

Linear loss measurements of the Ge-on-Si waveguides were performed using various mid-IR sources over the wavelength range $1.9 - 3.8\,\mu$m. The initial measurements were conducted over the short wavelength range of $1.9 - 2.6\,\mu$m using the tunable CW Cr^{2+}:ZnSe laser source (IPG Model SFTL-Cr-ZnSe-2300-1000). For these wavelengths the light could be launched into the core using a 63 $\times$ silica microscope objective (0.85 NA), which allowed for optimal coupling into the fundamental TE mode of the taper, and hence waveguide core, which was multi-moded for wavelengths $< 3\,\mu$m. The output was

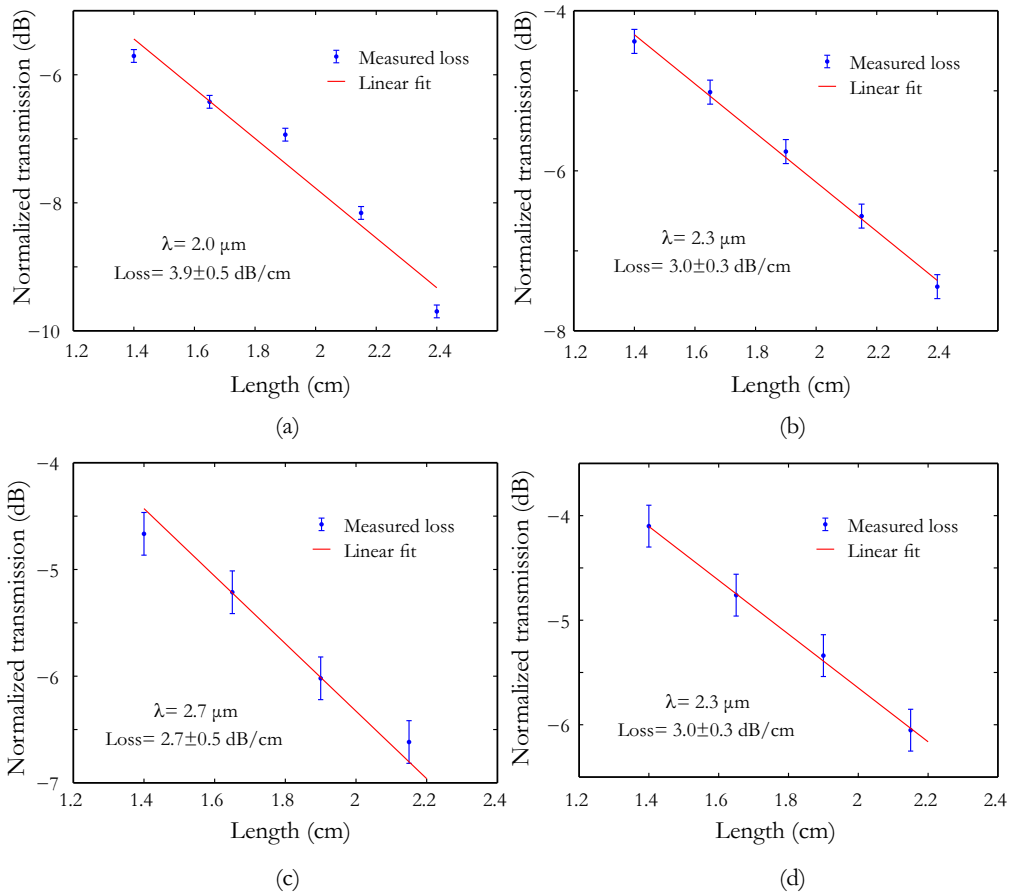

Figure 4.9: Normalized transmitted power as a function of waveguide length for selected wavelengths for the cut-back measurements in Ge-on-Si waveguide sample C.

then collected via a ZnSe objective with a 6 mm focal length and measured using a PbSe pre-amplified photoconductive detector.

Figure 4.9 presents the results of the effective cutback method for sample C. The normalized transmission through the Ge-on-Si waveguide are shown for different wavelengths over several waveguide lengths ($L = 1.4 - 2.4$ cm), revealing the loss value of the corresponding wavelength. Similar approaches were applied for the other two chips. The linear transmission measurements were conducted in all of the three waveguides listed in Table 4.2. The propagation losses are of the orders of a few dB/cm for all the waveguides in the wavelength range of $2.0 - 2.6$ dB/cm. Generally, sample B has slight higher loss values than that of sample A as the waveguide dimensions are smaller. As can be seen from Figure 4.10, sample B has loss value of 6.1 dB/cm at 2 μm while the number for sample A is 6.0 dB/cm. As the overall loss difference is ≤ 1 dB/cm between them, only the loss results over the measured wavelength regime for sample A are plotted in Figure 4.10. The high loss value recorded near 2 μm is expected as it is close to germanium's band edge. However, beyond 2 μm the losses of sample C flatten out to a consistently low value of ~ 3 dB/cm, which indicates that these waveguides should have

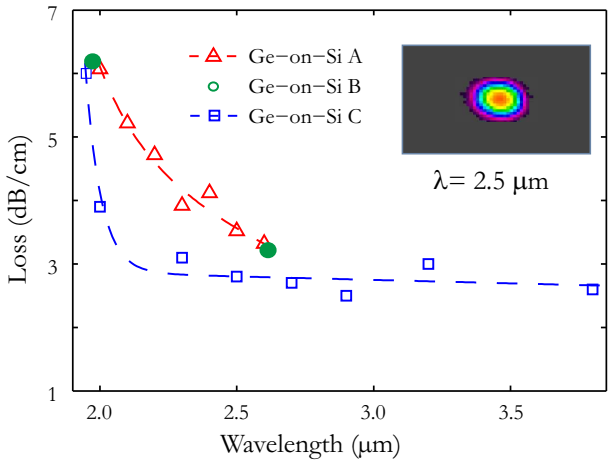

Figure 4.10: Mid-IR linear losses over the selected wavelengths for two Ge-on-Si wavguides and mid-IR guided mode from the tapered output at $\lambda = 2.7\,\mu$m, imaged by a Spiricon camera.

a broad transmission window across much of the mid-IR regime. It is worth noting that the lower losses for sample C was measured, which is attributed to the reduced of sidewall roughness by decreasing the etch depth and the reduced TD after optimising the deposition conditions.

Additional measurements were performed for longer wavelengths in sample C, firstly using an Aculight CW OPO over the range $2.6 - 3.2\,\mu$m, then a quantum cascade laser (QCL) to push out as far as $3.8\,\mu$m which was conducted by Soler-Penades. As it was not possible to use the silica coupling objective for these wavelengths, an aspheric chalcogenide lens with a focal length of 1.87 mm was used to couple light from the OPO, while a mid-IR fibre butt-coupled to the waveguide core was used to launch light from the QCL. Confirmation that the mid-IR light was predominantly guided in the fundamental mode can be seen through the high quality output profile displayed in Figure 4.10.

Compared to previous measurements of Ge-on-Si waveguides in the literature, our lowest loss of $2.5 \pm 0.2\,$dB/cm taken at $\lambda = 3.8\,\mu$m is commensurate with the losses reported for wavelengths $> 5\,\mu$m [13, 78]. This data suggests that these Ge-on-Si waveguides could provide a broad transparent window in the mid-IR regime to build various integrated photonic devices. I expect the losses are largely due to material defects at the germanium-silicon interface, the sidewall roughness scattering and bulk material absorption. As the scattering loss mechanisms are wavelength dependent, the results suggest that for the Ge-on–Si sample C the material absorption is dominant. However, further investigation is required to determine which source of scattering is dominant in these first generation Ge-on–Si waveguides. An ongoing project is currently focusing on reducing the transmission losses across the entire wavelength region by improving the waveguide quality, in terms of optimising of the design and fabrication.

4.5 Conclusion

In this chapter, the fabrication techniques for several semiconductor waveguides are introduced and the linear optical properties over the mid-IR regime are discussed. The semiconductor waveguides are fabricated both in fibre and planar form. The first one is the semiconductor core, silica cladding fibre, which can be fabricated via a HPCVD method. Generally speaking, HPCVD is a promising fabrication technique by which various materials can be deposited into silica capillaries with different material phases. The material quality can be controlled by the deposition conditions and post-processing. A number of semiconductor core fibres including silicon core fibres and germanium core fibres have been characterised to determine their linear losses at mid-IR wavelengths, revealing that their losses are lower than in the telecoms band. The advantages of the semiconductor core fibres fabricated by HPCVD is that it is easy to tune the phase of the materials and the surfaces are very smooth and also compatible with the normal silica fibre platform. The other semiconductor platform investigated in this chapter is the Ge-on-Si waveguides. The linear characterisations of the Ge-on-Si waveguides have confirmed the good optical guidance in this novel structures across the 2 - 4 μm wavelength region and it can be expected that the losses will remain low over much of the 2 - 8 μm gerion where Ge-on-Si waveguides are transparent. This could provide potential for using this waveguide platform for mid-IR applications.

Chapter 5

Nonlinear properties of silicon fibre for the mid-infrared regime

5.1 Introduction

To date, the nonlinear effects in the silicon core fibres have only been observed in fibres with hydrogenated amorphous silicon (a-Si:H) core materials. This has been made possible following continuous work to develop and optimise the high pressure chemical vapor deposition (HPCVD) technique to achieve relatively low linear losses within fibres that have micron-sized core dimensions (6 μm core size for the first observation of nonlinear propagation) [22]. In Chapter 4, the linear optical losses have been characterized in a-Si:H core fibres extensively from near infrared to the mid-infrared (mid-IR) wavelength regime, demonstrating a broad transparency window up to 2.7 μm at least. In this chapter, I extend the nonlinear characterisations across this wavelength range. The mid-IR wavelength regime offers a great advantage for the observation of nonlinear effects in silicon as it is beyond the two-photon absorption (TPA) edge. A nonlinear figure of merit ($\mathrm{FOM_{NL}}$) is used to evaluate the nonlinear performance of the fibres from the near infrared to mid-IR region. Finally, to demonstrate the usefulness of these fibres for nonlinear applications, I present the first observations of four-wave mixing (FWM) and octave-spanning mid-IR supercontinuum generation in a small core a-Si:H fibre.

5.2 Nonlinear absorption in silicon

Although silicon exhibits low linear losses at near infrared wavelengths, it begins to absorb light heavily at high input intensities because of the nonlinear absorption. TPA is the dominant nonlinear absorption mechanism in silicon at the near infrared wavelengths, though free carrier absorption (FCA) caused by the TPA process can attenuate the

optical intensity further. Both these two absorption mechanisms will be discussed in this section.

5.2.1 Two-photon absorption

The basic principles of TPA were discribed in Section 3.3.1. The coefficients (β_{TPA}) of degenerate TPA can be calculated for different wavelengths using the model derived by Garica *et al.* [103], which incorporates the forbidden-forbidden (f-f), allowed-forbidden (a-f), and allowed-allowed (a-a) optical indirect transitions. These three types of TPA depend on the parity difference in the initial and final states. β_{TPA}, which is the sum of all three transition processes can be expressed as follows [136]:

$$\beta_{\mathrm{TPA}}(\omega) = \sum_{i=0}^{2} \beta^{(i)}(\omega), \tag{5.1}$$

with the term number i for a-a, a-f, and f-f transitions. In addition,

$$\beta^{(i)}(\omega) = K_i \frac{1}{n^2 E_{ig}^3} F_2^{(i)} \left(\frac{\hbar\omega}{E_{ig}} \right), \tag{5.2}$$

where $F_2^{(i)}(x) = (2x-1)^{i+2}/(2x)^5$, K_i is a curve-fitting factor, E_{ig} is the indirect bandgap energy of silicon, $\hbar$ is the reduced Planck constant, ω is angular frequency and n is the refractive index. Figure 5.1(b) plots the theoretically predicted curve of the TPA

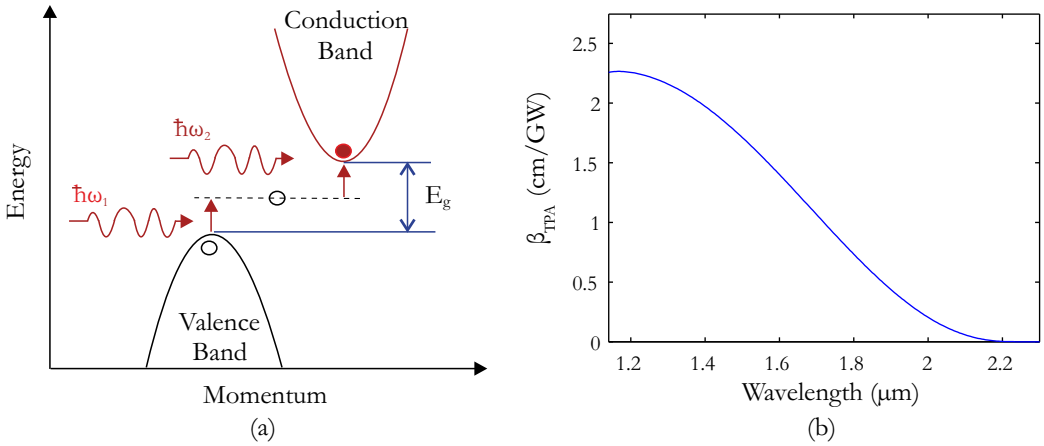

Figure 5.1: (a) Two-photon absorption process in silicon. (b) Predicted nonlinear absorption strength of TPA in silicon.

coefficient β_{TPA} as a function of wavelength in the TPA window of silicon based on the calculation from Equation 5.2. The TPA strength exhibits strong dependence on the wavelength of the incident light. From Figure 5.1(b), the TPA effect in silicon is strong in the near infrared but will weaken until the point at which it vanishes as the wavelength increases into the mid-IR regime. In crystalline silicon (c-Si), the band gap energy ($E_g = 1.12\,eV$) suggests that the TPA edge is at $2.2\,\mu m$. After this wavelength, the TPA will dramatically reduce and there will be multiphoton absorption (MPA) at longer wavelengths, though the absorption strength for these processes is much weaker. The band gap energy of a-Si (with or without hydrogen) is commonly estimated to be $E_g = 1.7\,eV$, however this depends on the deposition conditions. Furthermore the band edge will not be sharp and has an extended tail, sometimes related to the Urbach tail. Thus the practical TPA edge of our HPCVD deposited a-Si:H is not yet known and needs to be characterised.

5.2.2 Free carrier absorption

FCA is an intraband absorption and was shown in the process [iv] of Figure 3.7. Because the excited state transition in the process [iv] is small, the required input photon energy is very low. As discussed in section 3.3.2, the free-carrier induced absorption in silicon follows $\Delta\alpha \propto \lambda^2$ from the near infrared to the mid-IR regime. The FCA coefficient has been studied thoroughly in c-Si at telecom wavelength and extended to the mid-IR wavelength up to $14\,\mu m$ [137]. The a-Si:H material has been demonstrated to have an enhanced FCA coefficient [23], due to two-state absorption (TSA), where mid-gap localized defect states can aid absorption as modelled in Ref. [138]. The FCA coefficient $\sigma_{\text{FCA}} \sim 1.6 \times 10^{-16}\,cm^2$ at $1.55\,\mu m$ can be calculated from the Equation 3.31 using the parameters for a-Si:H listed in Ref. [139]. It is possible to account for the wavelength dependence of this parameter using a simple approximation presented in Ref [137].

5.2.3 Free carrier lifetime

As previously mentioned, the free carrier lifetime is a crucial parameter for high power, high speed devices such as modulators. The pump-probe technique has been widely used to measure the carrier lifetime whereby the carriers are optically excited by the pump light and monitored by a secondary probe. The output optical power of the probe exhibits an exponential decrease as a function of time related to the lifetime given in the form:

$$P_{\text{out}} = P_{\text{in}} \exp\left(-\frac{t}{\tau}\right), \tag{5.3}$$

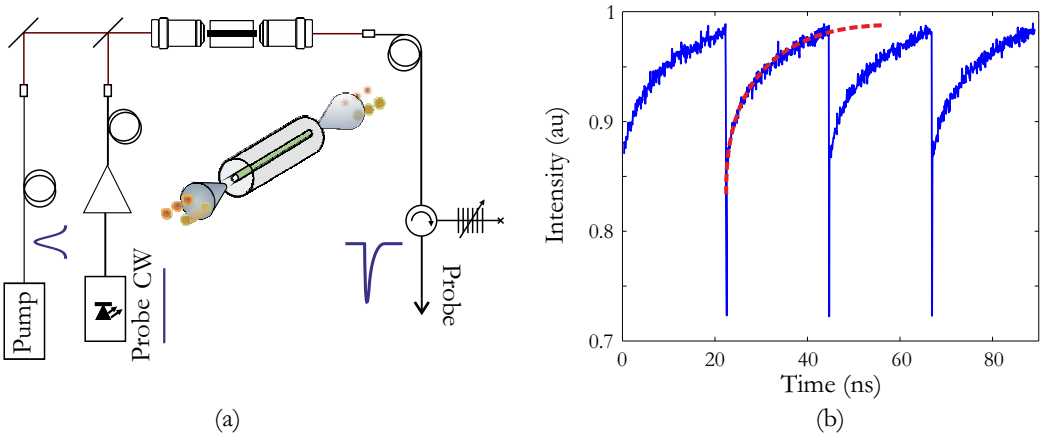

Figure 5.2: Pump-probe experiment employed by Mehta [141].

where τ is the carrier lifetime. The carrier lifetime of the material can be determined by fitting the pump probe measurement results using the Equation 5.3.

The carrier lifetime in the silicon optical fibres was first measured by Won *et al.* in 2007 and then by Mehta *et al.* in 2011 [140, 141]. The main difference between the two experiments is the way in which the carriers are generated. Won *et al.* used the single photon excitation process to generate the carriers while Mehta *et al.* used TPA. Hence, Mehta used a high power pump in a co-propagation scheme instead of side pumping with below bandgap light. The experimental setup used for Mehta's measurements is shown in Figure 5.2. The fibres primarily investigated in this thesis were characterised using a similar TPA-based approach, hence the lifetime measurement demonstrated by Mehta will be briefly introduced.

The pump wavelength was chosen in the wavelength regime $1.1\,\mu\text{m} < \lambda < 2.2\,\mu\text{m}$, where the photon energy is below the band gap of silicon but within the two-photon window to efficiently excite the free-carriers through TPA. A high peak power mode-locked fibre laser operating at the telecommunications wavelength of $1.54\,\mu$m, with a pulse duration of 720 fs and a 40 MHz repetition rate was employed as the pump source. A CW laser diode provided the low power probe at $1.57\,\mu$m. A preamplifier was used for the CW probe to provide enough power to overcome the transmission losses of the a-Si:H fibre and other external factors such as coupling losses and Fresnel reflections. The pump and probe beams were then combined with a pellicle beam-splitter before coupling into the silicon fibre using a microscope objective. As a result, the output from the fibre contains both the pump and probe waves. The probe wavelength is filtered by using a conventional Bragg grating and circulator configuration. The grating consists of a reflection peak at $1.57\,\mu$m with a FWHM of approximately 1.5 nm. This bandwidth was chosen such that the increased spectral width due to amplitude modulation of the CW is able to be reflected without any form of pulse broadening or filtering. The filtered signal was detected and viewed on a 30 GHz sampling oscilloscope. Figure 5.2(b) shows the free-carrier modulated probe amplitude for a coupled signal power. By applying

Table 5.1: Typical carrier lifetime of a-Si:H fibres.

a-Si:H fibre	Carrier lifetime (ns)	Core diameter (μm)
A	86	6
B	4	1.7

an exponential fit to the recovery (red dashed lines), the free-carrier lifetime τ can be determined.

For this work, two a-Si:H core fibres with different core sizes were characterised and the corresponding carrier lifetimes are given in Table 5.1. From this data it can be seen that the carrier lifetime depends on the physical dimensions of the semiconductor fibre core. The surfaces of all materials, regardless of their physical form, always exhibit the highest number of defects. Since the deposited semiconductor material in these fibres will assume the same surface conditions as the inner walls of the silica capillary, the surface of the semiconductor will produce defected sites in order to form a perfect adhesion (since there is a material mismatch between silica and silicon). By decreasing the core diameter, the surface to volume ratio is increased and free carriers are generated closer to a recombination site (i.e. surface).

5.2.4 Characterization of the nonlinear absorption

Characterization of the nonlinear absorption in the a-Si:H core fibres was performed using well-established high power transmission experiments [132]. In the measurements, the transmitted power is measured for a set of input powers and the transmission data is fitted by the theoretical simulations which model the pulse propagation. The generalized nonlinear Schrödinger equation (NLSE) that describe the propagation of optical pulses in silicon core fibres, already presented in Section 3.4. For a typical centimetre long silicon core fibre ($L \sim 1\,\mathrm{cm}$), at $1.55\,\mu\mathrm{m}$, the GVD (β_2) is estimated to be approximately $1\,\mathrm{ps}^2/\mathrm{m}$. The dispersion length L_D defined in Section 3.4.1 is around 16.7 cm for a 720 fs (FWHM) pulse which is much longer than the actual fibre length. Hence, it is therefore possible to neglect the effects of dispersion during the propagation. The primary concern is the evolution of the pulse intensity due to the nonlinear absorption, it is possible to simplify the generalized NLSE by ignoring the spectral evolution to concentrate on the evolution of the temporal profile. By substituting $\gamma = k_0 n_2/A_{\mathrm{eff}} + i\beta_{\mathrm{TPA}}/2A_{\mathrm{eff}}$ and the pulse intensity $I(z,t) = |A(z,t)|^2/A_{\mathrm{eff}}$ in Equation 3.57, the simplified model under the influence of linear and nonlinear loss is given by the coupled rate equations:

$$\frac{dI(z,t)}{dz} = -\alpha_l I(z,t) - \beta_{\mathrm{TPA}} I^2(z,t) - \sigma N_c(z,t) I(z,t), \tag{5.4}$$

$$\frac{\partial N_c(z,t)}{\partial t} = \frac{\beta_{\mathrm{TPA}}}{2h\nu_0}|I(z,t)|^2 - \frac{N_c(z,t)}{\tau_c}. \tag{5.5}$$

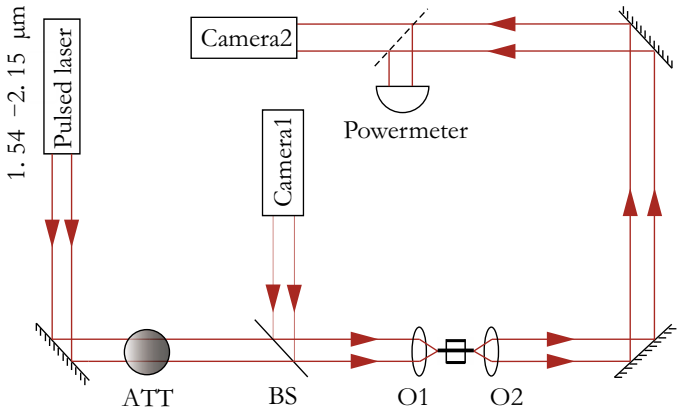

Figure 5.3: Experimental setup for nonlinear absorption characterisation.

In this section, the experimentally measured nonlinear absorption coefficients of several silicon optical fibres are estimated by solving the Equations 5.4 and 5.5 using the TPA and FCA coefficients as free parameters. By fitting the data, the best coefficients can be found corresponding to a particular fibre. The a-Si:H core fibres were first characterised using an erbium doped mode-locked fibre laser (Onefive ORIGAMI) to evaluate the nonlinear properties at a telecom wavelength. In the experiments, a high peak power pulsed source is launched into the a-Si:H core fibre and the corresponding output powers are recorded as a function of increasing input pump power. The maximum input power should be high enough to access the nonlinear transmission region induced by the TPA.

The experimental setup is illustrated in Figure 5.3 with the output measured on the power meter. The fibre laser was first used to generate standard hyperbolic secant pulses with a duration of 720 fs (FWHM) and a repetition rate of 40 MHz at 1.54 μm. The light was launched into the fibre core using the same free space coupling configuration in Section 4.4.3.1 and focused it onto a calibrated Newport germanium photodetector (Model 818-IR). Similar with the linear characterisation setup, two near-infrared cameras were used in this experiment to image the back-reflection from the input a-Si:H core fibre facet and the output end face of the fibre, which helps optimize the light coupling. A conventional graded neutral density silica attenuator was used to control the input power. The input power was kept very low ($\sim \mu$Ws) at first and then increased gradually until the output power saturated due to the TPA.

Two 6 μm core fibre samples were investigated. a-Si:H core Fibre L listed in Table 4.1 has a length of 1.5 cm and its transmission loss was measured to be $\sim$ 6.77 dB/cm at 1.54 μm. While Fibre D from the same table has a lower transmission loss of $\sim$ 2.1 dB/cm at 1.54 μm. These two silicon core fibres were chosen for the nonlinear characterisations because they had different loss values (one relatively high loss and the other with lower loss) and exhibited clean spectral broadening characteristics which will be discussed in Section 5.3. Figure 5.4 shows the normalized output power as a function of coupled input

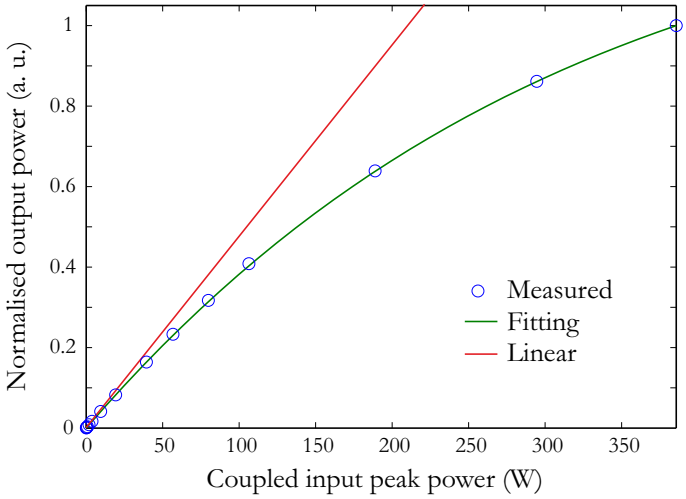

Figure 5.4: Normalized output power as a function of coupled input peak power showing the onset of nonlinear absorption.

peak power measured for the a-Si:H core fibre sample L. The red line indicates the linear transmission loss. The green curve is a numerical fit to the nonlinear transmission data. The fitting reveals the best fit values of $\beta_{\mathrm{TPA}} \sim 0.75\,\mathrm{cm/GW}$ and $\sigma_{\mathrm{FCA}} \sim 1 \times 10^{-16}\,\mathrm{cm}^2$. Measurements of Fibre D yield a $\beta_{\mathrm{TPA}} \sim 0.70\,\mathrm{cm/GW}$ and $\sigma_{\mathrm{FCA}} \sim 1 \times 10^{-16}\,\mathrm{cm}^2$ which suggests our fabrication method could produce a-Si:H material with consistent good quality.

The value found for the TPA parameter is similar to those reported for a-Si:H materials on-chip [23, 142], with typical results varying from $0.08 - 4.1\,\mathrm{cm/GW}$. It can be expected this variation is due to the differences in the material quality as these waveguides were fabricated using a different processes [143]. Furthermore, the bandgap energy scales with the binding energy, which could be influenced by the concentration of hydrogen in the amorphous silicon (a-Si). Hence, the incorporation of hydrogen could cause differences in the bandgap energy, thus resulting in variations on the TPA coefficient. The value found for σ_{FCA} is also in good agreement with our previous calculation from the Drude model in Section 5.2.2.

As a-Si has been reported to have a larger bandgap energy ($E_g \sim 1.7\,\mathrm{eV}$) compared to c-Si, the TPA edge should occur at shorter wavelengths at $\sim 1.46\,\mu\mathrm{m}$. Hence the nonlinear absorption is expected to be modest at the telecom wavelength ($\sim 1.54\,\mu\mathrm{m}$) used in this experiment because it should be past the TPA edge. However, in practice the values of the TPA coefficient β_{TPA} measured around $1.5\,\mu\mathrm{m}$ vary quite substantially and are not insignificant. This can be attributed to the amorphous nature of the material which cause the band tail to be elongated, and hence results in a smearing of the TPA edge. In addition, when compared to c-Si, the measured TPA coefficient is in the upper range reported related to the larger $\chi^{(3)}$ nonlinearity ($0.5 - 0.9\,\mathrm{cm/GW}$) [56, 144]. It is for this

reason that a-Si:H has recently been proposed as a strong candidate for potential TPA-based applications including optical limiting, pulse shaping and all-optical modulation [145].

5.2.5 Nonlinear absorption across the TPA edge

As the precise position of the TPA edge is not known for a-Si:H, the dispersion of the TPA parameter was investigated for a range of wavelengths spanning half the theoretical bandgap energy of a-Si ($E_g/2 \sim 0.85\,\text{eV}$) and up to the edge of the mid-IR region $\sim 2.15\,\mu\text{m}$. To access sufficiently high powers, for these measurements I employed the femtosecond OPO (Radiantis OPIUM). The Ti: sapphire laser pumped OPO generates hyperbolic secant pulses with a duration of 250 fs (FWHM) and a repetition rate of 80 MHz at selected wavelengths. Furthermore, to minimize the effects of dispersion for the short pulses used in these experiments, I employed a shorter piece of fibre (Fibre D1 $L = 0.47\,\text{cm}$) that was cut off from Fibre D during the characterization of the linear losses. The fibre length was considerably shorter than the dispersion length for all wavelengths (e.g. $L_\text{D} \sim 1.44\,\text{cm}$ at $1.54\,\mu\text{m}$ for the femtosecond pulses), thus the simplified coupled Equations 5.4 and 5.5 are still valid for the OPO. To begin, the a-Si:H core fibre was tested using the OPO at $1.54\,\mu\text{m}$, the same wavelength as the telecoms fibre laser. In both cases, the same value of β_TPA was obtained, validating the use of the short pulse OPO for further measurements.

For each wavelength, the output power was recorded as a function of coupled input peak power and the results are plotted in Figure 5.5. For all the wavelengths, there is a linear dependence for low input peak powers $< 50\,\text{W}$. However, at higher input powers, the output powers for the short wavelengths (i.e., $1.55\,\mu\text{m}$ and $1.65\,\mu\text{m}$) begin to saturate due to nonlinear absorption. In contrast, the largely linear trend exhibited for the longer wavelengths indicates that TPA is essentially negligible in this regime. As a result, this data can be used to get an indication of the TPA edge of our core material, which is likely to be in the region of $1.7\,\mu\text{m}$, or $E_g \sim 1.4 - 1.5\,\text{eV}$. It is worth noting that a similarly low value of the bandgap energy of a-Si:H has been measured via ellipsometry in Ref. [142], and could be attributed to a change in material density due to the hydrogen content.

The same fitting method as used in Figure 5.4 was applied to the different wavelengths to establish the values of β_TPA. In this analysis I use $\tau_c \sim 86\,\text{ns}$, as determined via pump-probe measurements [141], $A_\text{eff} = 13\,\mu\text{m}^2$, which has been estimated from modal analysis and shown to be approximately constant over the entire wavelength range [132], and $\sigma(\lambda)$, as calculated via the Drude model using the parameters for a-Si:H material in [23]. The corresponding values obtained for the TPA coefficient β_TPA are plotted as a function of wavelength in Figure 5.6. These results show that the β_TPA initially drops sharply from 0.70 cm/GW down to 0.28 cm/GW as the wavelength increases through the

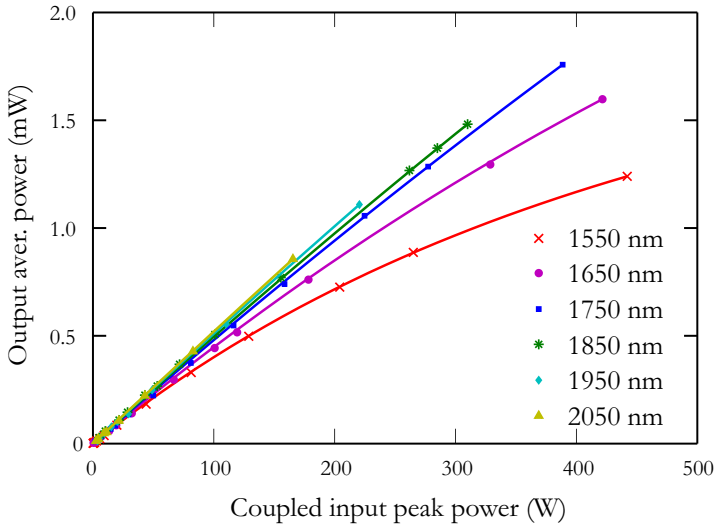

Figure 5.5: Nonlinear absorption measurements for the wavelengths given in the legend. The solid curves are the simulated fits obtained via solving Equations 5.4 and 5.5 for the corresponding wavelength.

telecom window ($1.55 - 1.65\,\mu$m), then eventually begins to plateau at a negligible value of 0.05 cm/GW as the wavelength approaches the mid-IR regime ($1.95 - 2.15\,\mu$m). This trend of decreasing β_{TPA} is as what would be expected for wavelengths near the TPA edge, and specifically, I would also expect this to drop to zero for photon energies smaller than $E_g/2$, where the sum of the energies of two photons is no longer sufficient to span the bandgap. Here I attribute the non-zero values of β_{TPA} at the longer wavelengths, beyond the estimated TPA edge, to the exponential Urbach tail [146], so that some TPA exists below the half bandgap [147]. However, the fact that the TPA edge appears to be shifted from that of a-Si suggests that the position of the TPA edge may be tuned through the material deposition parameters, and this is currently the subject of further investigations.

These measurements represent the first detailed nonlinear characterisations performed on the a-Si:H optical fibres in the mid-IR regime and extend the understanding of the nonlinear properties of this material into the longer wavelength region, which could help establish new applications. Also, the TPA and FCA coefficients can be used for the investigations of the nonlinear refraction in the following sections as they provide additional details of parameters for the generalised NLSE.

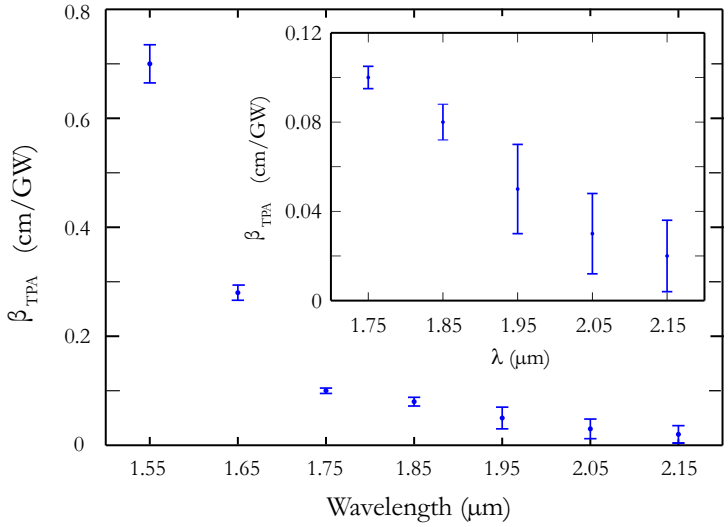

Figure 5.6: TPA parameter as a function of wavelength. Inset: close up of the low value β_{TPA} region. Error bars represent the uncertainty in the input powers.

5.3 Nonlinear refraction in silicon fibres

5.3.1 Self-phase modulation

As discussed in Section 3.3.3.1, self-phase modulation (SPM) will broaden the spectrum as the new components are generated continuously as the pulse propagates through the a-Si:H core fibre. In order to observe SPM induced spectral broadening, the a-Si:H core fibre should have a low optical loss and high nonlinearity as the length of the fibres is typically of the order of a centimetre. The effective length of the fibre (L_{eff}) should be longer than the nonlinear length which is defined by $L_{\mathrm{NL}} = 1/\gamma P_0$ in Section 3.4.1. The nonlinear length L_{NL} is $\sim 0.57\,\mathrm{mm}$ for a $6\,\mu\mathrm{m}$ core fibre at $1.54\,\mu\mathrm{m}$ when the input peak power is 300 W. For a a-Si:H core fibre with a typical loss value of 3 dB/cm, the effective length L_{eff} is around 0.787 cm which is longer than the nonlinear length. This suggests that the nonlinear effects should be observable in our a-Si:H core fibres. To date, SPM has been observed in many silicon waveguides [148], as have many other nonlinear processes such as supercontinuum generation [81] and cross phase modulation (XPM) based wavelength conversion [149, 28]. The first observation of SPM in a micron-sized silicon core fibre was demonstrated by our group in 2010 [132]. Based on this observation, a spectral fitting method was developed to give an evaluation of the nonlinear coefficient n_2.

5.3.2 Nonlinear refraction index characterisation

There are a few measurement techniques that can be used to determine the nonlinear refractive index n_2. For bulk materials, the Z-scan technique is the most commonly

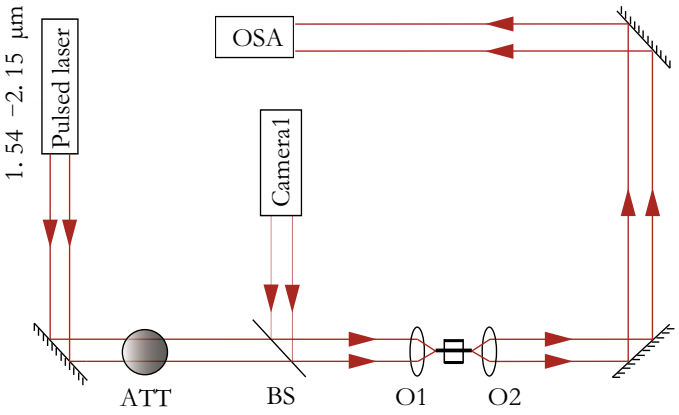

Figure 5.7: Experimental setup for nonlinear refraction characterisation.

used method [55]. For fibres, the methods are usually based on monitoring different nonlinear processes such as FWM [150], modulation instability (MI) [151], XPM [152], and SPM [153]. In our group, the nonlinear refractive index is usually measured via the widely used SPM method because of its simplicity for characterising n_2 in the normal dispersion regime. Thus, compared with other approaches, it does not require phase-matching. For the silicon fibres, a full generalized NLSE shown in Chapter 3 including all the quantities of linear loss, dispersion, nonlinear strength and carrier effects needs to be considered to obtain a fit to the measured spectral broadening, with n_2 as the free parameter. The other parameters of the fibres including linear loss, TPA coefficients β_{TPA} and FCA coefficients σ_{FCA} are as predetermined.

The experimental setup for the spectral measurement is shown in Figure 5.3, where the output is monitored on the optical spectrum analyser (OSA). The OSA is set to have the same resolution of 0.1 nm and sensitivity of −70 dBm for each measurement. Similar with the nonlinear absorption measurement illustrated in Section 5.3, the a-Si:H core fibre was first tested using the telecom wavelength fibre laser source (Onefive ORIGAMI) as used for the characterisation of the silicon core fibres. The light was coupled into the silicon core fibre and carefully optimized by monitoring the output beam profile on the second CCD camera to make sure the fundamental mode was preferentially excited.

Three particular a-Si:H core fibres (Fibre C, D and M of Table 4.1) were investigated. Two of which have 6 μm core diameters and the third one has a 1.7 μm core diameter. As all three fibres show similar spectral broadening due to the SPM, here only the spectral evolution of Fibre D is shown in Figure 5.8. The experimental spectra are plotted in green and the labeled powers in each plot correspond to the coupled input peak power. As shown by the green curves in Figure 5.8, the fibre's output spectrum exhibits considerable broadening due to SPM. The spectral broadening grows larger and larger with increasing input power. From the spectra, the maximum phase shift ϕ_{max} is

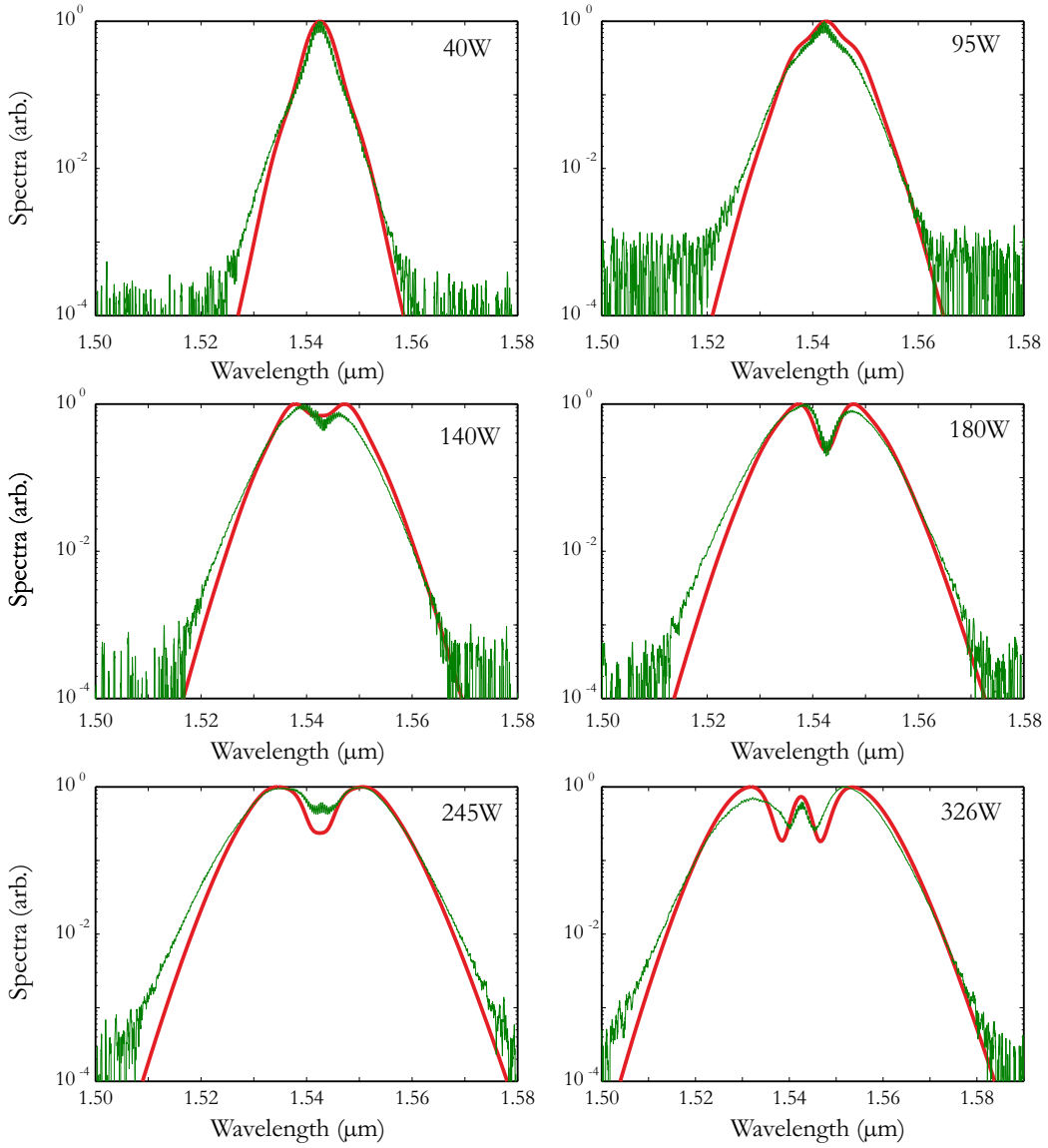

Figure 5.8: Experimental spectral evolution as a function of input peak power (green line). The red curves are numerical fits to full generalized NLSE Equations 3.57 and 3.34.

approximated through the number of peaks M by [88]:

$$\phi_{\max} \approx \left(M - \frac{1}{2}\right) \tag{5.6}$$

revealing $\phi_{\max} \approx 2.5\pi$ for the last spectrum in Figure 5.8.

The input pulse properties used in the generalized NLSE simulations were from the specifications of the laser source. The linear loss of Fibre D is 2.1 dB/cm at 1.54 μm. The nonlinear parameters were $\beta_{\text{TPA}} \sim 0.70\,\text{cm/GW}$ and $\sigma_{\text{FCA}} \sim 1 \times 10^{-16}\,\text{cm}^2$ and β_2 was estimated using FEM modelling to be $0.98\,\text{ps}^2/\text{m}$ at 1.54 μm. The blue curves which are numerically fitted using a Kerr coefficient of $n_2 = 1.7 \pm 0.05 \times 10^{-13}\,\text{cm}^2/\text{W}$ show a

good quantitative agreement with the normalised measured spectral curves. Due to the slight uncertainty in the coupling efficiency, an additional fine tuning of each input peak power was required to obtain a better fit. Thus the uncertainty in the measurements was based on this variation.

A summary of the measured Kerr nonlinearities of these a-Si:H core fibres is shown in Table 5.2. These values of the nonlinear Kerr coefficient are consistent with our previous measurements [132]. As Fibre C has slightly lower loss than Fibre D, it is interesting to see that the Kerr coefficient n_2 is larger than Fibre D. Although the relation between the linear loss and the Kerr coefficient n_2 in silicon core fibre is not straightforward, it can be found that the linear and nonlinear optical properties of the silicon core fibre could be improved by further keeping on optimising the deposition conditions to obtain better quality materials (e.g. increase the hydrogen content in the fibre core). Significantly, the Kerr coefficient n_2 found for a-Si:H material is two times larger than that of c-Si [154, 155], which is promising for the use of a-Si:H for nonlinear applications.

In silica optical fibres, SPM-induced spectral broadening of short pulses is normally symmetric around the centre. However, in the semiconductor fibres the main effect that can cause spectral asymmetry is the FCA when the input peak power is high [132]. The small oscillations on the experimentally recorded spectra are most likely due to multimode interference (MMI) from other higher order modes excited modes at the launch in the silicon fibre. Although the silicon core fibre is highly multimoded due to the large refractive index contrast between the silicon core and the silica cladding in the wavelength regime considered in this thesis, by carefully optimising the free space coupling into silicon core fibres, most of the light ($> 95\%$) can be launched into the fundamental mode. It has been confirmed that the effects of multiple modes in this case do not severely affect the estimation of n_2 using the single-mode generalized NLSE, but simply adds spectral modulations on the SPM envelope [156].

Following this effort, the characterization of the nonlinear refractive index n_2 for the a-Si:H core fibres was extended beyond the telecommunications window up to the mid-IR regime. Importantly, this will help develop a full understanding of the nonlinear

Table 5.2: Kerr coefficients for several a-Si:H core fibres characterised at $\lambda = 1.54\,\mu$m using numerical fitting of the experimental SPM spectra.

a-Si:H fibre	Core diameter (μm)	α_l (dB/cm)	β_{TPA} (cm/GW)	σ_{FCA} (cm^2)	n_2 (m^2/W)
C	6	1.98	0.75	1×10^{-16}	1.75×10^{-13}
D	6	2.1	0.70	1×10^{-16}	1.70×10^{-13}
M	1.7	2.8	0.70	1×10^{-16}	1.70×10^{-13}

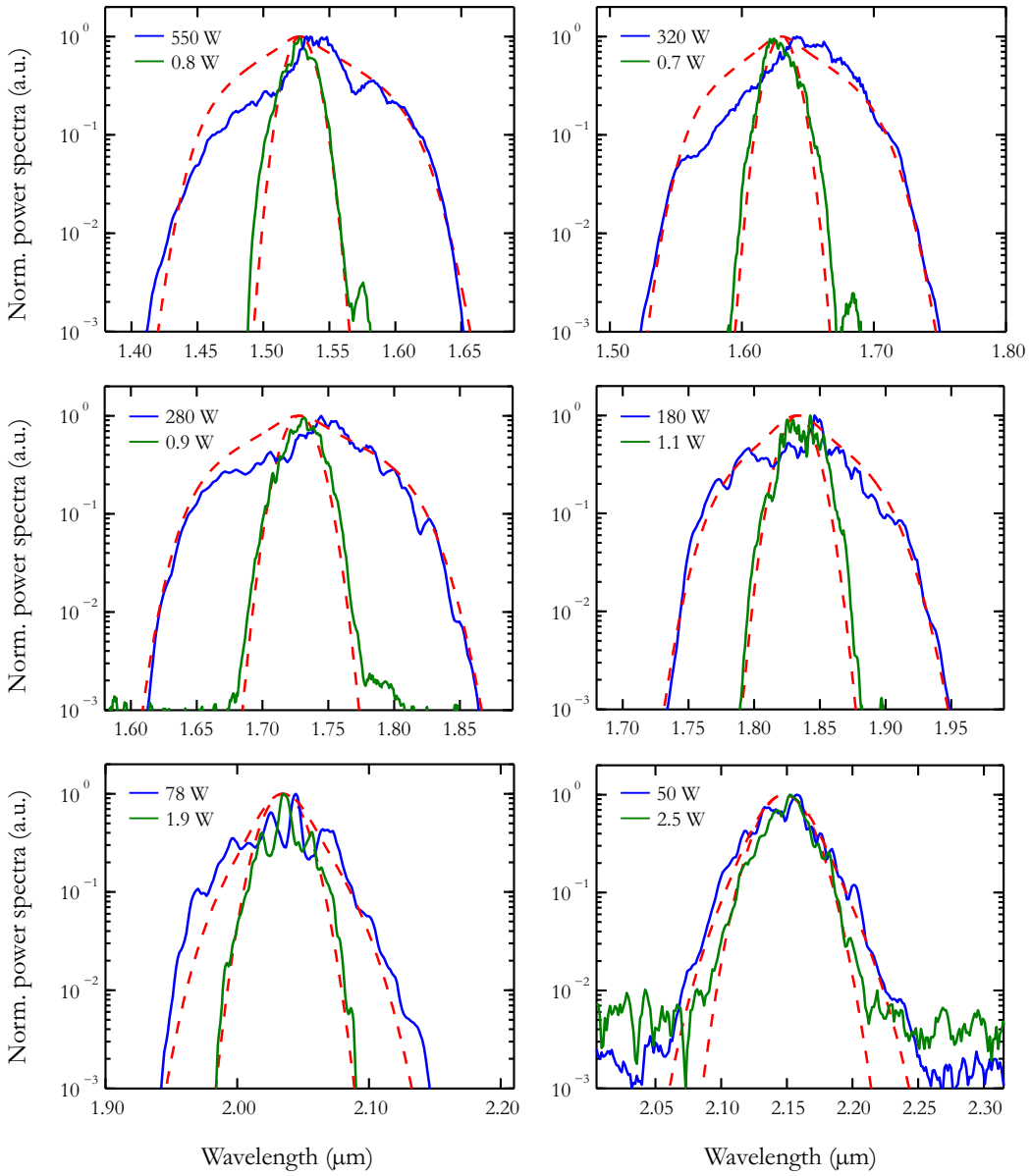

Figure 5.9: Experimental power-dependent transmission spectra as a function of pump center wavelength, as labeled in the legends. The dashed lines are numerical fits obtained by solving Equations 3.57 and 3.34.

properties of the a-Si:H core fibre, and specifically to fill in the spectral gap between the telecom wavelength and the mid-IR region where the TPA edge is located. Previous measurements of these quantities across this wavelength region have only been performed in the bulk c-Si material [55, 136, 157]. As a-Si:H is emerging as a useful material for nonlinear applications, a comprehensive study of the nonlinear refractive index will be important for future work, particularly in the mid-IR region.

A series of experiments were carried out on a-Si:H core fibre D to study the spectral broadening induced by SPM and determine the values of n_2 from 1.45 μm to 2.15 μm. For these experiments, the same femtosecond OPO (Radiantis OPIUM) used in the

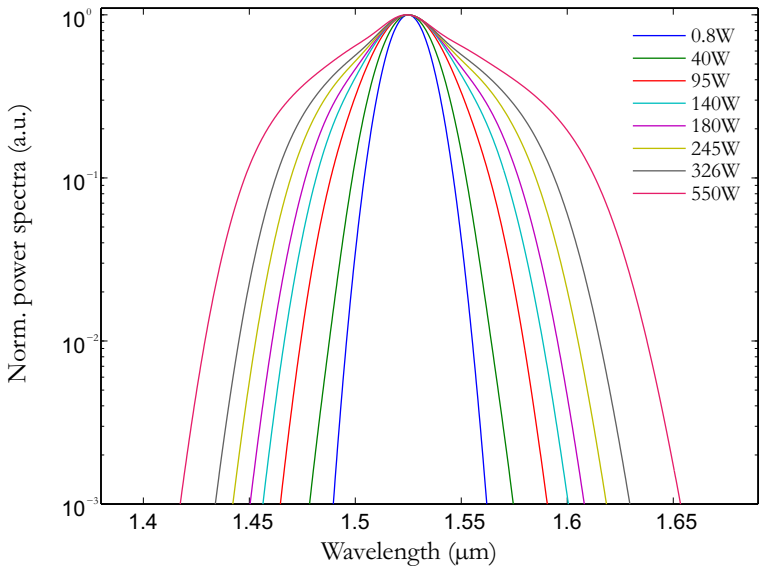

Figure 5.10: For the chirped pulses of 250 fs and selected input powers from Figure 5.8 and Figure 5.9, the figure shows the spectrum broadening from simulation.

nonlinear absorption characterisations in Section 5.2.4 was employed as the input source to provide high peak power pulses at these wavelengths. The setup was the same as that used for 1.54 μm, but this time the output spectra were monitored via a long wavelength OSA (Yokogawa AQ6375) covering $1.2 - 2.4\,\mu$m. The measured SPM spectra are shown in Figure 5.9 over a selected input wavelength range of $1.45 - 2.15\,\mu$m. For each central wavelength, the output transmission spectra are recorded at two input peak powers, as designated in the legends.

Unlike the pulses generated from the telecom fibre laser, the optical pulses from the OPO are not transform-limited and hence there is an initial frequency chirp on the pulses. Here, the results obtained with low input powers are essentially free from nonlinear propagation and are included as an indicator of the bandwidth of the input pulse, and thus as a means to determine the size of the initial negative frequency chirp on our pulses. The chirp was not found to vary dramatically over this wavelength range, and had a value of $C \sim -0.9$ at 1.55 μm. This was determined from a comparison between the measured autocorrelation trace and a fit to the input spectrum which had a FWHM bandwidth of $\Delta\lambda \sim 23$ nm.

Figure 5.10 plots the simulation results of spectral broadening assuming a 1.55 μm pump pulse from the OPO, but for the same input powers as those in Figure 5.8, obtained with the fibre laser as the input. As it can be seen, the SPM induced modulation for the two pump pulses is quite different, and the modulation induced by the nonlinear phase shift has vanished in Figure 5.10. This is due to the initial chirp on the OPO pulses, which is partly cancelled by the SPM-induced chirp [88]. Further investigations of the role the chirp plays on the spectral broadening is required to fully understand the

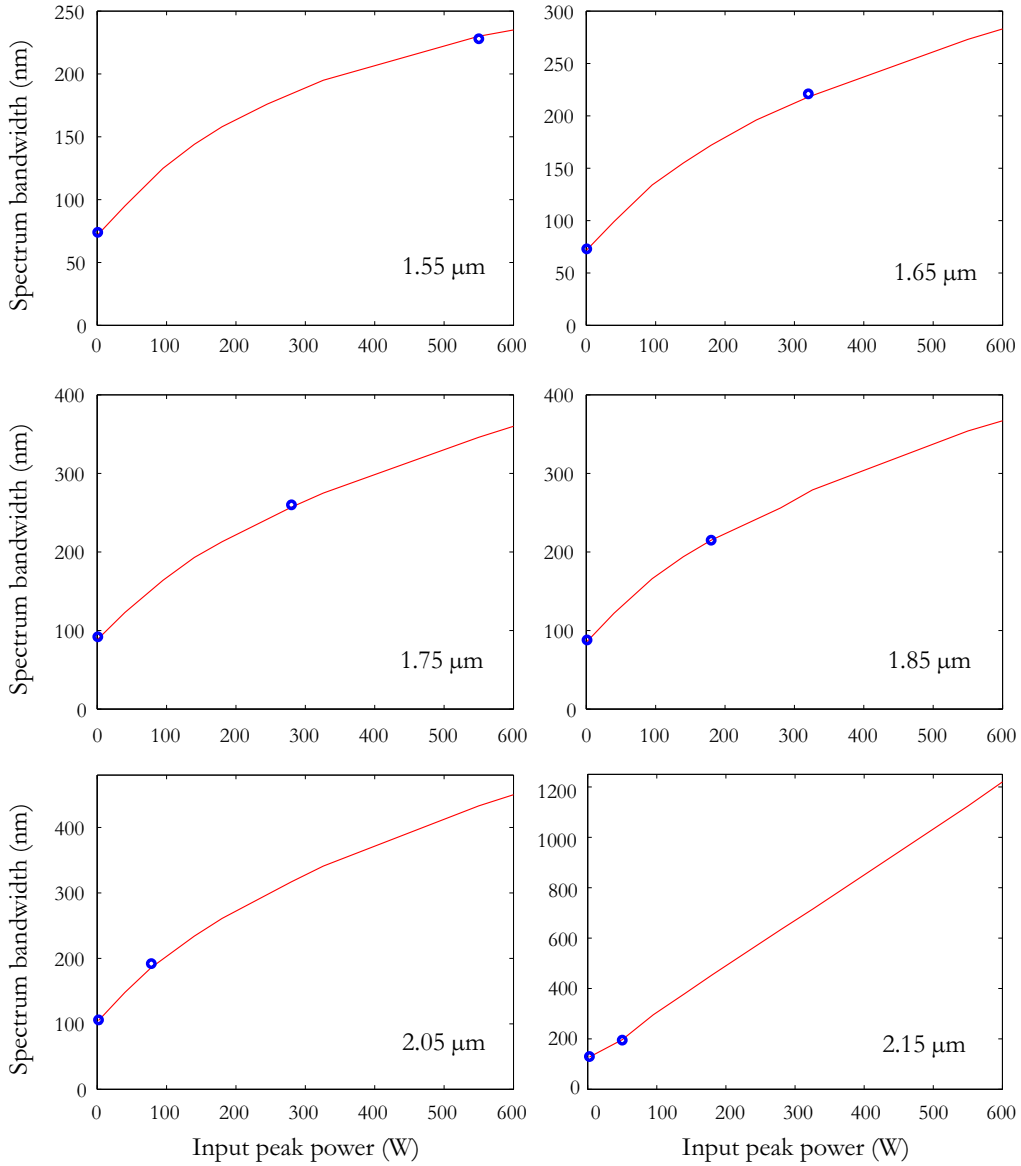

Figure 5.11: Simulated spectral bandwidth (−30 dB/cm) for selected input peak powers for different pump center wavelength, as labeled in the legends. The blue dots are experimental measured spectral bandwidth from Figure 5.9.

evolution, which is another ongoing area of research. Moreover, because of the shorter input pulse from the OPO, the obtained spectrum bandwidths (at the −30 dB) are larger in Figure 5.10, than in Figure 5.8. For example, the bandwidth for the input power of 326 W is around 200 nm in Figure 5.10 which is three times larger than that the 70 nm in Figure 5.8.

Returning to the wavelength dependant spectrum broadening, the high power results are then used to illustrate the strong spectral broadening due to the large Kerr nonlinearity of the a-Si:H core material, with bandwidths of more than 200 nm obtained for all wavelengths below 2.05 μm. The limited spectral broadening seen for wavelengths above

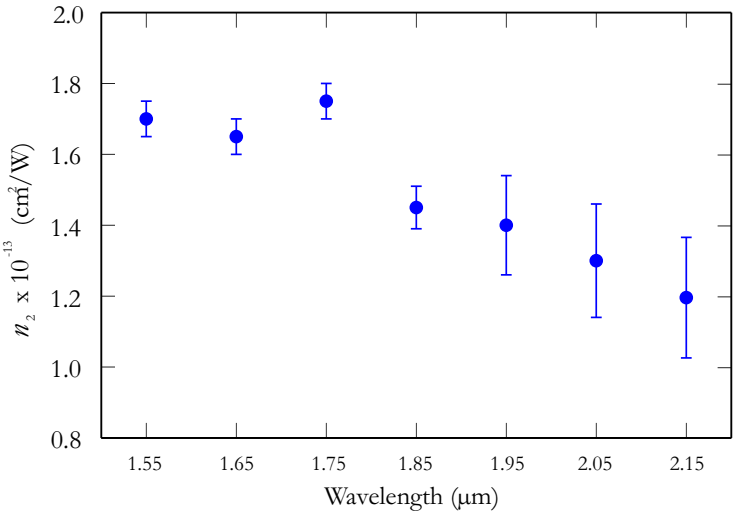

Figure 5.12: Wavelength dependence of the Kerr nonlinear coefficient n_2. Error bars represent the uncertainty in the input powers.

2 μm is due to the increased coupling losses (from 0.6 dB at 1.55 μm up to 3.8 dB at 2.1 μm) and the lack of output power as the pump wavelengths move towards the edge of the tuning range of the OPO. Figure 5.11 plots the spectral broadening as a function of input peak power for pump wavelength listed in Figure 5.9. As can be seen from the figure, the spectral broadening increases monotonically with increasing input peak. These simulation results suggest that for the longer wavelengths, much more spectral broadening would be observed if the input powers were larger. In the experiment, the coupled input peak power for a pump wavelength of 2.15 μm is only one tenth of that at 1.55 μm. Larger bandwidths (more than 1200 nm) at the mid-IR wavelength are expected to be seen with 'hundreds of Watts' coupled input peak powers in the a-Si:H as both the linear and nonlinear loss decrease with increasing wavelength.

The size of the Kerr coefficient for each central wavelength can then be established by fitting the spectral broadening using the same method as conducted for the telecom wavelength. The corresponding values of n_2 are plotted in Figure 5.12, which shows that as the input pulse wavelength is shifted across the TPA edge, the n_2 value first increases slightly up to a value of 1.75×10^{-13} cm^2/W at 1.75 μm, then drops to a modest value of 1.2×10^{-13} cm^2/W at 2.15 μm. This trend is as expected from the nonlinear Kramers-Krönig relation, where the values of n_2 are expected to peak around the TPA edge, as similarly observed in c-Si around 2.2 μm ($E_g/2 \sim 0.56$ eV) [136]. It is worth noting that the larger error bars for longer wavelengths are due to the smaller broadening factors associated with the lack of available coupled power at these wavelengths.

5.4 Figure of merit

As discussed in Sections 5.2 and 5.3, with two of the most important nonlinear parameters being measured from the near infrared to the mid-IR region, it is useful to define a FOM to evaluate the overall nonlinear performance of the a-Si:H material. As the main nonlinear absorption for the wavelength region investigated in this thesis is TPA, a $\mathrm{FOM_{NL}}$ was defined as a normalised ratio of n_2 to β_{TPA}. By using this nonlinear figure of merit, it provides a dimensionless measurement to compare different nonlinear platforms. In this thesis, the same definition was use as in [80, 158, 159]:

$$\mathrm{FOM_{NL}} = \frac{\mathrm{n_2}}{\lambda_{\mathrm{o}}\beta_{\mathrm{TPA}}}. \tag{5.7}$$

This FOM was initially defined to provide a useful dimensionless measurement of the suitability of the material for optical switching at different wavelengths [154]. The nonlinear phase shift can be obtained by substituting n_2 with the $\mathrm{FOM_{NL}}$ to Equation 3.37:

$$\phi_{\mathrm{NL}}(t) = 2\pi\mathrm{FOM_{NL}I(t)}\beta_{\mathrm{TPA}}\mathrm{z}. \tag{5.8}$$

Assuming there is sufficient intensity or interaction length to induce a nonlinear phase shift, then the limiting case of Equation 5.8 can be applied to produce the maximum induced nonlinear phase of:

$$\phi_{\mathrm{NL}}(t) = 2\pi\mathrm{FOM_{NL}}. \tag{5.9}$$

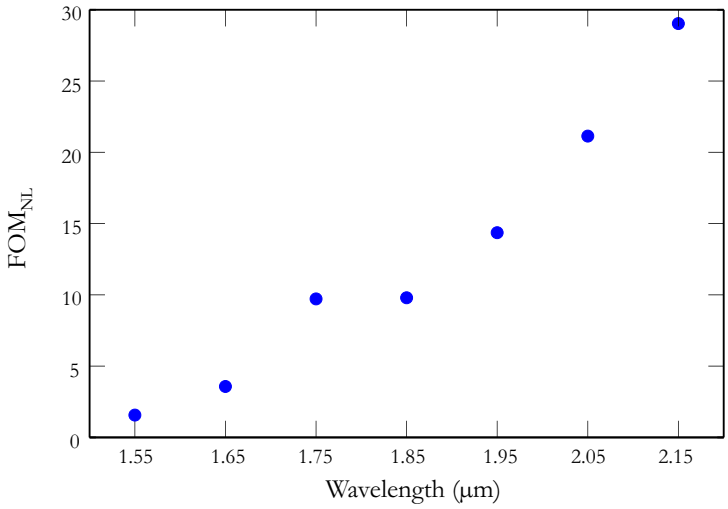

Figure 5.13: Wavelength dispersion of the $\mathrm{FOM_{NL}}$.

Values of $\mathrm{FOM_{NL}} > 2$ are necessary for applications requiring a minimum nonlinear induced phase shift of 4π or higher. These applications involve processes such as XPM to create nonlinear directional couplers. Values where $0.5 < FOM_{\mathrm{NL}} < 2$ are suitable for applications only requiring a π phase shift, such as Mach-Zehnder interferometers.

With the wavelength dependent values of both β_{TPA} and n_2 established from the previous characterisations, the dispersion of the $\mathrm{FOM_{NL}}$ in our a-Si:H fibre material, is in Figure 5.13. This figure clearly shows that despite the decrease in n_2 at the longer wavelengths, the dramatic reduction in β_{TPA} results in a monotonic increase in the $\mathrm{FOM_{NL}}$. Thus, although the value of the $\mathrm{FOM_{NL}}$ at $1.55\,\mu$m for this a-Si:H core material is comparable to what has been reported in other a-Si:H waveguides at telecom wavelength, it increases rapidly to ~ 10 for the peak value of n_2 at $1.75\,\mu$m, then even further up to ~ 28 at the longest wavelengths, this is consistent with what has been found by Zlatanovic *et al.* It is important to note that whilst the validity of this figure of merit could be questioned beyond the TPA edge, it has been applied to the long wavelengths based on the non-zero values of the TPA parameter, and provides a clear indicator of the advantage of moving into a regime of low nonlinear loss. Thus, these results show that with a complete picture of the $\mathrm{FOM_{NL}}$ in the a-Si:H material, it is possible to access regimes of very highly nonlinear propagation. Specially, the $\mathrm{FOM_{NL}}$ for the a-Si:H fibre is 1.66 at $1.55\,\mu$m, which suggests that the nonlinear processes related to XPM is not efficient. However, this value still indicates that the material is promising in interferometric based switching applications that need a π phase shift. Furthermore, the $\mathrm{FOM_{NL}}$ for all the longer wavelengths is > 2, which suggest that a-Si:H material exhibits great potential for nonlinear applications in the extended wavelength band of telecom wavelength ($1.6\,\mu$m) to the mid-IR regime around $2\,\mu$m.

5.5 Mid-infrared supercontinuum generation

5.5.1 Introduction

In this section, the first demonstration of supercontinuum generation in a-Si:H core fibres is presented as an example of an application for our highly nonlinear fibres. Mid-IR supercontinnum sources present a promising approach to meeting the increasing demands for broadband, high-brightness radiation in various application areas, e.g. molecular fingerprinting, chemical sensing or gas detection. Physically the generation of the supercontinuum occurs when incident narrow-band pulses exhibit extreme spectral broadening from the interplay between soliton breakup, FWM, Raman effects, and dispersive wave generation [160]. All of these nonlinear effects can generate new frequencies and depend critically on the dispersive properties of the waveguides. Mid-IR supercontinuum generation in silicon waveguides has recently attracted much interest as silicon has inherent transparency and high nonlinearity in this region. In previous sections, the

a-Si:H material has been demonstrated to have enhanced nonlinearity for wavelengths beyond 2 μm. As discussed in Section 5.4, a-Si:H has a lower β_{TPA}, owing to its slightly larger bandgap energy, which results in a higher $\mathrm{FOM_{NL}}$. As a result, mid-IR supercontinuum generation has been realized in a-Si:H waveguides at much lower power levels than in their c-Si counterparts [99, 161]. In this section, I will attempt to give a general description of the first demonstration of mid-IR supercontinuum generated in a a-Si:H core fibre.

5.5.2 Optical properties of the small core a-Si:H fibre

As discussed in Section 3.2.5, the dispersion properties of the a-Si:H core fibre varied with the core diameter. The zero-dispersion wavelength (ZDW) of a 6 μm core diameter a-Si:H fibre is estimated to be beyond 4 μm, where it is difficult to find high power pulsed laser sources. For the wavelengths where the SPM induced spectral broadening was measured in Section 5.3.2, these large core fibres exhibits normal dispersion, thus resulting in fairly modest spectral broadening (maximum 200 nm). Similar with the reports on supercontinuum generation in the silica fibres, pumping in the anomalous wavelength region near the ZDW, can result in broadband supercontinuum generation predominantly governed by soliton fission and dispersive wave generation [160]. It is for this reason that most of the supercontinuum generation has been done in photonic crystal fibres as they provide the combined advantages of enhanced nonlinearity and extreme dispersion tailoring. Particularly for the silicon core fibres, dispersion engineering can be achieved by selecting a proper silica capillaries sizes prior to deposition. Previous simulation work revealed that the ZDW of the silicon core fibres can be shifted to $\lambda_Z \sim 2\,\mu$m by reducing the core size to diameters $d \sim 1.7\,\mu$m [156]. By accessing the anomalous dispersion in these fibres beyond 2.1 μm, there is potential for soliton propagation and FWM to be observed, which are very helpful for supercontinuum generation [162, 163]. As mentioned in Chapter 4, the smallest core fibre that have been characterised to date has a diameter of $d \sim 1.7\,\mu$m and a loss of 2.8 dB/cm at 1.55 μm. Figure 5.14 shows a scanning helium ion microscope (SHIM) image of this fibre core, together with the predicted group velocity dispersion (β_2) profile obtained from modal simulations using a full vector finite element method. As the dispersion of the a-Si:H is not yet well-known due to a lack of characterisations of this material, the higher order dispersion is not considered in the following analysis. However, it is an on-going project to allow for further understanding of the supercontinuum generation in a-Si:H core fibres.

As well as helping to engineer the dispersion, reducing the fibre core size enhances the nonlinearity via a reduction in the mode area. The effective area of the fundamental mode for the 1.7 μm core size fibre is estimated to be $A_{\mathrm{eff}} = 1.2\,\mu\mathrm{m}^2$ at 1.55 μm, which is a ten fold reduction of the value for the 6 μm core size fibre. This will result a ten times increase of the nonlinear strength γ as the nonlinear refractive index n_2 stays the same.

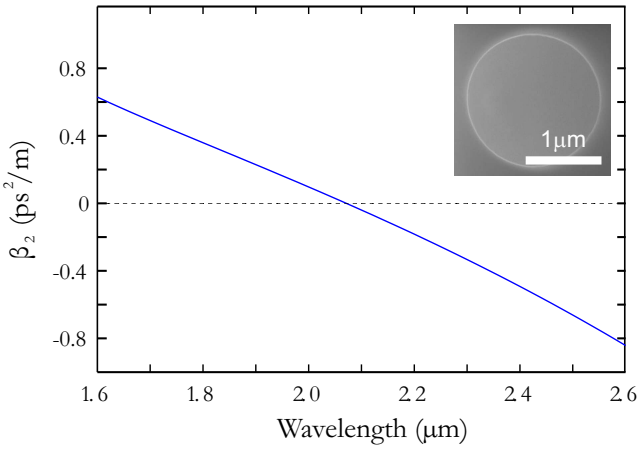

Figure 5.14: Simulated group velocity dispersion for a 1.7 μm diameter core a-Si:H fibre. Inset, scanning helium ion microscope (SHIM) image of the core.

Thus based on the two advantages discussed above, it is promising for the observation of nonlinear processes associated to supercontinuum generation such as modulation instability, FWM, and soliton effects in the fibres in the short wavelength edge of the mid-IR.

The details of the optical properties of the small core a-Si:H fibre used in the supercontinuum experiments are as follows. The fibre corresponds to Fibre M in Table 4.1. The effective area of the fundamental mode was estimated from simulations and found to increase as a function of wavelength as $A_{\text{eff}} = 1.2\,\mu\text{m}^2$ at 1.55 μm to $1.4\,\mu\text{m}^2$ at 2.4 μm. As can be seen from the dispersion curve in Figure 5.14, the estimated ZDW is $\sim 2.1\,\mu$m, and at wavelengths above this the fibre undergoes anomalous dispersion. The linear losses are 2.8 dB/cm at 1.55 μm and 0.8 dB/cm at 2.4 μm as shown in Figure 4.5(b). The nonlinear parameters are $n_2 = 1.7 \times 10^{-13}\,\text{cm}^2/\text{W}$ and $\beta_{\text{TPA}} = 0.7\,\text{cm/GW}$ at 1.55 μm, and $n_2 = 1.0 \times 10^{-13}\,\text{cm}^2/\text{W}$ and $\beta_{\text{TPA}} = 0.08\,\text{cm/GW}$ at 2.4 μm. The nonlinear absorption is negligible at 2.4 μm indicating that it is most likely beyond the TPA region, but preceding the region of higher nonlinear three-photon absorption (3PA) [164]. As a result, although the measured n_2 is smaller in the mid-IR, the significant reduction in the nonlinear absorption means that the overall FOM_{NL} in this regime is much larger. The FOM_{NL} is calculated to be ~ 22 at 2.4 μm using the pre-determined TPA coefficients and nonlinear refractive index, which exhibit a large increase when compared to the $\text{FOM}_{\text{NL}} \sim 1.6$ at 1.55 μm, so that both the linear and nonlinear properties of the fibre are favorable for long wavelength applications. The total fibre length after the characterisations is 4 mm, which is much larger than the nonlinear length ($L_{\text{NL}} \sim 0.61$mm at 2.4 μm for an input power of 75 W). Pump wavelengths in the window $2.1 - 2.5\,\mu$m were investigated as they are beyond the ZDW and in the anomalous dispersion region.

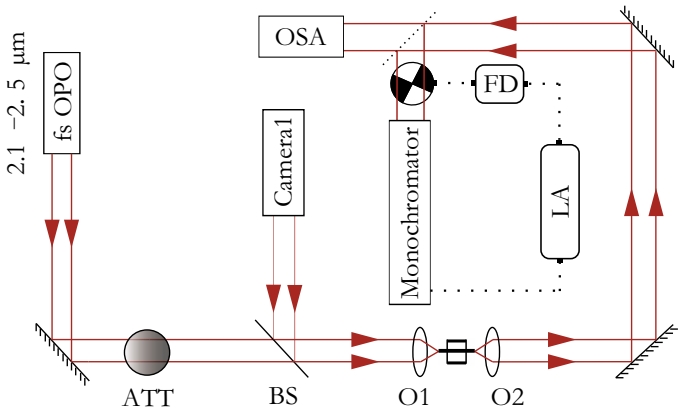

Figure 5.15: Experimental setup for supercontinuum generation.

5.5.3 Experimental setup

The experimental setup for supercontinuum generation in a a-Si:H core fibre is illustrated in Figure 5.15. To access high peak power at wavelengths beyond 2 μm, a Ti:sapphire pumped OPO (Radiantis Oria IR) which cover the selected pump wavelengths was employed that produced Gaussian shaped pulses of $\sim$ 300 fs (FWHM) duration at a 80 MHz repetition rate. A 63$\times$ magnification silica microscope objective lens was used to launch the light into the fibre core. However there is an issue induced by the small spot size which is that it is very easy to damage the fibre facet by melting the wax that holds it in place during the coupling adjustment. The melted wax flows onto the fibre facet smearing the fibre core. The fibre facet can then be easily burnt as the wax is over heated. This problem can be solved by carefully pulling out one side of the fibre slightly, about 1 mm from the mount, hence a clean fibre facet without wax can be obtained which can tolerate much higher powers. By optimizing the coupling conditions, the light was preferentially coupled into the fundamental mode of the a-Si:H core fibre, with a coupling loss of 6 dB (including Fresnel reflections), which is mostly due to the spot size mismatch. Since the transmission of the silica microscope objective is poor for mid-IR wavelenths beyond 2.5 μm, a ZnSe objective lens with a 6 mm focal length was used as the second lens to capture the broadband output. The output is then coupled into a long wavelength OSA (Yokogawa AQ6375) or a grating-based monochromator (Bentham TMc300). As the long wavelength OSA (Yokogawa AQ6375) only operates up to 2.4 μm, it was only used for the beam alignment. At the low starting input powers, the optimization of the light coupling was conducted by the OSA as it provides a fast scan time. The OSA was set to have a same resolution of 0.1 nm and sensitivity of -70 dBm for each measurement. The high power measurements were then monitored by the monochromator. To ensure efficient signal detection for the full range of powers, the detection of the signal in the monochromator is aided via the use of a lock-in amplifier connected to an optical chopper that modulates the beam at a frequency of 100 Hz.

The scan step of the monochromator was set to be 5 nm for each measurement and the detector in the monochromator was cooled using liquid nitrogen to improve the sensitivity.

5.5.4 Spectral dynamics

To obtain insight into the nonlinear processes that result in spectral broadening, the spectral evolution is investigated as a function of the input peak power. Figure 5.16 shows this evolution for a pump center wavelength of $\lambda_p = 2.28\,\mu$m. The pump peak power is increased from 1.9 W to 59 W, which corresponds to average output powers between 30 μW and $\sim$ 1 mW. When the input pump power is low, the spectrum exhibits little broadening and thus it is essentially free from nonlinear effects. Like our discussion in Section 5.3.2, this spectrum can be used as an indicator of the initial input pump pulse. When the input power is increased to 23 W, the pump spectrum is broadened by SPM. In the spectrum the residual pump does not exhibit the usual SPM induced oscillations, which was attributed to the chirp of the OPO pulse. The FWHM time-bandwidth product is calculated to be 0.56, which is larger than time-bandwidth product of the standard Gaussian pulse. Similar spectral features have been observed in the Section 5.3.2 when the OPO source was used as a pump source. It can be seen from Figure 5.16 that as the power increases the characteristic broad FWM sidebands start to appear on the spectral wings. The FWM peaks are chosen based on the slight bump on the shoulder of the broadening spectrum. Furthermore, the positions of these peaks detune continuously from the pump for increasing power. This is the first observation of FWM in a silicon fibre, which has been made possible due to the ability to access the anomalous dispersion regime in the small core fibre. These FWM peaks are not symmetric in silicon owing to the strong wavelength dependence of the linear and nonlinear losses. The higher order sidebands generated by the first order sidebands can be observed when the pump power is increased further. The similar FWM sidebands has been observed in a nanoscale a-Si:H waveguide on-chip [99].

The Raman effect is not included in the discussions as the Raman response is normally much smaller in amorphous material. Since the effects in a-Si:H core fibres has been studied in the previous sections, here our discussion focuses on the observation of the FWM sidebands. For a pump positioned in the anomalous dispersion regime close to the ZDW, the simplified phase-match condition of Equation 3.54 can be applied. From this equation, the maximum frequency shift can be estimated as $\Omega_{\max} = \pm\sqrt{2\gamma P_0/|\beta_2|}$, where P_0 is the peak pump power. Figure 5.17 compares the measured peak positions for the signal (circles) and idler (squares) with the wavelength shift calculated from $\Omega_{\max}$ (solid lines) for the estimated fibre dispersion at the pump wavelength ($\beta_2 = -0.3\,\mathrm{ps}^2/\mathrm{m}$), showing good agreement.

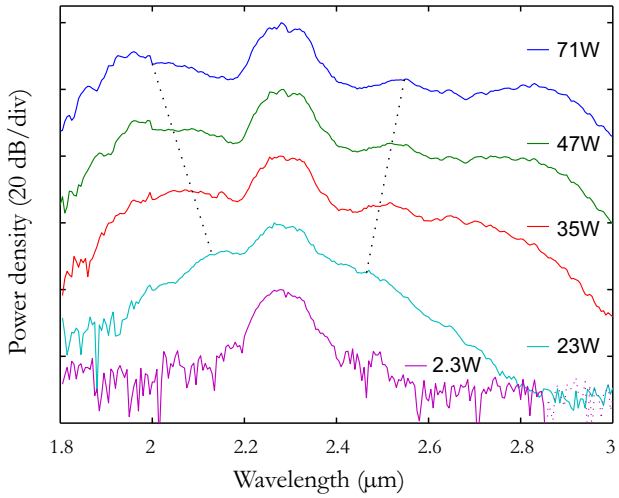

Figure 5.16: Measured spectra for the powers labeled in the legend. Dashed lines are a guide to show the power dependent FWM frequency detuning.

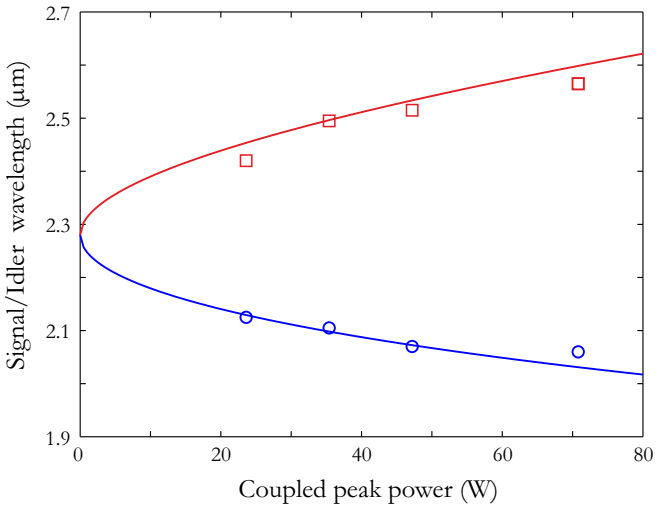

Figure 5.17: Peak FWM signal (circles) and idler (squares) wavelengths plotted with the phase-matched estimates from $\Omega_{\max}$ (solid lines).

In addition to power tuning, it is also possible to adjust the signal and idler positions through the choice of pump wavelength. Although the tunability of the FWM peaks is typically quite modest in the anomalous dispersion regime [165], these measurements provide a useful validation of the estimated fibre dispersion. As shown in Figure 5.18, the measured spectra are plotted for different pump wavelength from $2.19\,\mu\text{m} - 2.49\,\mu\text{m}$ (pump wavelength $2.28\,\mu\text{m}$ is already included in Figure 5.18). Figure 5.19 plots the measured signal and idler positions for a fixed input peak power of 20 W, which are in remarkable agreement with the predicted phase-matching curves over the pump wavelength range. Moreover, these results demonstrate that even in this low power regime it is possible to tune the wavelength conversion over 600 nm (1.99 to $2.61\,\mu\text{m}$), while only tuning the pump by 280 nm, and the tunability could be even greater if the power was

increased as in Figure 5.17.

As presented in Section 3.2.5.1, the GVD β_2 of the a-Si:H material was estimated using the parameters for the c-Si. This assumption was validated by the good agreement between the measured frequency shifts and theoretical prediction using the phase-match condition. These results are a good indication that the dispersion of our a-Si:H fibre material is similar to that of c-Si, which has also been recently reconfirmed by the experimentally measured GVD of a-Si:H waveguide using interferometric measurements [98, 100].

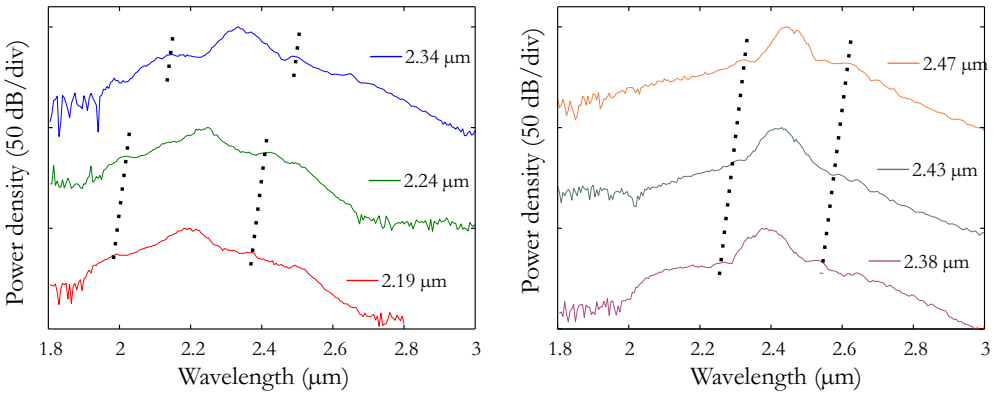

Figure 5.18: Measured spectra for the pump wavelengths labeled in the legend. Dashed lines are a guide to show the wavelength dependent FWM frequency detuning.

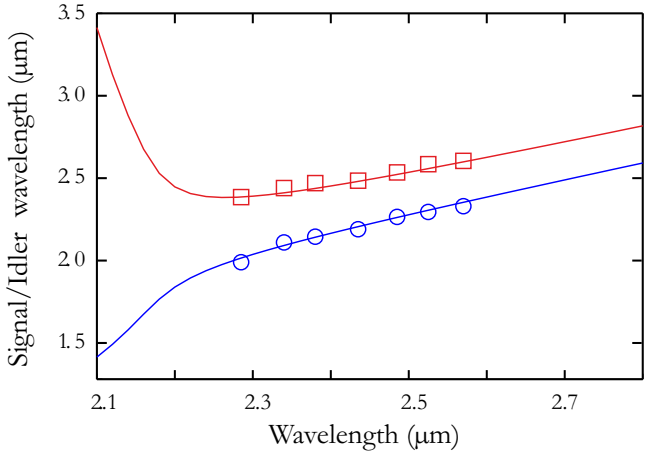

Figure 5.19: FWM signal (circles) and idler (squares) positions for a coupled peak power of 20 W, together with the phase-matching predictions for fibre dispersion (solid lines).

5.5.5 Supercontinuum generation

Returning to the high power scenarios in Figure 5.16, another notable feature of these spectra is the appearance of the second set of higher order FWM sidebands, most obvious on the longer wavelength side. Importantly, the phase-matching of cascaded FWM processes is expected to be aided by the short 4 mm fibre length used in these experiments, and that these processes can ultimately be exploited to generate broadband supercontinua [99, 166]. To investigate this, a series of high power measurements ($P_0 \sim 75$ W) were conducted for various pump wavelengths, with the resulting spectra shown in Figure 5.20. The bottom spectrum in Figure 5.20 corresponds to the same pump wavelength as Figure 5.16, but now both second order sidebands are clearly visible (separated by $\Omega_{\max} \sim 14$ THz) which is in good agreement with the prediction by the phase-match condition. It is worth noting that although the 30 dB bandwidth for this spectrum of 1200 nm has only increased by $\sim$ 100 nm compared to that for the 70 W pump, the flatness (defined as the ratio of the bandwidth and the standard deviation) has improved by almost 25 % [167]. The remaining spectra in Figure 5.20 were then taken for increasing longer pump wavelengths, where the linear and nonlinear losses are lower. Interestingly, as well as the expected increase in the spectral bandwidth (up to 1300 nm for $\lambda_p = 2.47\,\mu$m), these spectra exhibit an additional feature on the short wavelength edge of dispersive wave emission. Although dispersive waves are often associated with the onset of soliton fission, as the length of our fibre is shorter than the estimated fission length for the input pulses ($L_{\text{fiss}} \simeq L_D/N \sim 7$ mm, where $L_D \sim 64.9$ mm and $N \sim 10$ is the soliton order defined in Equation 3.60), I attribute their appearance in these spectra to the temporal breakup of pulses caused by FWM induced modulation [168]. Further verification for this is provided by the good agreement between the position of these short wavelength peaks (1.8 μm) and the predicted wavelength of the dispersive wave emission ($\lambda_{DW} \sim 1.75\,\mu$m) given by the phase-matching condition in Ref. [169], with the dispersion estimated from Figure 5.14. It is worth noting that these broader continuum spectra obtained for the longer pump wavelengths also exhibit a further improvement in the flatness of up to 30 %; however, unfortunately it was not possible to increase the pump wavelength beyond 2.5 μm as the silica input coupling lens became prohibitively lossy. Nevertheless, in all cases the spectra in Figure 5.20 exhibit more than an octave of continuum generation at the 30 dB level, with the total spectral coverage extending from 1.64 to 3.37 μm ($\sim$ 1700 nm), which it is believed to be the largest supercontinuum generated in a a-Si:H waveguide, and certainly within a core of micron sized dimensions.

5.5.6 Continuum generation in normal dispersion regime

For completeness the continuum generation has been investigated in the normal dispersion regime using pump wavelengths $\lambda_{zd} < 2.1\,\mu$m. As mentioned in previous discussions, the 6 μm diameter core a-Si:H fibres exhibit large normal dispersion at all the

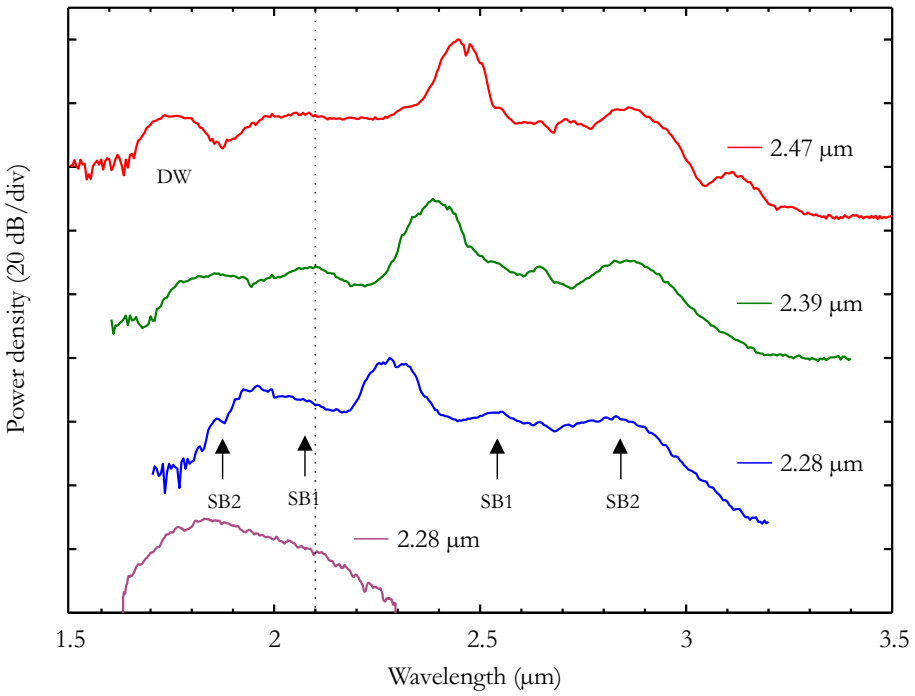

Figure 5.20: Supercontinuum spectra generated in the anomalous dispersion and normal dispersion regimes ($P_0 \sim 75$ W and central wavelengths as labeled). The dash line is the ZDW. The arrows indicate the positions of the 1st and 2nd order FWM sidebands (SB1 and SB2 in bottom spectrum) and the dispersive wave emission (DW in top spectrum).

pump wavelengths up to 3.7 μm, thus restricting the largest broadening to $\sim$ 200 nm for pump wavelengths around $\lambda_p = 2\,\mu$m. From the estimated dispersion curve in Figure 5.14, the 1.7 μm core size silicon fibre exhibits fairly low normal dispersion when pumped it on the short wavelength side of the ZDW. Figure 5.21 shows the spectral broadening generated by pumping at $\lambda_p = 1.85\,\mu$m in both the 1.7 μm and 6 μm core size silicon fibres. The spectral broadening of the small core fibre is up to $\sim$ 700 nm ($\sim$ 0.7 of an octave) when the input peak power is 75 W. The bandwidth of the continuum in the small core fibre is more than 3 times larger compared to that for the 6 μm core fibre pumped with input power 180 W and at a lower input peak power.

In the normal dispersion region, the spectral broadening is dominated by SPM and the approximately symmetric spectral properties are as expected (seen in the green curve in Figure 5.21) [88]. In the small core, the pump wavelength is close to the ZDW so that the new spectral components generated by SPM are in the vicinity of the ZDW, and thus the anomalous regime. Consequently, the soliton dynamics dominate the spectral broadening on the long wavelength side and cause the asymmetry of the spectrum. These spectral dynamics matches well with the simulation work in Ref. [160]. Hence, it can be concluded that the improvement of the continuum bandwidth is aided by both the enhanced nonlinearity from the reduced core size and engineered dispersion properties.

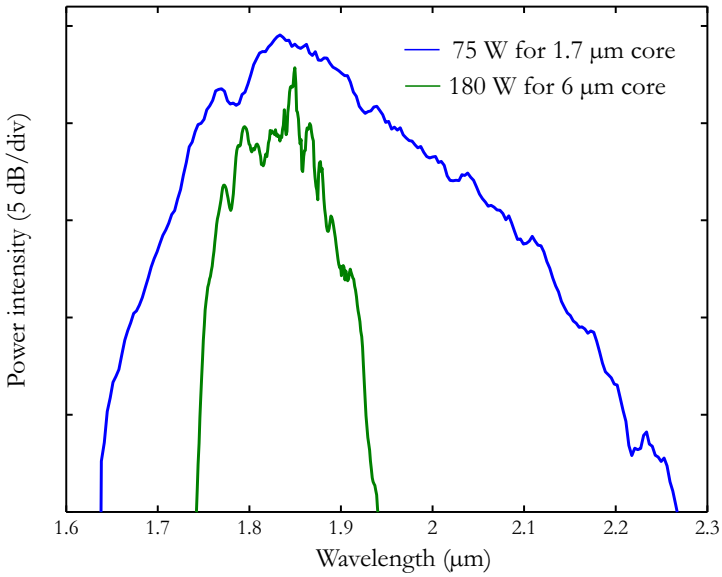

Figure 5.21: Continuum spectra generated in the normal dispersion regimes in silicon core fibres with two different core sizes, the pump peak powers are given in the legend.

Lastly, it is worth noting that although continua generated in the normal dispersion regime have reduced broadening, the improved flatness and coherence is likely to be of interest for applications in spectroscopy and metrology [170].

5.6 Conclusion

This chapter has presented the nonlinear characterization in silicon optical fibres from telecoms wavelengths, across the TPA edge, and up to the edge of the mid-IR regime. TPA and FCA are the main nonlinear absorption mechanisms in silicon at wavelengths in the TPA window. The most fundamental nonlinear process SPM, was also investigated in a-Si:H core fibre. From the experimental measurements and numerical modelling, the TPA and Kerr nonlinear parameters were obtained for a range of wavelengths. The dispersion curves obtained for the TPA and Kerr nonlinear parameters are in good qualitative agreement with the Kramers-Krönig transformations, and highlight the advantage of working beyond the TPA edge, where some of the highest values of the $\mathrm{FOM_{NL}}$ were obtained for this material to date. The results suggest that a-Si:H waveguides are a viable platform for nonlinear applications extending beyond telecoms, and into the short wavelength end of the mid-IR regime.

Additionally, I have extended our investigations of nonlinear propagation in the a-Si:H core fibres, demonstrating supercontinuum generation spanning more than an octave ($1.64\,\mu\mathrm{m}-3.34\,\mu\mathrm{m}$). The broadest bandwidths are obtained via a cascaded FWM process when pumped at wavelengths $> 2.1\,\mu\mathrm{m}$, where propagation in the $1.7\,\mu\mathrm{m}$ core fibre

is governed by anomalous dispersion and the a-Si:H material exhibits low linear and nonlinear losses. These fibres hold great promise for use at wavelengths beyond the telecom band, and by tuning the micron sized core dimensions, their applications may eventually extend much deeper into the mid-IR regime.

Chapter 6

Nonlinear properties in germanium on silicon waveguides

6.1 Introduction

In Chapter 4, the emerging germanium-on-silicon (Ge-on-Si) waveguides exhibited low loss across a broad wavelength range in the mid-infrared (mid-IR) region. Hence, they have potential for the development of integrated mid-IR photonic systems. Unlike silicon, the nonlinear effects in germanium are less well known. So far all of the experimental measurements of the nonlinear coefficients of germanium have been performed in bulk samples due to the fabrication challenges of germanium waveguides [75]. In this chapter, a full characterization of the nonlinear absorption in a Ge-on-Si waveguide across the two-photo absorption (TPA) window is presented. The main nonlinear absorption mechanisms in germanium are free carrier absorption (FCA) and TPA. As these processes can also be exploited to modulate the light signals, in the final section of this chapter, the first demonstrations of all-optical modulation will be presented for the Ge-on-Si waveguides.

6.2 Nonlinear absorption in germanium

The low loss transmission window of germanium starts from $\sim 2\,\mu$m and extends to $14\,\mu$m. Similar to silicon, in addition to the linear absorption, nonlinear absorption induced loss will also attenuate the transmitted light. TPA will be the dominant mechanism of nonlinear absorption for short pulse propagation until the TPA band edge ($\lambda = 3.7\,\mu$m for germanium). TPA induced FCA will also induce extra loss by the free-carrier plasma effect.

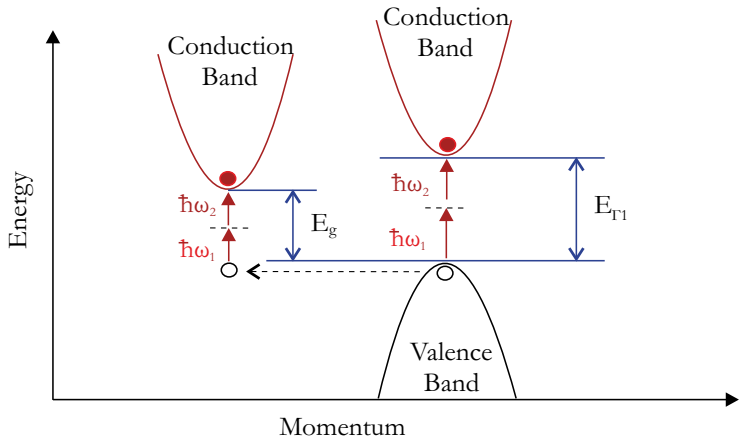

Figure 6.1: Schematic band structure of germanium illustrates TPA over indirect bandgap and direct bandgap.

6.2.1 Two-photon absorption

Like silicon, germanium is also a group IV semiconductor material with an indirect band structure. However, germanium is a peculiar indirect bandgap semiconductor as the indirect energy gap $E_g = 0.66\,eV$ is not much smaller than the direct bandgap $E_\Gamma = 0.82\,eV$. Thus, germanium is one of only a few semiconductors where indirect and direct absorption regimes can be accessed at comparable wavelengths. In Figure 6.1, the TPA process associated with the indirect gap is a phonon assisted three-particle process, which is similar to the TPA in silicon. For germanium, this TPA process has an efficiency of three orders of magnitude smaller than the direct gap transition which is also shown in Figure 6.1 [104].

The coefficients β_{TPA} of degenerate TPA in germanium at different wavelengths are commonly estimated using a two-model, direct bandgap model [171]. It can be expressed as follows:

$$\beta(\omega) = K\frac{1}{n^2 E_g^3}F_2(\frac{\hbar\omega}{E_g}), \tag{6.1}$$

where $F_2^{(i)}(x) = (2x-1)^{3/2}/(2x)^5$, K is a curve-fitting factor. Figure 6.2 shows the theoretical predictions for germanium's nonlinear absorption coefficients β_{TPA}, from which the nonlinear absorption of germanium is found to be orders of magnitude larger than silicon, around 1000× for β_{TPA} at its peak value. I have previously mentioned that all of the experimental measurements of the nonlinear coefficients have been performed in bulk germanium samples. Here the TPA coefficients in a germanium waveguide will be

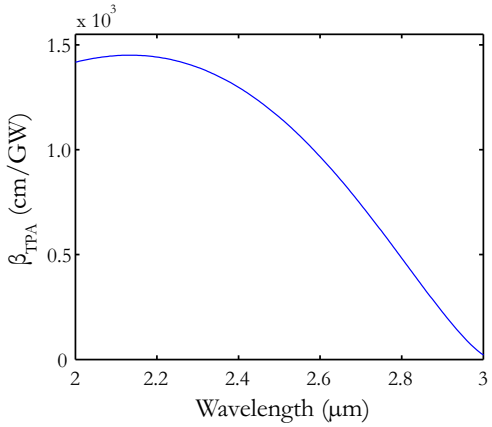

Figure 6.2: Predicted dispersion of nonlinear absorption coefficients β_{TPA} as a function of wavelength.

investigated for the first time using the nonlinear transmission measurement developed for the silicon fibres in the previous chapter.

6.2.2 Free carrier absorption

The FCA in germanium can be also described by Process [iv] of Figure 3.7. According to the Drude-Lorenz model given in Equation 3.31, the optical absorption in germanium shows quadratic dependence on the wavelength of the incident light. The value of the FCA coefficient σ is 4×10^{-17} at $2\,\mu$m from the literature [84]. In this thesis, the wavelength dependence of the FCA coefficient $\sigma(\lambda)$ is calculated via the Drude model based on these measured results. Although realistically the Drude model is inadequate for fully describing FCA and its wavelength dependence will not be presented in this thesis. This is because this variation only has minor impact in our simulation work when investigating the dominant TPA effect.

6.2.3 Free carrier lifetime in germanium

As discussed in Chapter 5, the free carrier lifetime can be obtained by studying the optical recovery of a CW signal following carriers excitation from a pulsed pump. In this experiment, a pump probe scheme was employed. A pulsed optical source was chosen for the pump at wavelength $\lambda_p = 1.54\,\mu$m which has a photon energy $h\nu_p$ greater than the band-gap energy E_g to generate free carriers in the waveguide. A CW probe was then positioned at various signal wavelengths λ_s with photon energies $h\nu_s < E_g$. When the probe is propagating in the waveguide, the free carriers generated by the pump pulse absorb photons of the CW probe, hence creating dark pulses or equivalently an inverted imprint of the pump on the probe signal. In this section, this modulation

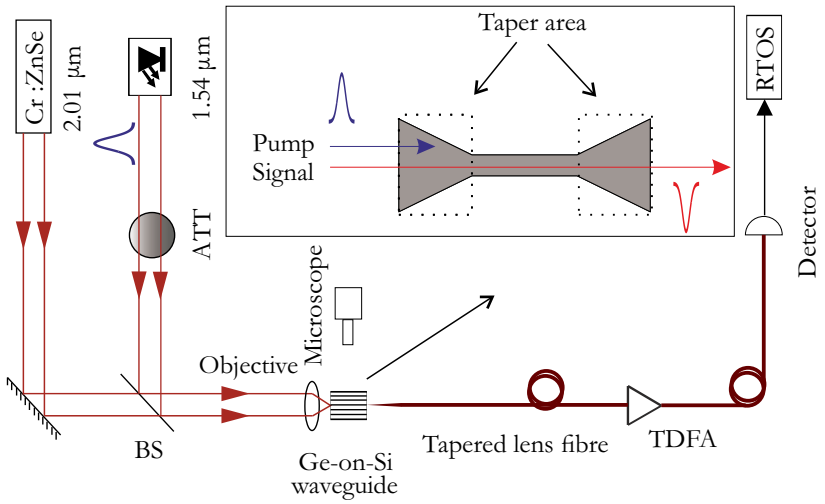

Figure 6.3: Pump probe experimental set-up to determine carrier lifetime in the Ge-on-Si waveguides. attenuator (ATT), beam-splitter (BS), thulium doped fibre amplifier (TDFA), and real time oscilloscope (RTOS).

was used to characterise the lifetime in the Ge-on-Si waveguide. As the pump energy is strong, the free carriers are excited deep into the conduction band states, which will add additional delay to the carrier lifetime.

The experiment makes use of the single photon excitation process to generate free carriers in the waveguide, which was described in Figure 3.7. The experimental setup is illustrated in Figure 6.3. In these measurements, the pump was chosen at a wavelength below the band edge of germanium ($\lambda < 1.9\,\mu$m) to efficiently excite the free carriers. Hence, the chosen pump source was a high power mode-locked fibre laser (Onefive ORIGAMI) operating at the telecommunications wavelength of 1.54 μm, with a pulse duration of 720 fs and a 40 MHz repetition rate. A Cr^{2+}:ZnSe laser (IPG Model SFTL-Cr-ZnSe-2300-1000) was used to generate a weak CW probe centred at 2.01 μm. As shown in Figure 4.10, the probe wavelength was positioned just on the edge of the high loss region of the material. Although not ideal, this short wavelength was chosen because I could make use of our fast, 10 GHz bandwidth InGaAs photodetector (EOT ET-5010F) which has a peak responsivity at 1.9 μm so that it was possible to study the temporal dynamics of the modulation. The pump and probe beams were combined with a pellicle beam-splitter (BS) before coupling into the waveguide using a 64 $\times$ microscope objective. As there are several waveguides on a single chip which are very close to each other, to aid with the coupling, a microscope (Veho 400x) was introduced to image the top of the chip surface. As the pump wavelength is below the band edge, it will be absorbed in the tapered area of the waveguide (shown in the inset of Figure 6.3) thus the carriers recovery in this experiment happened realistically in the relatively large tapered area (maximum width 10 μm). The only output from the waveguide was the modulated mid-IR probe light and collected by a tapered lens fibre. The estimated coupling loss for this experiment arrangement was 9.8 dB. Thus, the output probe light was amplified by

a custom built 2 μm thulium-doped fibre amplifier to compensate for the coupling losses as well as the transmission loss of the Ge-on-Si waveguide. The optical signal was detected via the InGaAs photodetector and the converted electrical signal was monitored on a real time oscilloscope with 12 GHz bandwidth (Agilent).

In this experiment, a co-propagating scheme was chosen because of its simplicity compared with illuminating the pump light from the top to the waveguide with only 2.25 μm wide. The experiment setup for the top illuminating is much more complex thus it is not suitable for this first carrier lifetime measurement in a Ge-on-Si waveguide. However, in this co-propagating configuration the absorption of the pump occurred in the tapered region near the waveguide input thus resulting in longer recombination time. The lifetime measurement was performed on Ge-on-Si waveguides C of Table 4.2 for which the propagation loss of the TE mode was measured to be 3.9 dB/cm at 2 μm in Section 4.4.4. Figure 6.4 shows the free carrier modulated probe amplitude for a coupled signal power of $\sim$ 1 mW, and a pump energy of 44 pJ. Unfortunately, owing to the limited bandwidth of our commercially available 2 μm detector, it was not possible to fully resolve the fast build-up of free carriers that are generated on the timescale of femtosecond pump pulse [25]. However, the slower dynamics associated with the free carrier recombination can be clearly resolved, and through an exponential fit to the recovery (dashed lines) using Equation 5.3, the free carrier lifetime can be estimated to be $\tau \sim 18$ ns. This lifetime is considerably faster than what has been reported for bulk germanium samples ($\tau \sim \mu$s), as expected for a confined waveguide geometry [172]. Furthermore, as the recombination is taking place in the larger tapered input (10 μm), this lifetime is also faster than what has been measured for silicon waveguides with similar micron sized core dimensions [173], which is attributed to the increased carrier mobility of germanium. As the two main mechanisms for removing carriers from the core of a rib waveguide are diffusion from the rib [173], and recombination via surface and interface states [174], the lifetime should be even lower in the smaller core section of the Ge-on-Si waveguides. Thus a route to improving the speed of our system would be to pump the 2.25 μm core from the top, though this would come at the expense of a reduced pump/probe overlap, and would also greatly complicate the experimental setup [25, 175]. Like silicon, the carrier plasma dispersion effect can be used to achieve all-optical modulation which will be described in the following sections.

6.2.4 Characterisation of nonlinear absorption

The nonlinear absorption in Ge-on-Si waveguides was characterised via high power transmission experiments, as previously described for the silicon core fibres in Chapter 5. The experimental setup is illustrated in Figure 6.5, where two mid-IR cameras were used to image the input facet and the output beam profile of the waveguide. In this section, the investigations of β_{TPA} were carried out for a range of wavelengths, from 1.9 to 3.7 μm,

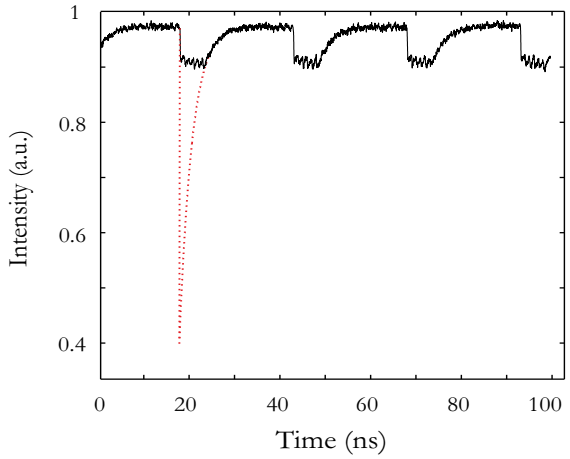

Figure 6.4: Free carrier based absorption on the probe of a $\lambda \sim 2\,\mu$m signal. The dashed line is an exponential fit to determine the free carrier lifetime.

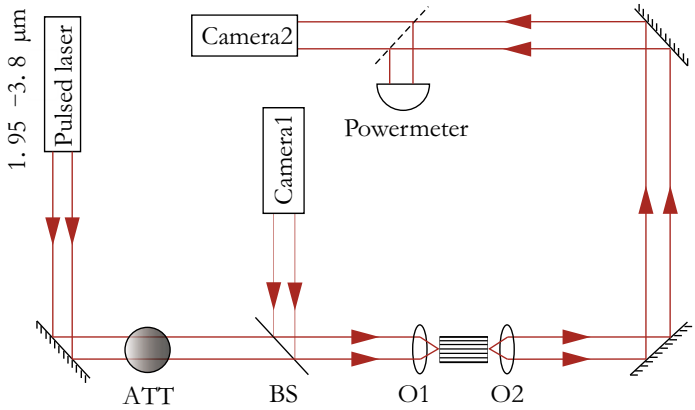

Figure 6.5: Experimental setup for nonlinear absorption characterisation in Ge-on-Si waveguide.

over the TPA window for germanium. The high power pump pulses were provided by a long wavelength Ti:sapphire pumped OPO (Radiantis Oria IR), with a pulse duration of ~ 250 fs (FWHM) at 80 MHz repetition rate. As the silica lens is not suitable for wavelengths longer than 2.7 μm, an aspheric chalcogenide lens with a focal length of 1.87 mm was used to launch the beam into the waveguide. A second ZnSe objective with a 6 mm focal length was used to couple the output light onto a Spricon Pyrocam III Series camera. The use of these mid-IR cameras ensured efficient coupling into waveguide core so that the fundamental mode was primarily excited. Finally, both the input and output power were measured using a PbSe pre-amplified photoconductive detector. A conventional graded neutral density silica attenuator was used to control the input power.

The Ge-on-Si waveguide was first characterised at 1.94 μm using a fibre laser (AdValue Photonics AP-ML) which is near the band edge wavelength ($\sim 2\,\mu$m). Similar to the

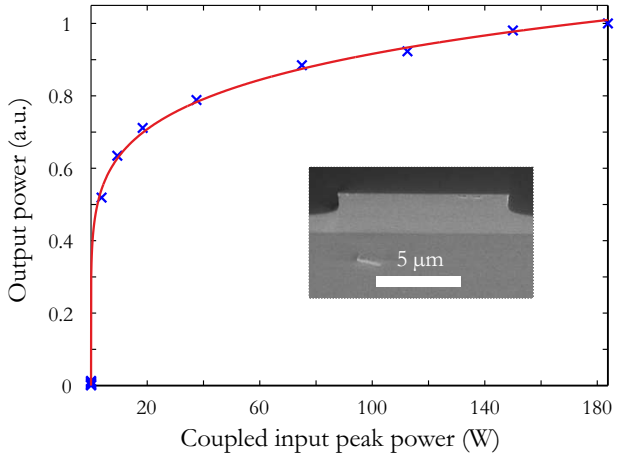

Figure 6.6: Normalized output power as a function of coupled input peak power showing the onset of nonlinear absorption. The solid curve is the simulated fit obtained via solving Equations 5.4 and 5.5.

carrier lifetime measurement, TPA is mainly occurred in the taper area of the Ge-on-Si waveguide. The effective mode area A_{eff} was estimated to be around $10\,\mu m^2$ at the pump wavelength using a full vector finite element method for the taper with $10 \times 2.25\,\mu m$ cross section as shown by the SEM image in the inset of Figure 4.8. Figure 6.6 shows the normalised measured output power as a function of coupled input power demonstrating the characteristic optical limiting behaviour associated with strong TPA induced absorption. Again, the transmission data is fitted by the theoretical simulations using the simplified coupled-mode Equations 5.4 and 5.5. It is worth noting that the length of the Ge-on-Si waveguides used for these measurements were shorter than the dispersion length and the simplified set of equations could be used. By applying the same fitting method with the pre-determined parameters in Table 6.1, the value of β_{TPA} is found to be $1240\,cm^2/GW$, which is in excellent agreement with the simple band model prediction in Figure 6.2. A large value found for β_{TPA} at this wavelength which is close to band gap edge of the germanium material. This value is around three orders of magnitude larger than that of silicon at its peak value.

6.2.5 Nonlinear absorption across the TPA edge

In order to fill some of the spectral "gaps" left by the previous reports of β_{TPA} in germanium, the nonlinear absorption measurements were extended to other preselected wavelengths from 1.9 to $3.7\,\mu m$, i.e. across the entire TPA window. For each wavelength, the output power was recorded as a function of coupled input peak power and the results are plotted in Figure 6.7. For all the wavelengths up to $3.4\,\mu m$, it is obvious that the output power saturates due to the strong nonlinear absorption caused by TPA. In contrast, the largely linear trend exhibited for the longest wavelength ($\lambda = 3.7\,\mu m$), which continues up to input power of 6 W shown in Figure 6.7(b) indicates that TPA is

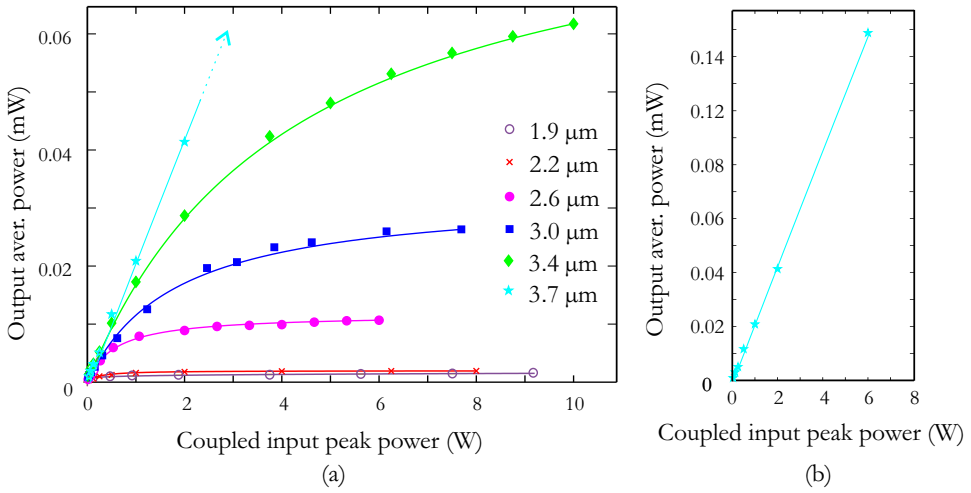

Figure 6.7: (a) Nonlinear absorption measurements for the wavelengths given in the legend. The solid curves are the simulated fits obtained via solving Equations 5.4 and 5.5 for the corresponding wavelength. (b)The complete transmission curve for pump wavelength at 3.7 μm.

essentially negligible at this wavelength. As a result, this data provides an indication of the TPA edge of the germanium material, which is likely to be in the region of 3.7 μm, or $E_g/2 \sim 0.335\,\text{eV}$. These results were in good agreement with the direct bandgap energy of germanium.

The linear loss used in the simulations are from Figure 4.9. $\sigma(\lambda)$ is calculated via the Drude model based on the measured results from [84], as discussed in Section 6.2.2. The corresponding values obtained for the TPA parameters are plotted as a function of wavelength in Figure 6.8. These results show that the β_{TPA} initially drops sharply from $1240 \pm 50\,\text{cm/GW}$ down to $50 \pm 10\,\text{cm/GW}$ as the wavelength increases from the edge of the germanium transmission window to the mid-IR regime. Eventually the value of β_{TPA} reaches a negligible value of $1 \pm 0.5\,\text{cm/GW}$ at the wavelength of 3.7 μm. This trend of decreasing β_{TPA} is as what would be expected for wavelengths across the TPA window, and specifically, this would be also expected to drop to a negligible value as the

Table 6.1: Pre-determined parameters at 1.94 μm of the Ge-on-Si waveguides for nonlinear characterisation.

Property	Units	Value
Length	cm	1.2
Linear Loss	dB/cm	6
Effective Area	μm^2	10
Carrier Life Time	ns	18
FCA Coefficient	cm^2	4×10^{-17}

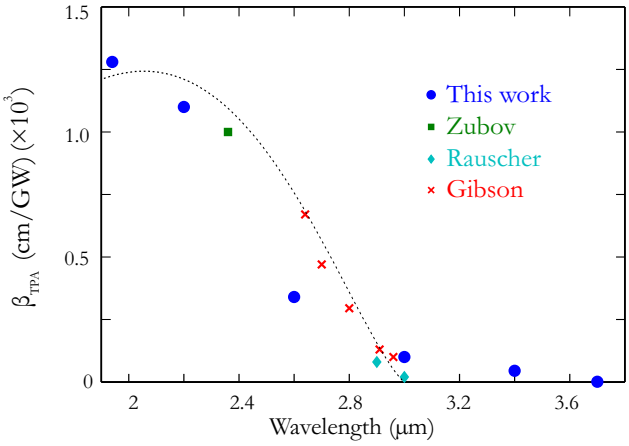

Figure 6.8: TPA parameter as a function of wavelength extracted from Figure 6.7 and data points from Refs. [82] (rectangle), [83] (crosses), and [84] (diamonds). The dash line is the theoretical fitting for all the measured results.

wavelength approaches the TPA edge ($\lambda = 3.7\,\mu$m), where the sum of the energies of the two photons is no longer sufficient to span the bandgap. These measured β_{TPA} values are consistent with the values reported by Zubov, Gibson *et al.* and Rauscher *et al.* in the wavelength region from 2.6 to 3.0 μm. These earlier β_{TPA} values are plotted along with the measurements from this work, together with the two-band model based upon the direct bandgap of germanium, by changing the fitting factor K in Equation 6.1 as shown by the dash line in Figure 6.8. As it can be seen, the very high β_{TPA} values for germanium from 1.9 to 2.6 μm are in excellent agreement with the theoretical prediction. In this work, the slow roll off the TPA parameters at longer wavelengths is due to the both indirect and direct bandgap energy of Ge and the larger measurement errors at longer pump wavelength.

I believe that this systematical study of the dispersion of the β_{TPA} values in the Ge-on-Si waveguides, it will provide useful information regarding the potential to migrate these applicaions to the Ge-on-Si platform for the mid-IR wavelengths. In Sections 6.4.2, the demonstrations of all-optical modulation of mid-IR wavelengths are presented as an example of these TPA based application in the Ge-on-Si waveguides with strong nonlinear absorption.

6.3 Figure of merit

As discussed in Section 5.4, a FOM_{NL} can be defined as the normalised ratio of the Kerr coefficient n_2 to the TPA parameter β_{TPA} and used to evaluate the potential value of the nonlinear waveguides. Although the investigations of the n_2 parameter in the Ge-on-Si waveguides are still on-going, the FOM_{NL} can be estimated using the measured β_{TPA} and the theoretical predicted curve for the dispersion of n_2 in Figure 6.9(a) from which

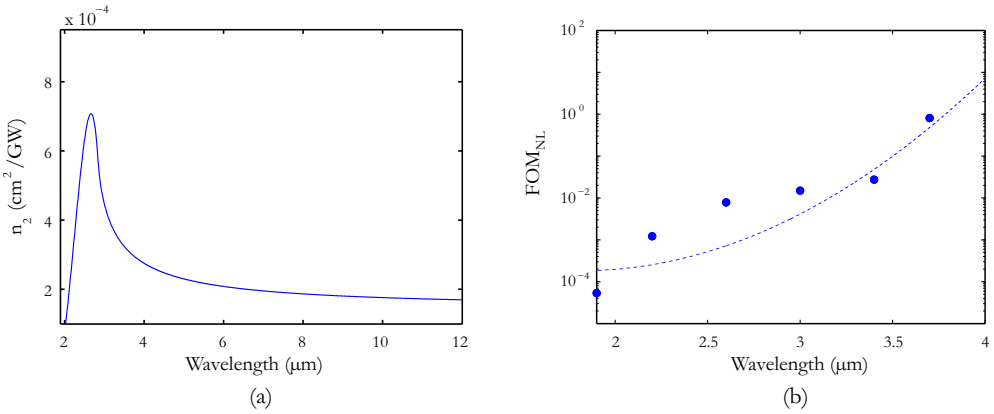

Figure 6.9: (a) Predicted dispersion of Kerr nonlinear coefficient n_2. (b) Theoretical $\mathrm{FOM_{NL}}$ dispersion.

has been taken from Ref. [29]. The predicted dispersion of the $\mathrm{FOM_{NL}}$ is shown in Figure 6.9(b). Similar to silicon, germanium is expected to exhibit a monotonic increase in the $\mathrm{FOM_{NL}}$. As the wavelength approaches the TPA edge, it shows a much higher order increase compared with silicon. It is worth noting that the effect of the MPA absorption on the $\mathrm{FOM_{NL}}$ was ignored as it has minimal impact at these waveguides [176]. As the Kerr nonlinearity remains large even for wavelength beyong the TPA edge, the use of Ge-on-Si waveguides for nonlinear applications can be exploited in the TPA free wavelength regime. From the rapid increasing trend of the predicted $\mathrm{FOM_{NL}}$ curve, the great potential of the Ge-on-Si platform for exploiting nonlinear effects especially for wavelength beyond $4\,\mu$m drives our further investigations moving towards to longer wavelengths in the mid-IR.

6.4 All-optical modulation

6.4.1 Free carrier absorption based modulation

Similar to what has been demonstrated in silicon devices [177], the plasma dispersion effect in germanium can be used for all-optical modulation. In this section, I have extended the pump-probe experiments used in the lifetime measurement for different wavelengths, thus demonstrate all-optical modulation in the Ge-on-Si waveguides.

6.4.1.1 Modulation setup

To demonstrate all-optical modulation in the Ge-on-Si waveguides, a series of pump-probe experiments were undertaken across the $2-3.2\,\mu$m wavelength region using two different sources. The experimental set-up is based on the free carrier lifetime measurement, with a slight modification to the collection of the output signal, as shown in

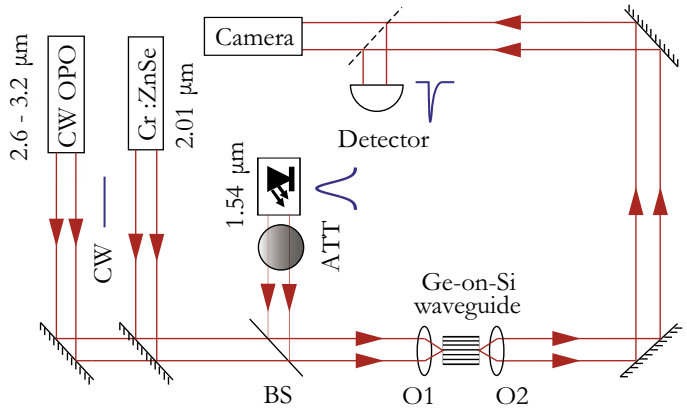

Figure 6.10: Experimental setup to demonstrate all-optical modulation in the Ge-on-Si waveguides. ATT, attenuator, BS, beam-splitter, O1 & O2, microscope objective lenses.

Figure 6.10. The low power signal was provided by either the Cr^{2+}:ZnSe laser (IPG Model SFTL-Cr-ZnSe-2300-1000) or the Aculight CW OPO so that modulation could be investigated over the selected wavelengths of $\lambda = 2.01$, 2.6, 3.0, and $3.2\,\mu$m. In all cases the pump and probe beams were combined with a pellicle beam-splitter (BS) before coupling into the waveguide using an appropriate objective. As the the silica coupling objective and lens taper was impossible to use for the longer wavelength, an aspheric chalcogenide lens with a focal length of 1.875 mm was used to couple light from the OPO. The output was then collected via a ZnSe objective with a 6 mm focal length. A PbSe detector was used to measure the power change of the modulated light, which can be used to estimate the total absorbed power.

6.4.1.2 Modulation results and discussions

Although it is not possible to directly measure the modulation depth with any of our detectors, it can be estimated from the lower bound in the exponential fit (shown in Figure 6.4) as the pump induced carrier generation can be regard as instantaneous when compared to the slow recovery time [25]. From Figure 6.4, the modulation depth is around ~ 4 dB at a pump wavelength of $2.01\,\mu$m close to the band edge. The remaining measurements were then conducted within the lower loss, longer wavelength region for $\lambda = 2.6\,\mu$m and $3\,\mu$m, and $3.2\,\mu$m using the CW OPO. As plotted in Figure 6.11(a), the maximum extinctions at these wavelengths are 4.6 dB , 4.8 dB and 5.1 dB, respectively. The trend of increasing modulation depth for increasing wavelength is due to the larger FCA coefficient and the larger mode size in the longer wavelength region [175]. Thus, this observation is promising for applications extending even further into the mid-IR. Figure 6.11(b) then shows a plot of the modulation depth as a function of the pump pulse energy for the longest signal wavelength of $3.2\,\mu$m, showing the expected trend of

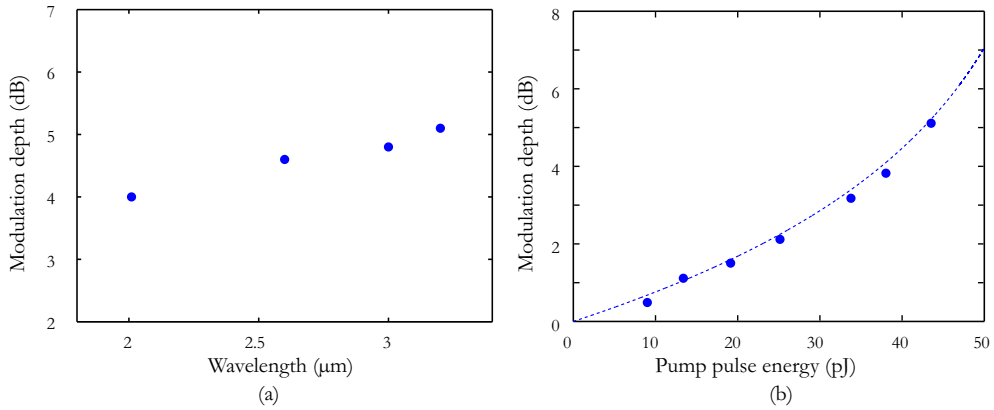

Figure 6.11: (a) Modulation depth as a function of pump wavelength. (b) Modulation depth as a function of pump pulse energy for a signal wavelength of $\lambda = 3.2\,\mu$m.

increasing modulation for increasing pump power. The highest modulation depth 5.1 dB was only limited by the available pump energy. However, in this free carrier absorption based modulation, the modulation rate is determined by the lifetime, thus the operation speed will be on the order of ~ 50 MHz.

Unfortunately the speeds of this modulation scheme will always be limited by the free carrier lifetime, which typically ranges from tens of picoseconds in nanoscale silicon wires, to hundreds of nanoseconds in micron-sized waveguides. As germanium has better carrier mobility [179], the germanium based device is expected to have faster modulation speed. However the carrier lifetime in the first generation of the Ge-on-Si waveguides is still at the order of nanoseconds due to large waveguide dimension. This could be increased by simply reducing the waveguide dimensions or by applying free carrier sweep-out [178].

6.4.2 Cross-absorption modulation using two-photon absorption

In an effort to increase the modulation speed, an experiment focused on a TPA based absorption modulation scheme was undertaken. β_{TPA} is associated with the $\chi^{(3)}$ nonlinear process which is ultrafast. The ultrafast nature of TPA can be exploited to realize a number of all-optical processing functions such as pulse shapers, logic gates, modulators, switches and detectors [145, 180]. A high-speed, all-optical XAM process using a simple pump-probe experiment can be demonstrated in the Ge-on-Si waveguide by exploiting the large β_{TPA} parameter at $\sim 2\,\mu$m. This method is capable of achieving a high temporal resolution when combined with lock-in detection. As this scheme is based on TPA, one photon from the high intensity pump is combined with another from the weak probe so that there is enough energy to span the bandgap and to be absorbed. As a result, photons will be removed from the probe that are otherwise too weak to induce TPA, producing a modulation that is an inversion of the pump. The probe pulse

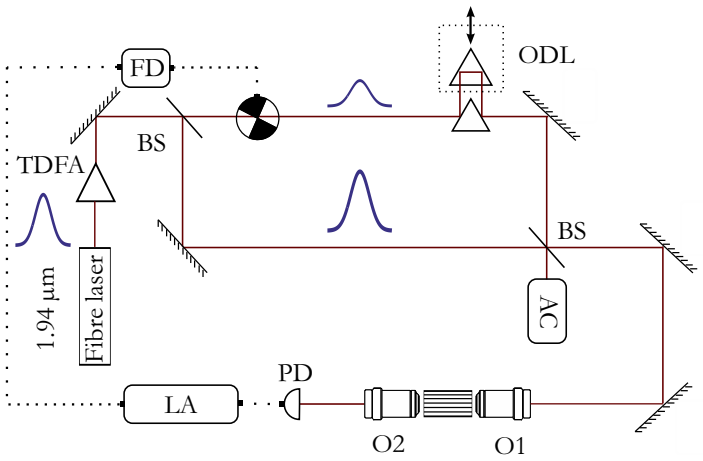

Figure 6.12: Experimental setup to demonstrate all-optical modulation using TPA in the Ge-on-Si waveguides. Optical delay line (ODL), Autocorrelator (AC), Photodiode (PD), Lock-in amplifier (LA), Frequency driver (FD), Microscope objective lenses (O1 & O2) and beam-splitter (BS).

can be a small fraction of the pump pulse so that the pump and signal wavelength are the same (i.e. degenerate TPA), or may involve a different wavelength signal pulse (i.e. non-degenerate TPA). In this section, only the degenerate case is considered because there were not two different sources with the same repetition at these long wavelengths.

6.4.2.1 Experimental setup for cross-absorption modulation

The setup for this experiment is illustrated in Figure 6.12. A mode-locked fibre laser (AdValue Photonics AP-ML) was used to generate optical pulses with 25 MHz repetition rate at 1.94 μm and was amplified using a custom built thulium-doped fibre amplifier to boost the power [181]. The amplified pulse has a duration of 5 ps FWHM. The laser light was then split into a high power pump pulse (maximum 10 W coupled peak power) and a weak probe pulse ($\sim$ 10 mW coupled peak power). A variable time delay was introduced between the probe and pump pulses by a retroreflector prism mounted on a motorized stage. The probe was modulated using an optical chopper so that a lock-in amplifier could be used to discriminate between the pump and probe signal. The pump and probe beams were then combined with a pellicle beam-splitter (BS) before coupling into and out of the waveguide using two 40 $\times$ silica objective lenses with a numerical aperture of 0.65. The transmitted output power was measured using a PbSe pre-amplified photoconductive detector via the lock-in amplifier over continuous scans of different time delays.

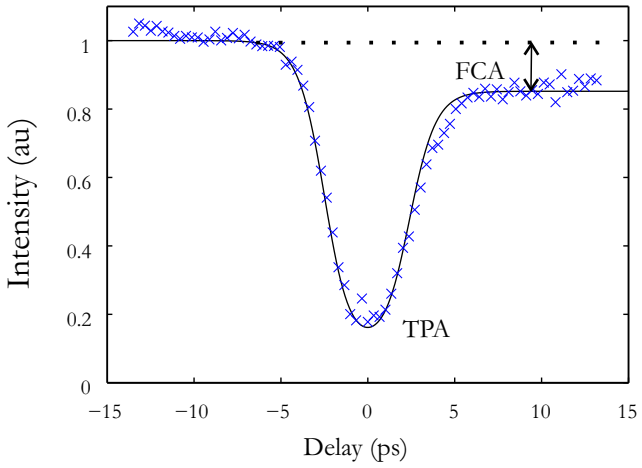

Figure 6.13: Measured nonlinear absorption of the weak probe pulse (blue crosses) together with the simulated fit (black line).

6.4.2.2 Modulation results and discussions

Once again, as this work are primarily interested in the power evolution, by ignoring the effects of spectral modulation, this process can be described by simplified coupled NLSEs as [141]:

$$\frac{\partial A_2(t,z)}{\partial z} = -\frac{\alpha_l}{2}A_2(t,z) - \frac{1}{2}\sigma_{\mathrm{FCA}}N_c(t,z)A_2(t,z) - \beta_{\mathrm{TPA}}I_1(t,z)A_2(t,z), \quad (6.2a)$$

$$\frac{\partial I_1(t,z)}{\partial z} = -\alpha_l I_1(t,z) - \sigma_{\mathrm{FCA}}N_c(t,z)I_1(t,z) - \beta_{\mathrm{TPA}}I_1^2(t,z). \quad (6.2b)$$

In these equations, $A_2(t,z)$ is the field amplitude of the probe, $I_1(t,z)$ is the intensity profile of the pump, $N_c(t,z)$ is given by Equation 5.5 with $I = I_1$, and the low power probe is assumed to have a negligible influence on the pump.

Figure 6.13 plots the absorption of the probe as a function of delay for a coupled pump peak power of 10 W, corresponding to only 4 mW of average power. The measured response clearly shows that the ultrafast absorption due to TPA occurs on the timescale of the pump pulse, thus allowing for modulation speeds of up to $\sim$ 200 GHz for our 5 ps pulses. It is worth noting that this could be made even faster by employing sub-picosecond pulses (THz speeds). However, it is clear from the slower recovery seen on the tail of the response in Figure 6.13 that our current set-up will ultimately be limited by the slow free carrier recombination time, as discussed in Section 6.4.1. Again this could be mitigated by applying a simple carrier sweep-out scheme. Fitting the response curve with Equation 6.2 and Equation 5.5 and $\beta_{\mathrm{TPA}} = 1280$ cm/GW from Figure 6.8, an excellent agreement (solid line) is obtained, thus providing further verification of the results of the TPA characterization. Although similar modulations have been demonstrated in silicon

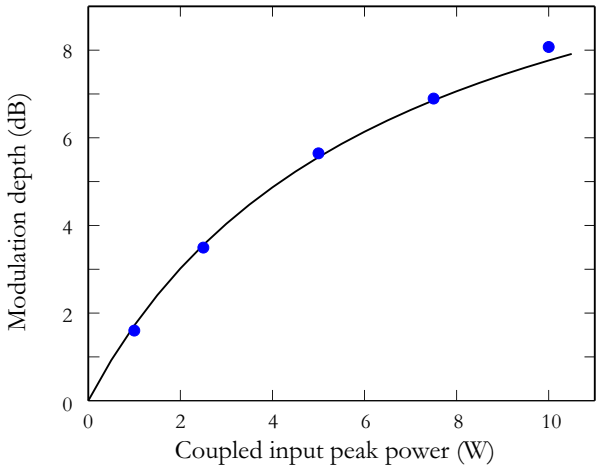

Figure 6.14: Modulation depth as a function of coupled input pump peak power.

based waveguides, this is the first demonstration of ultrafast modulation via TPA in this Ge-on-Si waveguide platform.

Repeating these measurements for different pump powers produces the expected trend of increasing modulation depth for increasing power, as shown in Figure 6.14. The solid line is obtained from the simplified equations and the carrier rate equation which is in good agreement with our measured modulation depth. I note that the high power roll-off is associated with the saturating pump. The maximum extinction ratio of 8.1 dB is the highest reported in any of the group IV waveguides to date [182, 183], which is most likely due to the very large nonlinear absorption accessed in this experiment. Furthermore, as β_{TPA} remains strong (compared to silicon) throughout the $2-3\,\mu$m pump range, it should be straightforward to extend this scheme to develop high-speed, high-extinction modulators across this important wavelength region for the potential applications i.e. $2\,\mu$m optical communications.

6.5 Conclusions

In this chapter, the nonlinear transmission properties of Ge-on-Si waveguides have been characterized across a transmission window in the mid-IR regime. The dispersion curves obtained for the β_{TPA} parameter are in good agreement with the theoretical predictions and early reports in the literature. All-optical modulation of the mid-IR light has been demonstrated for selected wavelengths across the $2-3.2\,\mu$m region by both the FCA and TPA absorption schemes. The modulation depth obtained is as high as ~ 8 dB, at speeds of tens of MHz (for the FCA-based modulation) to hundreds of GHz (for the TPA-based modulation). Since these waveguides have been shown to exhibit low losses

that are relatively independent of wavelength over the range $2 - 3.8\,\mu$m, I expect that the transmission region should extend well into the mid-IR. Thus it should be straightforward to apply these absorption based modulation schemes to longer wavelengths to develop integrated devices for sensing and spectroscopy applications. I expect that continued efforts to understand the properties of this highly nonlinear material will play a key role in the development of future mid-IR systems.

Chapter 7

Conclusions

7.1 Summary of the thesis

My PhD project has met the objectives of testing novel semiconductor waveguide platforms for the mid-infrared (mid-IR) regime. Two particular waveguides have been investigated in this work; semiconductor core optical fibres and germanium-on-silicon (Ge-on-Si) rib waveguides. The semiconductor core fibre platform offers the capability of combining the flexible light guiding ability of fibres with the rich optoelectronic functionality of semiconductors in integrated fibre geometry. While germanium offers the ability to extend the current existing silicon base integrated photonics circle to the mid-IR regime. Moreover, compared to silicon, germanium offers a number of other advantages such as broader transparent window, higher nonlinear and the potential to produce active devices based on germanium-based alloys.

In this thesis, the linear transmission characterisations of semiconductor waveguides have been presented. The limitations of the transmission window are the same for these two types waveguides, which are due to the absorption of the cladding material ($3.8\,\mu$m for silica cladding and $7.8\,\mu$m for silicon substrate), thus the transmission window can be extended to longer wavelengths by carefully designing the waveguides to decrease the optical mode leakage to the cladding. Investigations of nonlinear properties of the silicon and germanium waveguides in the mid-IR are the focus of this work as they can be exploited to develop a large range of functional optical devices. The fabrication process and linear optical properties characterisations of the two aforementioned semiconductor waveguides are introduced in Chapter 4, whereas the nonlinear properties and associated applications are included in Chapter 5 and Chapter 6 with particular emphasis in the mid-IR wavelength region.

In Chapter 4, the fabrication techniques used for depositing the semiconductor optical fibres, namely high pressure chemical vapour deposition (HPCVD), was introduced in

detail. In terms of core materials, silicon and germanium core fibres were fabricated and they showed different optical properties. For the a-Si:H fibres, two particular fibre core sizes (6 μm and 1.7 μm) were studied. Using the HPCVD process, hydrogenated amorphous silicon (a-Si:H) and polycrystalline silicon (p-Si) can be deposited under different temperatures. Specifically, a-Si:H core fibre can be fabricated by keeping the temperatures below 450 °C as it is below the nucleation temperature 520 °C of silicon and can suppress out diffusion of hydrogen to passivate the dangle bonds. The a-Si:H core fibres exhibited low linear optical losses over the entire wavelength range from near infrared to the mid-IR regime. The lowest loss measured for the 6 μm core diameter fibre was 0.29 dB/cm at 2.7 μm, which is a significant decrease from those measured in the near infrared wavelength regime. The 3 dB/cm loss measured for the 1.7 μm core diameter fibre was slightly higher than that of the 6 μm core fibre, however, it decreased to 0.8 dB/cm at 2.4 μm.

For p-Si core fibres, they can be fabricated by post annealing the a-Si core fibre. The two-step annealing method used in this thesis improved the optical properties compared with the previous single step method. A reduction of a few dB/cm in linear loss was demonstrated over the entire wavelength regime thus making the lowest loss 0.99 dB/cm at 2.2 μm. This is just below the threshold of 1 dB/cm often considered necessary for many photonic and optoelectronic applications.

Hydrogenated amorphous germanium (a-Ge:H) core fibre can also be deposited using HPCVD. By keeping high hydrogen content thereby passivizing dangling bonds, it leads to a decrease in the number of scattering centers and ultimately the optical loss was reduced by an order of magnitude.

The germanium rib waveguides were fabricated on the Ge-on-Si wafer with different germanium film thicknesses. The Ge-on-Si waveguide exhibited loss values at a few dB/cm that are relatively independent of wavelength over the range of 2 to 3.8 μm. The lowest loss was measured to be 2.5 dB/cm at 3.8 μm in a Ge-on-Si waveguide designed to have an etch depth of 1.2 μm and a core width of 2.25 μm.

In Chapter 5, nonlinear transmission properties of a-Si:H core fibres were characterized from the near infrared up to the edge of the mid-IR regime. The results revealed that the two-photo absorption (TPA) coefficient β_{TPA} drops sharply from 0.70 cm/GW at 1.5 μm down to a negligible value of 0.05 cm/GW as the wavelength approaches the mid-IR regime (1.95 - 2.15 μm). The values of the Kerr coefficient n_2 were also estimated by studying the spectral broadening induced by self-phase modulation (SPM) over this wavelength range. The results have shown that n_2 reaches a peak value at 1.75 μm which is estimated to be the TPA edge of the a-Si:H material. All of the n_2 values stay in the range of $1.2 - 1.75 \times 10^{-13}\,\mathrm{cm}^2/\mathrm{W}$, which is in the upper range compared to other a-Si:H and c-Si platform. By measuring the dispersion of the nonlinear Kerr and TPA parameters I have found that the nonlinear figure of merit ($\mathrm{FOM_{NL}}$) increases

dramatically over this region, with $FOM_{NL} > 20$ at around 2 μm and above. This characterization demonstrates the potential for a-Si:H core fibres to find use in nonlinear applications in the mid-IR regime.

The superior nonlinear properties of the a-Si:H core fibres were exploited to demonstrate the supercontinuum generation. A a-Si:H core fibre, with 1.7 μm core diameter, was used to demonstrate a broadband supercontinuum that extends from the edge of the telecommunications band into the mid-IR (1.64 to 3.37 μm). The supercontinuum was seeded by cascaded four-wave mixing (FWM) and subsequent pulse break-up.

In Chapter 5, TPA in a Ge-on-Si waveguide was characterised for the first time for a range of wavelengths across the wavelength range (2 - 3.8 μm). The results show that the TPA parameters in germanium waveguides are much stronger than the peak values in silicon, which is in good agreement with selected measurements conducted in bulk materials. The Ge-on-Si waveguide exhibited a relatively long carrier lifetime $\tau \sim 18$ ns, although it is still faster than what has been measured for silicon waveguides with similar micron sized core dimensions. As the carrier lifetime is related to the waveguide dimensions, it could be reduced by scaling down the waveguide size. All-optical modulation has been demonstrated using the FCA for over the mid-IR wavelength range of 2 to 3.2 μm, with extinctions up to 5 dB. The speed of this modulation scheme was limited by the slow carrier lifetime. However, by exploiting the high TPA parameter directly, a high-speed (picosecond) TPA-based cross-absorption modulation (XAM) scheme was demonstrated, obtaining a modulation extinction ratio of 8 dB for only 10 W coupled peak power. These results present the first step toward the design and development of nonlinear optical devices in germanium-based waveguides for applications across the increasingly important mid-IR regime.

7.2 Future work

Mid-IR photonics is still an emerging field with numerous exciting possibilities existing for future studies. Possible future work could go in two directions, (i) completing the knowledge of characterisation of the optical properties of silicon and germanium in the mid-IR regime, and (ii) exploiting novel applications based on the semiconductor waveguides. Several examples of the possible future research work are listed here.

1. Dispersion engineering in silicon core fibre. The accurate dispersion properties of the silicon optical fibre is yet to know. Hence, measuring the dispersion properties of the silicon optical fibres will provide the key parameters necessary for a range of applications such as pulse shaping. Better understanding of the dispersion properties will also be useful for a more accurate analysis of supercontinuum generation introduced in Chapter 6. Furthermore, the silicon fibre platform can capitalise off

the broad array of existing silica optical fibres hence introduce the hollow core photonic crystal fibre (PCF). Using these as templates for deposition, this approach will provide us the capabilities allow for dispersion engineering beyongd what is possible with step index fibres. Some preliminary work has been conducted to fabricate silicon PCFs which exhibited novel optical properties. I anticipate that by making use of the PCF designs it should be possible not only to observe, but also to optimize the full range of nonlinear optical effects in silicon optical fibres.

2. Nonlinear photonics in germanium. Germanium is a promising material choice for the mid-IR. However, many of its optical properties especially nonlinearities are not yet well known. The work in this thesis presented the first systemic measurements of the nonlinear absorption in Ge-on-Si waveguides. Now characterisations of the Kerr nonlinear coefficient n_2 are required to obtain a comprehensive knowledge of the fundamental nonlinear properties.

3. Exploiting even longer wavelengths in the mid-IR regime. In this work, the investigations are conducted in the wavelength range from the near infrared up to $3.8\,\mu$m which is just past the short wavelength edge of the mid-IR regime. Although there are some reports for germanium waveguides of even longer wavelengths around $5\,\mu$m, there is still a very broad unexploited spectral regime, including the 8 to $14\,\mu$m "finger regime" which is of particular importance for biomedical applications. To access these longer wavelength parts of the mid-IR waveguide I will have to design novel waveguide structures or incorporate new materials as silicon is lossy beyond $8\,\mu$m. For example, suspended germanium or germanium on chalcogenide platforms could allow the transmission window to extend over the wavelength range from 2 to $14\,\mu$m.

These further investigations will update our understanding of the basic optical properties of these two mid-IR waveguide platforms. By putting continuous efforts in optimising the waveguide fabrication process and exploiting novel waveguide designs, I anticipate that potential mid-IR photonic devices could built on these semiconductor waveguides in the future.

Appendix A

List of publications

Journal Papers

1. J. J. Ackert, D. J. Thomson, **L. Shen**, A. C. Peacock, P. E. Jessop, G. T. Reed, G. Z. Mashanovich, and A. P. Knights, "High-speed detection above the telecommunication windows with monolithic silicon photodiodes", *Nature Photonics*, Vol.9 393-396(2015).

2. M, Belal, L, Xu, P, Horak, **L. Shen**, X. Feng, M. Ettabib, D. J. Richardson, and J. H. V. Price, "Mid-infrared supercontinuum generation in suspended core tellurite microstructured optical fibers", *Optics Letters*, Vol.40 (10), 2237-2240(2015).

3. **L. Shen**, N. Healy, C. J. Mitchell, J. S. Penades, M. Nedeljkovic, G. Z. Mashanovich, A. C. Peacock, "Two-photon absorption and all-optical modulation in germanium-on-silicon waveguides for the mid-infrared", *Optics Letters*, Vol.40 (10), 2213-2216(2015).

4. **L. Shen**, N. Healy, C. J. Mitchell, J. S. Penades, M. Nedeljkovic, G. Z. Mashanovich, A. C. Peacock, "Mid-infrared all-optical modulation in low loss germanium-on-silicon waveguides", *Optics Letters*, Vol.40 (2), 268-271(2015).

5. G. Roelkens, U. D. Dave, A. Gassenq, N. Hattasan, C. Hu, B. Kuyken, F. Leo, A. Malik, M. Muneeb, E. Ryckeboer, D. Sanchez, S. Uvin, R. Wang, Z. Hens, R. Baets, Y. Shimura, F. Gencarelli, B. Vincent, R. Loo, J. Van Campenhout, L. Cerutti, J-B. Rodriguez, E. Tournie, X. Chen, M. Nedeljkovic, G. Mashanovich, **L. Shen**, N. Healy, A. C. Peacock, R. Osgood, W. M. J. Green, "Silicon-Based Photonic Integration Beyond the Telecommunication Wavelength Range", *IEEE Journal of Selected Topics in Quantum Electronics*, Vol.20 (4), 1-11(2014).

6. D. J. Thomson, **L. Shen**, J. J. Ackert, E. Huante-Ceron, A. P. Knights, M. Nedeljkovic, A. C. Peacock, G. Z. Mashanovich, "Optical detection and modulation at 2 μm-2.5 μm in silicon", *Optics Express*, Vol.22 (9), 10825-10830(2014).

7. L. Xu, J. S. Feehan, **L. Shen**, A. C. Peacock, D. P. Shepherd, D. J. Richardson, J. HV. Price, "Yb-fiber amplifier pumped idler-resonant PPLN optical parametric oscillator producing 90 femtosecond pulses with high beam quality", *Applied Physics B*, Vol.117 (4), 987-993(2014).

8. **L. Shen**, N. Healy, H. Y. Cheng, T. D. Day, J. HV. Price, J. V. Badding, A. C. Peacock, "Four-wave mixing and octave-spanning supercontinuum generation in a small core hydrogenated amorphous silicon fiber pumped in the mid-infrared", *Optics Letters*, Vol.19 (19), 5721-5724(2014).

9. G. Roelkens, U. D. Dave, A. Gassenq, N. Hattasan, C. Hu, B. Kuyken, F. Leo, A. Malik, M. Muneeb, E. Ryckeboer, D. Sanchez, S. Uvin, R. Wang, Z. Hens, R. Baets, Y. Shimura, F. Gencarelli, B. Vincent, R. Loo, J. Van Campenhout, L. Cerutti, J-B. Rodriguez, E. Tournie, X. Chen, M. Nedeljkovic, G. Mashanovich, **L. Shen**, N. Healy, A. C. Peacock, R. Osgood, W. M. J. Green, "Silicon-based heterogeneous photonic integrated circuits for the mid-infrared", *Optical Materials Express*, Vol.3 (9), 1523-1536(2014).

10. **L. Shen**, N. Healy, P. Metha, T. D. Day, J. R. Sparks, J. V. Badding, A. C. Peacock, "Nonlinear transmission properties of hydrogenated amorphous silicon core fibers towards the mid-infrared regime", *Optics Express*, Vol.21 (11), 13075-13083(2013).

Conference Papers

1. S.Chaudhuri, **L. Shen**, N. Healy, A. C. Peacock, J. V. Badding, "Hydrogenated amorphous germanium optical fiber", *Advanced Photonics Conference*, Boston United States, 27 June-1 July (2015).

2. H. Zhang, N. Healy, **L. Shen**, C. C. Huang, D. Hewak, and A. C. Peacock, "High-performance Low-loss Fibre Polarizer Based on Graphene and PVB", *CLEO/Europe-EQEC*, Munich Germany, CH-6.5, 21-25 June (2015).

3. **L. Shen**, N. Healy, C. J. Mitchell, J. S. Penades, M. Nedeljkovic, G. Z. Mashanovich, and A. C. Peacock, "All-optical Modulation in Germanium-on-silicon Waveguides in the Mid-infrared", *CLEO/QELS*, San Jose United States, STu4I.7, 10-15 May (2015).

4. **L. Shen**, N. Healy, C. J. Mitchell, J. S. Penades, M. Nedeljkovic, G. Z. Mashanovich, A. C. Peacock, "All-optical modulation and nonlinear absorption in germanium-on-silicon waveguides near the $2\,\mu$m wavelength regime", *Asia Communications and Photonics Conference*, Shanghai China, ATh4B.6, 11-14 Nov (2014).

5. A. C. Peacock, **L. Shen**, P. Metha, N. Healy, "Nonlinear properties of silicon optical fibers from telecoms to the mid-infrared", *Frontiers in Optics/Laser Science (FiO)*, Tuscon United States, FW1D.5 (Invited), 19-23 Oct (2014).

6. G. Roelkens, U. D. Dave, A. Gassenq, N. Hattasan, C. Hu, B. Kuyken, F. Leo, A. Malik, M. Muneeb, E. Ryckeboer, D. Sanchez, S. Uvin, R. Wang, Z. Hens, R. Baets, Y. Shimura, F. Gencarelli, B. Vincent, R. Loo, J. Van Campenhout, L. Cerutti, J-B. Rodriguez, E. Tournie, X. Chen, M. Nedeljkovic, G. Mashanovich, **L. Shen**, N. Healy, A. C. Peacock, R. Osgood, W. M. J. Green, "Long-wavelength silicon photonic integrated circuits", *IEEE 11th International Conference on Group IV Photonics (GFP)*, Paris France, WD1, 27-29 Aug(2014).

7. **L. Shen**, N. Healy, H. Y. Cheng, T. D. Day, J. V. Badding, A. C. Peacock, "Short-wave infrared continuum generation in hydrogenated amorphous silicon fibers", *OSA Advanced Photonics Congress (SOF)*, Barcelona Spain, JTu3A.14, 27-31 Jul (2014).

8. A. C. Peacock, P. Metha, **L. Shen**, F. H. Suhailin, N. Vukovic, N. Healy, "Silicon fibre devices for nonlinear applications", *OECC/ACOFT '14*, Melbourne Australia, WE7B (Invited), 6-10 Jul (2014).

9. **L. Shen**, N. Healy, H. Y. Cheng, T. D. Day, J. V. Badding, A. C. Peacock, "Semiconductor optical fibres for nonlinear applications in the mid-infrared", *Rank Prize Funds Symposium: New Horizons in Non-linear Fibre Optics*, Grasmere United Kingdom, 6-10 Jun (2014).

10. G. Roelkens, U. D. Dave, A. Gassenq, N. Hattasan, C. Hu, B. Kuyken, F. Leo, A. Malik, M. Muneeb, E. Ryckeboer, D. Sanchez, S. Uvin, R. Wang, Z. Hens, R. Baets, Y. Shimura, F. Gencarelli, B. Vincent, R. Loo, J. Van Campenhout, L. Cerutti, J-B. Rodriguez, E. Tournie, X. Chen, M. Nedeljkovic, G. Mashanovich, **L. Shen**, N. Healy, A. C. Peacock, R. Osgood, W. M. J. Green, "Mid-IR heterogeneous silicon photonics ", *SPIE Photonics West*, San Francisco United States, 8993-42 (Invited), 1-6 Feb(2014).

11. N. Healy, P. J. Sazio, P. Metha, **L. Shen**, T. D. Day, J. V. Badding, A. C. Peacock, "Towards in-fiber silicon photonics", *Asia Communications and Photonics Conference*, Shanghai China, ATh3C.1 (Invited), 12 Nov (2013).

12. **L. Shen**, N. Healy, T. D. Day, J. V. Badding, A. C. Peacock, "High nonlinear figure of merit hydrogenated amorphous silicon optical fibers", *Workshop on Speciality Optical Fibers and their Applications (WSOF 2013)*, Sigtuna Sweden, 28-30 Aug (2013).

13. A. C. Peacock, P. Metha, **L. Shen**, T. D. Day, J. R. Sparks, J. V. Badding, N. Healy, "Nonlinear properties of silicon optical fibers from telecoms to the mid-infrared", *Photonics North*, Ottawa Canada, (Invited), 3-5 Jun (2013).

14. **L. Shen**, N. Healy, T. D. Day, J. R. Spark, J. V. Badding, A. C. Peacock, "Two-Photon Absorption and Self-PhaseModulation in Silicon Optical Fibers into the Mid-Infrared Regime", *POEM/IONT*, Wuhan China, IF2A.2, 1-2 Nov (2012).

15. **L. Shen**, N. Healy, P. Metha, T. D. Day, J. R. Spark, J. V. Badding, A. C. Peacock, "Transmission properties of hydrogenated amorphous silicon optical fibers into the mid-infrared regime", *Frontiers in Optics (FiO/LS XXVIII)*, Rochester United States, FM3H.3, 14-18 Oct (2012).

References

[1] E. Suhir, "Microelectronics and photonics-the future," *Microelectronics Journal* vol. 31, no. 11-12 pp.839–851, 2000.

[2] R. Soref and B. Bennett, "Electrooptical effects in silicon," *IEEE Journal of Quantum Electronics* vol. 23, no. 1 pp.123–129, 1987.

[3] B. Schuppert, J. Schmidtchen, and K. Petermann, "Optical channel waveguides in silicon diffused from GeSi alloy," *Electronics Letters* vol. 25, no. 22 pp.1500–1502, 1989.

[4] R. Soref, J. Schmidtchen, and K. Petermann, "Large single-mode rib waveguides in GeSi-Si and Si-on-SiO_2," *IEEE Journal of Quantum Electronics* vol. 27, no. 22 pp.1971–1974, 1991.

[5] B. Jalali and S. Fathpour, "Silicon photonics," *Journal of Lightwave Technology* vol. 24, no. 25 pp.4600–4615, 2006.

[6] G. T. Reed, G. Z. Mashanovich, F. Y. Gardes, and D. J. Thomson, "Silicon optical modulators," *Nature Photonics* vol. 4, no. 8, pp.518–526, 2010.

[7] B. Jalali, V.Raghunathan, R. Shori, S. Fathpour, D. Dimitropoulos, and O. Stafsudd, "Prospects for Silicon Mid-IR Raman Lasers," *IEEE Journal of Selected Topics in Quantum Electronics* vol. 12, no. 6, pp.1618–1627, 2006.

[8] R. Soref, Towards silicon-based longwave integrated optoelectronics (LIO)," *Proc. SPIE* vol. 6898, pp. 689809, 2008.

[9] G. Z. Mashanovich, M. M. Milosevic, M. Nedeljkovic, N. Owens, W. R. Headley, E. J. Teo, B. Xiong, P. Yang, and Y. Hu, "Low loss silicon waveguides for the mid-infrared," *Optics Express* vol. 19, no. 8, pp.7112–7119, 2011.

[10] B. Kuyken, T. Ideguchi, S. Holzner, M. Yan, T. W. H́ansch, J. Van Campenhout, P. Verheyen, S. Coen, F. Leo, R. Baets, G. Roelkens and N. Picqué, "An octave-spanning mid-infrared frequency comb generated in a silicon nanophotonic wire waveguide," *Nature Communications* vol. 6, pp.1–6, 2015.

[11] M. N. Petrovich, F. Poletti, J. P. Wooler, A. Heidt, N. Baddela, Z. Li, D. Gray, R. Slavk, F. Parmigiani, N. Wheeler, J. Hayes, E. Numkam, L. Grüner-Nielsen, B. Pálsdóttir, R. Phelan, B. Kelly, J. O'Carroll, M. Becker, N. MacSuibhne, J. Zhao, F. G. Gunning, A. Ellis, P. Petropoulos, S. Alam, and D. J. Richardson, "Demonstration of amplified data transmission at 2 μm in a low-loss wide bandwidth hollow core photonic bandgap fiber," *Optics Express* vol. 21, no. 23, pp.28559–28569, 2013.

[12] T. Baehr-Jones, A. Spott, R. Ilic, A. Spott, B. Penkov, W. Asher, and M. Hochberg, "Silicon-on-sapphire integrated waveguides for the mid-infrared," *Optics Express* vol. 18, no. 12, pp. 12127–12135, 2010.

[13] Y. C. Chang, V. Paeder, L. Hvozdara, J. M. Hartmann, and H. P. Herzig, "Low-loss germanium strip waveguides on silicon for the mid-infrared," *Optics Letters* vol. 37, no. 14, pp.2883–2885, 2012.

[14] R. A. Soref, "Mid-infrared photonics in silicon and germanium," *Nature Photonics* vol. 4, pp.495–497, 2010.

[15] J. Leuthold, C. Koos, and W. Freude, "Nonlinear silicon photonics," *Nature Photonics* vol. 4, pp.535–544, 2010.

[16] B. J. Frey, D. B. Leviton, and T. J. Madison, " Temperature-dependent refractive index of silicon and germanium," *Optomechanical Technologies for Astronomy, Pts 1 and 2*, vol. 6273, pp. J2732-J2732 1178, 2006.

[17] N. P. Barnes and M. S. Piltch, "Temperature-dependent sellmeier coefficients and non-linear optics average power limit for germanium," *Journal of the Optical Society of America*, vol. 69, no. 1, pp. 178–180, 1979.

[18] R. Claps, D. Dimitropoulos, V. Raghunathan, Y. Han, and B. Jalali, "Observation of stimulated Raman amplification in silicon waveguides," *Optics Express* vol. 11, no. 15, pp. 1731–1739, 2003.

[19] I.-W. Hsieh, X. Chen, X. Liu, J. I. Dadap, N. C. Panoiu, C.-Y. Chou, F. Xia, W. M. Green, Y. A. Vlasov, and R. M. Osgood, "Supercontinuum generation in silicon photonic wires," *Optics Express* vol. 15, no. 20, pp.15242–15249, 2007.

[20] K. Yamada, H. Fukuda, T. Tsuchizawa, T. Watanabe, T. Shoji, and S. Itabashi, "All-optical efficient wavelength conversion using silicon photonic wire waveguide," *IEEE Photonics Technology Letters* vol. 18, no. 9, pp.1046–1048, 2006.

[21] M. A. Foster, A. C. Turner, J. E. Sharping, B. S. Schmidt, M. Lipson, and A. L. Gaeta, "Broad-band optical parametric gain on a silicon photonic chip," *Nature* vol. 441, pp.960–930, 2006.

[22] A. C. Peacock, J. R. Sparks and N. Healy, "Semiconductor optical fibres: progress and opportunities," *Laser & Photonics Reviews* vol. 8, no. 1, pp.53–72, 2014.

[23] K. Narayanan and S. F. Preble, "Optical nonlinearities in hydrogenated-amorphous silicon waveguides," *Optics Express* vol. 18, no. 9, pp. 8998–9005, 2010.

[24] J. I. Pankove, and D. E. Carlason, "Electrical and optical properties of hydragenated amorphous silicon," *Annual Review of Materials Science* vol. 10, pp.43–63, 1980.

[25] K. Narayanan, A. W. Elshaari, and S. F. Preble, "Broadband all-optical modulation in hydrogenated-amorphous silicon waveguides," *Optics Express* vol. 18, no. 10, pp. 9809–9814, 2010.

[26] Y. Shoji, T. Ogasawara, T. Kamei, Y. Sakakibara, S. Suda, K. Kintaka, H. Kawashima, M. Okano, T. Hasama, H. Ishikawa, and M. Mori, "Ultrafast nonlinear effects in hydrogenated amorphous silicon wire waveguide," *Optics Express* vol. 18, no. 6, pp. 5668–5673, 2010.

[27] B. Kuyken, S. Clemmen, S. K. Selvaraja, W. Bogaerts, D. Van Thourhout, Ph. Emplit, S. Massar, G. Roelkens, and R. Baets, "On-chip parametric amplification with 26.5 dB gain at telecommunication wavelengths using CMOS-compatible hydrogenated amorphous silicon waveguides," *Optics Letters* vol. 36, no. 4, pp.552–554, 2011.

[28] P. Mehta, N. Healy, T. D. Day, J. V. Badding, and A. C. Peacock, "Ultrafast wavelength conversion via cross-phase modulation in hydrogenated amorphous silicon optical fibers," *Optics Express* vol. 20, no. 24, pp. 26110–26116, 2012.

[29] N. Hon, R. Soref, and B. Jalali, "The third-order nonlinear optical coefficients of Si, Ge, and $Si_{1-x}Ge_x$ in the midwave and longwave infrared," *Journal of Applied Physics* vol. 110, no. 1, pp. 011301, 2011.

[30] P. J. A. Sazio, A. Amezcua-Correa, C. E. Finlayson, J. R. Hayes, T. J. Scheidemantel, N. F. Baril, B. R. Jackson, D.-J. Won, F. Zhang, E. R. Margine, V. Gopalan, and V. H. Crespi, J. V. Badding, "Microstructured Optical Fibers as High-Pressure Microfluidic Reactors," *Science* vol. 311, no. 5767, pp.1583–1586, 2006.

[31] C. E. Finlayson, A. Amezcua-Correa, P. J. A. Sazio, N. F. Baril and J. V. Badding, "Electrical and Raman characterization of silicon and germanium-filled microstructured optical fibers," *Applied Physics Letters* vol. 90, no. 13, pp.132110, 2007.

[32] J. R. Sparks, R. He, N. Healy, M. Krishnamurthi, A. C. Peacock, P. J. A. Sazio, V. Gopalan, and J. V. Badding, "Zinc Selenide Optical Fibers," *Advanced Materials* vol. 23, no. 14, pp.1647–1651, 2011.

[33] N. Healy, J. R. Sparks, R. R. He, P. J. A. Sazio, J. V. Badding, and A. C. Peacock, "High index contrast semiconductor ARROW and hybrid ARROW fibers," *Optics Express* vol. 19, no. 11, pp.10979–10985, 2011.

[34] J. Ballato, T. Hawkins, P. Foy, R. Stolen, B. Kokuoz, M. Ellison, C. McMillen, J. Reppert, A. M. Rao, M. Daw, S. Sharma, R. Shori, O. Stafsudd, R. R. Rice, and D. R. Powers, "Silicon optical fiber," *Optics Express* vol. 16, no. 23, pp.18675–18683, 2008.

[35] J. Ballato, T. Hawkins, P. Foy, B. Yazgan-Kokuoz, R. Stolen, C. McMillen, N. K. Hon, B. Jalali, and R. Rice, "Glass-clad single-crystal germanium optical fiber," *Optics Express* vol. 17, no. 10, pp.8029–8035, 2009.

[36] J. Ballato, T. Hawkins, P. Foy, B. Yazgan-Kokuoz, C. McMillen, L. Burka, S. Morris, R. Stolen, and R. Rice, "Advancements in semiconductor core optical fiber," *Optical Fiber Technology* vol. 16, no. 6, pp.399–408, 2010.

[37] J. Ballato, T. Hawkins, P. Foy, S. Morris, N. K. Hon, B. Jalali, and R. Rice, "Silica-clad crystalline germanium core optical fibers," *Optics Letters* vol. 36, no. 5, pp.687–688, 2011.

[38] S. Morris, T. Hawkins, P. Foy, C. McMillen, J. Fan, L. Zhu, R. Stolen, R. Rice, and J. Ballato, "Reactive molten core fabrication of silicon optical fiber," *Optical Materials Express* vol. 1, no. 6, pp.1141–1149, 2011.

[39] S. Morris, S. W. Martin, T. Hawkins, P. Foy, R. Rice, and J. Ballato, "Cladding Glass Development for Semiconductor Core Optical Fibers," *International Journal of Applied Glass Science* vol. 3, no. 2, pp.144–153, 2012.

[40] E. F. Nordstrand, A. N. Dibbs, J. Eraker and U. J. Gibson, "Alkaline oxide interface modifiers for silicon fiber production," *Optical Materials Express* vol. 3, no. 5, pp.651–657, 2013.

[41] H. K. Tyagi, M. A. Schmidt, L. Prill Sempere, and P. St.J. Russell, "Optical properties of photonic crystal fiber with integral micron-sized Ge wire," *Optics Express* vol. 16, no. 22, pp.17227–17236, 2008.

[42] B. Scott, K. Wang, V. Caluori, and G. Pickrell, "Fabrication of silicon optical fiber," *Optical Engineering* vol. 48, no. 10, pp.10050, 2009.

[43] B. Scott, K. Wang, and G. Pickrell, "Fabrication of n-Type Silicon Optical Fibers," *IEEE Photonics Technology Letters* vol. 21, no. 24, pp.1798–1800, 2009.

[44] A. M. Stolyarov, L. Wei, O. Shapira, F. Sorin, S. L. Chua, J. D. Joannopoulos, and Y. Fink, "Microfluidic directional emission control of an azimuthally polarized radial fibre laser," *Nature Photonics* vol. 6, pp.229–233, 2012.

[45] A. F. Abouraddy, M. Bayindir, G. Benoit, S. D. Hart, K. Kuriki, N. D. Orf, O. Shapira, F. Sorin, B. Temelkuran, and Y. Fink, "Towards multimaterial multifunctional fibres that see, hear, sense and communicate," *Nature Materials* vol. 6, pp.336–347, 2007.

[46] M. Bayindir, A. F. Abouraddy, J. Arnold, J. D. Joannopoulos, and Y. Fink, "Thermal-Sensing Fiber Devices by Multimaterial Codrawing," *Advanced Materials* vol. 18, no. 7, pp.845–849, 2006.

[47] S. Egusa, Z. Wang, N. Chocat, Z. M. Ruff, A. M. Stolyarov, D. Shemuly, F. Sorin, P. T. Rakich, J. D. Joannopoulos, and Y. Fink, "Multimaterial piezoelectric fibres," *Nature Materials* vol. 9, pp.643–648, 2010.

[48] B. Temelkuran, S. D. Hart, G. Benoit, J. D. Joannopoulos, and Y. Fink, "Wavelength-scalable hollow optical fibres with large photonic bandgaps for CO_2 laser transmission," *Nature* vol. 420, pp.650–653, 2002.

[49] C. Hou, X. Jia, L. Wei, S. Tan, J. D. Joannopoulos, and Y. Fink, "Crystalline silicon core fibres from aluminium core preforms," *Nature Communications* vol. 6, pp.1–6, 2015.

[50] P. Mehta, N. Healy, T. D. Day, P. J. Sazio, J. V. Badding, and A. C. Peacock, "Effect of core size on nonlinear transmission in silicon core optical fibers," *CLEO/QELS* San Jose, CTh1C.2, 6-11 May, 2012.

[51] J. Ballato, T. Hawkins, P. Foy, S. Morris, N. K. Hon, B. Jalali, and R. Rice, "Silica-clad crystalline germanium core optical fibers," *Optics Letters* vol. 36, no. 5, pp.687–688, 2011.

[52] S. K. Selvaraja, W. Bogaerts, P. Absil, D. V. Thourhout, and R. Baets, "Record low-loss hybrid rib/wire waveguides for silicon photonic circuits," *Group IV Photonics proceedings* Beijing, China, 2010.

[53] W. Bogaerts, G. Roelkens, and L. Liu, *Technologies and Building Blocks for On-Chip Optical Interconnects in Integrated Optical Interconnect Architectures for Embedded Systems* vol. 12 Springer, 2013.

[54] L. Vivien, J. Osmond, J. Fédéli, D. Marris-Morini, P. Crozat, J. Damlencourt, E. Cassan, Y. Lecunff, and S. Laval, "42 GHz p.i.n Germanium photodetector integrated in a silicon-on-insulator waveguide," *Optics Express* vol. 17, no. 8, pp. 6252–6257, 2009.

[55] M. Dinu, F. Quochi, and H. Garcia, " Third-order nonlinearities in silicon at telecom wavelengths," *Applied Physics Letters* vol. 82, no. 25 pp.2954–2956, 2003.

[56] H. K. Tsang, C. S. Wong, T. K. Liang, I. E. Day, S. W. Roberts, A. Harpin, J. Drake, and M. Asghari, "Optical dispersion, two-photon absorption and selfphase

modulation in silicon waveguides at 1.5 μm wavelength," *Applied Physics Letters* vol. 80, no. 3, pp.416–418, 2002.

[57] L. H. Yin, Q. Lin, and G. P. Agrawal, "Soliton fission and supercontinuum generation in silicon waveguides," *Optics Letters* vol. 32, no. 4, pp. 391–393, 2007.

[58] P. Koonath, D. R. Solli, and B. Jalali, " Continuum generation and carving on a silicon chip," *Applied Physics Letters* vol. 91, no. 6 pp.061111, 2007.

[59] G. W. Rieger, K. S. Virk, and J. F. Young, " Nonlinear propagation of ultrafast 1.5 μm pulses in high-index-contrast silicon-on-insulator waveguides," *Applied Physics Letters* vol. 84, no. 6 pp.900-902, 2004.

[60] Ozdal Boyraz, P. Koonath, V. Raghunathan, and B. Jalali, "All optical switching and continuum generation in silicon waveguides," *Optics Express* vol. 12, no. 18, pp.4094–4102, 2004.

[61] W. Astar, J. B. Driscoll, X. Liu, J. I. Dadap, W. M. J. Green, Y. A. Vlasov, G. M. Carter, and R. M. Osgood, " Conversion of 10 Gb/s NRZ – OOK to RZ – OOK utilizing XPM in a Si nanowire," *Optics Express* vol. 17, no. 10, pp.12987–12999, 2009.

[62] C. Koos, P. Vorreau, T. Vallaitis, P. Dumon, W. Bogaerts, R. Baets, B. Esembeson, I. Biaggio, T. Michinobu, F. Diederich, W. Freude, and J. Leuthold, "All-optical highspeed signal processing with silicon organic hybrid slot waveguides," *Nature Photonics* vol. 3, no. 4, pp.216–219, 2009.

[63] M. A. Foster, A. C. Turner, J. E. Sharping, B. S. Schmidt, M. Lipson, and A. L. Gaeta, "Broad-band optical parametric gain on a silicon photonic chip," *Nature* vol. 441, pp.960–930, 2006.

[64] X. Liu, R. M. Osgood, Y. A. Vlasov, and W. M. J. Green, "Mid-infrared optical parametric amplifier using silicon nanophotonic waveguides," *Nature Photonics* vol. 4, pp.557–560, 2010.

[65] R. Salem, M. A. Foster, A. C. Turner, D. F. Geraghty, M. Lipson and A. L. Gaeta, "Signal regeneration using low-power four-wave mixing on silicon chip," *Nature Photonics* vol. 2, pp.35–38, 2008.

[66] R. A. Soref, "Mid-infrared photonics in silicon and germanium," *Nature Photonics* vol. 4, pp.495–497, 2010.

[67] G. Z. Mashanovich, M. M. Milošević, M. Nedeljkovic, N. Owens, B. Xiong, E.-J. Teo, and Y. Hu, "Low loss silicon waveguides for the mid-infrared," *Optics Express* vol. 19, no. 8, pp. 7112–7119, 2011.

[68] M. M. Milošević, D. J. Thomson, X. Chen, D. Cox, and G. Z. Mashanovich, "Silicon waveguides for the $3-4\,\mu$m wavelength range," *Group IV Photonics proceedings* New York, United States, pp. 208210, 2011.

[69] F. Li, S. D. Jackson, C. Grillet, E. Magi, D. Hudson, S. J. Madden, Y. Moghe, C. O'Brien, A. Read, S. G. Duvall, P. Atanackovic, B. J. Eggleton, and D. J. Moss, "Low propagation loss silicon-on-sapphire waveguides for the mid-infrared," *Optics Express* vol. 19, no. 6, pp.15212-15220, 2011.

[70] A. Spott, Y. Liu, T. Baehr-Jones, R. Ilic, and M. Hochberg, "Silicon waveguides and ring resonators at $5.5\,\mu$m," *Applied Physics Letters* vol. 97, no. 21, pp. 213501, 2010.

[71] L. Pacesi, "Porous silicon dielectric multilayers and microcavities," *La Rivista del Nuovo Cimento* vol. 20, no. 10, pp. 1–76, 1997.

[72] Z. Cheng, X. Chen, C. Y. Wong, K. Xu, C. K. Fung, Y. M. Chen, and H. K. Tsang, "Focusing subwavelength grating coupler for mid-infrared suspended membrane waveguide," *Optics Letters* vol. 37, no. 7, pp.1217–1219, 2012.

[73] P. T. Lin, V. Singh, Y. Cai, L. C. Kimerling, and A. Agarwal, "Air-clad silicon pedestal structures for broadband mid-infrared microphotonics," *Optics Letters* vol. 38, no. 7, pp.1031–1033, 2013.

[74] J. Soler Penades, C. Alonso-Ramos, A. Z. Khokhar, M. Nedeljkovic, L. A. Boodhoo, A. Ortega-Monux, I. Molina-Fernandez, P. Cheben, and G. Z. Mashanovich, "Suspended SOI waveguide with sub-wavelength grating cladding for mid-infrared," *Optics Letters* vol. 39, no. 19, pp.5661–2482, 2014.

[75] R. A. Soref, S. J. Emelett, and W. R. Buchwald, "Silicon waveguided components for the long-wave infrared region," *Journal of Optics A: Pure and Applied Optics* vol. 8, no. 10, pp.840–848, 2006.

[76] A. Malik, M. Muneeb, Y. Shimura, J. Van Campenhout, R. Loo, and G. Roelkens, "Germanium-on-Silicon Mid-Infrared Arrayed Waveguide Grating Multiplexers," *IEEE Photonics Technology Letters* vol. 25, no. 18, pp.1805–1808, 2013.

[77] Y. C. Chang, P. Wägli, V. Paeder, A. Homsy, L. Hvozdara, P. van der Wal, J. Di Francesco, N. F. de Rooij, and H. P. Herzig, "Cocaine detection by a mid-infrared waveguide integrated with a microfluidic chip," *Lab on a Chip* vol. 12, pp.3020-3023, 2012.

[78] A. Malik, M. Muneeb, Y. Shimura, J. Van Campenhout, R. Loo, and G. Roelkens, "Germanium-on-silicon planar concave grating wavelength (de)multiplexers in the mid-infrared," *Applied Physics Letters* vol. 103, no. 16, pp. 161119, 2013.

[79] V. Raghunathan, D. Borlaug, R. R. Rice, and B. Jalali, "Demonstration of a Mid-infrared silicon Raman amplifier," *Optics Express* vol. 15, no. 22, pp.14355–14362, 2007.

[80] S. Zlatanovic, J. S. Park, S. Moro, J. M. C. Boggio, I. B. Divliansky, N. Alic, S. Mookherjea, and S. Radic, "Mid-infrared wavelength conversion in silicon waveguides using ultracompact telecom-band-derived pump source," *Nature Photonics* vol. 4, no. 8, pp. 561–564, 2010.

[81] B. Kuyken, X. Liu, R. M. Osgood Jr., R. Baets, G. Roelkens, and W. M. J. Green, "Mid-infrared to telecom-band supercontinuum generation in highly nonlinear silicon-on-insulator wire waveguides," *Optics Express* vol. 19, no. 21, pp. 20172–20181, 2011.

[82] B. V. Zubov, L. A. Kulevskii, V. P. Makarov, T. M. Murina and A. M. Prokhorov, "Two-photon Absorption in Germanium," *JETP Letters* vol 9, no. 4, pp. 130–132, 1969.

[83] A. F. Gibson, C. B. Hatch, P. N. D. Maggs, D. R. Tilley and A. C. Walker, "Two-photon absorption in indium antimonide and germanium," *Journal of Physics C: Solid State Physics* vol 9, no. 17, pp. 3259–3275, 1976.

[84] C. Rauscher, and R. Laenen, "Analysis of picosecond mid-infrared pulses by two-photon absorption in germanium," *Journal of Applied Physics* vol 81, no. 6, pp. 2818–2821, 1997.

[85] K. Okamoto, *Fundamentals of Optical Waveguides* Academic Press, 2000.

[86] D. Gloge, *Weekly Guiding Fibres*, vol. 16 of *Applied Optics*. 1971.

[87] G. Reed and A. Knights, *Silicon photonics* Wiley Online Library, 2008.

[88] G. Agrawal, *Nonlinear fiber optics*, Academic Press, 2000.

[89] S. O. Kasap, *Optoelectronics & Photonics: Principles & Practices (2nd Edition)* Prentice Hall, 2013.

[90] M. Nedeljkovic, *Silicon photonic modulators for the mid-infrared* (Doctoral dissertation), 2011.

[91] L. Brillouin, *Wave propagation and group velocity*, Academic Press, 1960.

[92] R. S. Quimby, *Photonics and lasers : an introduction*, Wiley-Interscience, 2006.

[93] D. F. Edwards and E. Ochoa, "Infrared refractive index of silicon," *Applied optics* vol. 19, no. 24, pp.4130–4131, 1980.

[94] H. W. Icenogle, B. C. Platt and W. L. Wolfe, "Refractive indexes and temperature coefficients of germanium and silicon," *Applied optics* vol. 15, no. 10, pp.2348–2351, 1976.

[95] R. M. Osgood Jr, N. C. Panoiu, J. I. Dadap, X. Liu, X. Chen, I-Wei. Hsieh, E. Dulkeith, W. M. J. Green, and Y. A. Vlasov, "Engineering nonlinearities in nanoscale optical systems: physics and applications in dispersion-engineered silicon nanophotonic wires," *Advances in Optics and Photonics* vol. 1, no. 1, pp.162–235, 2009.

[96] G. P. Agrawal, *Fiber-optic communication systems. Wiley series in microwave and optical engineering*, Wiley-Interscience, 2002.

[97] H. H. Li, "Refractive index of silicon and germanium and its wavelength and temperature derivatives," *Journal of Physical and Chemical Reference Data* vol. 9, no. 3, pp.561–658, 1980.

[98] J. Matres, G. C. Ballesteros, P. Gautier, J.-M. Fédéli, J. Martí, and C. J. Oton, "High nonlinear figure-of-merit amorphous silicon waveguides," *Optics Express* vol. 21, no. 4, pp.3932–3940, 2013.

[99] U. Dave, S. Uvin, B. Kuyken, S. Selvaraja, F. Leo, and G. Roelkens, "Telecom to mid-infrared spanning super-continuum generation in hydrogenated amorphous silicon waveguides using a Thulium doped fiber laser pump source," *Optics Express* vol. 21, no. 26, pp. 32032–32039, 2013.

[100] F. Leo, J. Safioui, B. Kuyken, G. Roelkens, and S.-P. Gorza, "Generation of coherent supercontinuum in a-Si:H waveguides: experiment and modeling based on measured dispersion profile," *Optics Express* vol. 22, no. 23, pp.28997–29007, 2014.

[101] R. Boyd, *Nonlinear optics* Academic Press, 2002.

[102] M. Dinu, "Dispersion of phonon-assisted nonresonant third-order nonlinearities," *IEEE Journal of Quantum Electronics* vol. 39, no. 11, pp. 1498–1503, 2003.

[103] H. Garcia and R. Kalyanaraman, "Phonon-assisted two-photon absorption in the presence of a dc-field: the nonlinear FranzKeldysh effect in indirect gap semiconductors," *Journal of Physics B* vol. 39, no. 12, pp. 2737–2746, 2006.

[104] E. Tuncel, J. L. Staehli, C. Coluzza, G. Margaritondo, J. T. McKinley, R. G. Albridge, A. V. Barnes, A. Ueda, X. Yang, and N. H. Tolk, "Free-electron laser studies of direct and indirect two-photon absorption in germanium," *Physical Review Letters* vol. 70, no.26, pp.4146–4149, 2010.

[105] M. Kira and S. W. Koch, *Semiconductor quantum optics*, Cambridge University Press, 2012.

[106] L. Yin and G. P. Agrawal, "Impact of two-photon absorption on self-phase modulation in silicon waveguides," *Optics Letters* vol. 32, no. 14, pp.2031–2033, 2007.

[107] R. Dekker, N. Usechak, M. Forst, and A. Driessen, "Ultrafast nonlinear all-optical processes in silicon-on-insulator waveguides," *Journal of Physics D-Applied Physics* vol. 40, no. 14, pp. R249–R271, 2007.

[108] Q. Lin, J. Zhang, P. M. Fauchet, and G. P. Agrawal, "Ultrabroadband parametric generation and wavelength conversion in silicon waveguides," *Optics Express* vol. 14, no. 11, pp. 4786–4799, 2006.

[109] M. Feit and J. Fleck, " Self-trapping of a laser beam in a cylindrical plasma column," *Applied Physics Letters* vol. 28, no. 3 pp.121–124, 1976.

[110] N. F. Baril, B. Keshavarzi, J. R. Sparks, M. Krishnamurthi, I. Temnykh, P. J. A. Sazio, A. C. Peacock, A. Borhan, V. Gopalan, and J. V. Badding, "High-Pressure Chemical Deposition for Void-Free Filling of Extreme Aspect Ratio Templates," *Advanced Materials* vol. 22, no. 41, pp.4605–4611, 2010.

[111] N. F. Baril, R. He, T. D. Day, J. R. Sparks, B. Keshavarzi, M. Krishnamurthi, A. Borhan, V. Gopalan, A. C. Peacock, N. Healy, P. J. A. Sazio, and J. V. Badding, "Confined High-Pressure Chemical Deposition of Hydrogenated Amorphous Silicon," *Journal of the American Chemical Society* vol. 134, no. 1, pp.19–22, 2011.

[112] J. Jang, J. Y. Oh, S. K. Kim, Y. J. Choi, S. Y. Yoon and C. O. Kim, "Electric-field-enhanced crystallization of amorphous silicon," *Nature* vol. 395, pp.481–483, 1998.

[113] V. G. Erkov, and S. F. Devyatova, "Polycrystalline-silicon LPCVD by silane pyrolysis: The effect of hydrogen injection," *Russian Microelectronics* vol. 36, no. 2, pp.120–126, 2007.

[114] L. Lagonigro, N. Healy, J. R. Sparks, N. F. Baril, P. J. A. Sazio, J. V. Badding, and A. C. Peacock, "Low loss silicon fibers for photonics applications," *Applied Physics Letters* vol. 96, pp.041105, 2010.

[115] A. Liu, H. Rong, M. Paniccia, O. Cohen, and D. Hak, "Net optical gain in a low loss silicon-on-insulator waveguide by stimulated raman scattering," *Optics Express* vol. 12, no. 18, pp.4261–4268, 2004.

[116] M. Levenson, N. Viswanathan, and R. Simpson, "Improving resolution in photolithography with a phase-shifting mask," *IEEE Transactions on Electron Devices* vol. 29, no. 12, pp.1828–1836, 1982.

[117] L. Ephrath, *Reactive ion etching* Aug. 11 1981. US Patent 4,283,249.

[118] P. J. Roberts, F. Couny, H. Sabert, B. J. Mangan, D. P. Williams, L. Farr, M. W. Mason, A. Tomlinson, T. A. Birks, J. C. Knight, and P. St. J. Russell, "Ultimate low loss of hollow-core photonic crystal fibres," *Optics Express* vol. 13, no. 1, pp. 236–244, 2005.

[119] N. Healy, J. R. Sparks, P. J. A. Sazio, J. V. Badding, and A. C. Peacock, "Tapered silicon optical fibers," *Optics Express* vol. 18, no. 8, pp.7596–7601, 2010.

[120] K. P. Yap, A. Delâge, J. Lapointe, B. Lamontagne, J. H. Schmid, P. Waldron, B. A. Syrett, and S. Janz, "Correlation of scattering Loss, sidewall roughness and waveguide width in silicon-on-insulator (SOI) ridge waveguides," *Journal of Lightwave Technology* vol. 27, no. 18, pp. 3999–4008, 2009.

[121] E. Neumann, *Single-mode fibers.* Springer-Verlag, 1988.

[122] R. G. Walker,, "Simple and accurate loss measurement technigue for semiconductor optical waveguides," *Electronics Letters* vol. 21, no. 13, pp.581–582, 1985.

[123] A. Harke, M. Krause, and J. Mueller, "Low-loss singlemode amorphous silicon waveguides," *Electronics Letters* vol. 41, no. 25, pp. 1377–1379, 2005.

[124] S. Zhu, G. Q. Lo, and D. L. Kwong, "Low-loss amorphous silicon wire waveguide for integrated photonics: effect of fabrication process and the thermal stability," *Optics Express* vol. 18, no. 24, pp. 25283–25291, 2010.

[125] M. H. Brodsky, M. Cardona, and J. J. Cuomo, "Infrared and raman-spectra of silicon-hydrogen bonds in amorphous silicon prepared by glow-discharge and sputtering," *Physical Review B* vol. 16, no. 8, pp. 3556–3571, 1977.

[126] S. K. Selvaraja, E. Sleeckx, M. Schaekers, W. Bogaerts, D. Van Thourhout, P. Dumon, and R. Baets, "Low-loss amorphous silicon-on-insulator technology for photonic integrated circuitry," *Optics Communications* vol. 282, no. 9, pp. 1767–1770, 2009.

[127] N. Healy, L. Lagonigro, J. R. Sparks, S. Boden, P. J. Sazio, J. V. Badding, and A. C. Peacock, "Polycrystalline silicon optical fibers with atomically smooth surfaces," *Optics Letters* vol. 36, no. 13, pp.2480–2482, 2011.

[128] N. Gupta, C. McMillen, R. Singh, R. Podila, A. M. Rao, T. Hawkins, P. Foy, S. Morris, R. Rice, K. F. Poole, L. Zhu, and J. Ballato, "Annealing of silicon optical fibers" *Journal of Applied Physics* vol. 110, no. 9, pp.093107, 2011.

[129] N. Healy, S. Mailis, N. M. Bulgakova, P. J. A. Sazio, T. D. Day, J. R. Sparks, H. Y. Cheng, J. V. Badding, and A. C. Peacock, "Extreme electronic bandgap modification in laser-crystallized silicon optical fibres," *Nature Materials* vol. 13, pp.1122–1127, 2014.

[130] P. Mehta, M. Krishnamurthi, N. Healy, N. F. Baril, J. R. Sparks, P. J. A. Sazio, V. Gopalan, J. V. Badding, and A. C. Peacock, "Mid-infrared transmission properties of amorphous germanium optical fibers," *Applied Physics Letters* vol. 97, no. 7, pp.071117, 2010.

[131] D. Bermejo, and M. Cardona, "Raman scattering in pure and hydrogenated amorphous germanium and silicon," *Journal of Non-Crystalline Solids* vol. 32, no. 1-3, pp.405–419, 1979.

[132] P. Mehta, N. Healy, N. F. Baril, P. J. A. Sazio, J. V. Badding, and A. C. Peacock, "Nonlinear transmission properties of hydrogenated amorphous silicon core optical fibers," *Optics Express* vol. 18, no. 16, pp. 16826–16831, 2010.

[133] www.iqesilicon.com.

[134] R. Loo, G. Wang, L. Souriau, J. C. Lin, S. Takeuchi, G. Brammertz, and M. Caymax, "High Quality Ge Virtual Substrates on Si Wafers with Standard STI Patterning," *Journal of The Electrochemical Society* vol. 157, no. 1, pp. H13–H21, 2010.

[135] G. Z. Mashanovich, M. Milosevic, P. Matavulj, S. Stankovic, B. Timotijevic, P. Y. Yang, E. J. Teo, M. B. H. Breese, A. A. Bettiol and G. T. Reed, "Silicon photonic waveguides for different wavelength regions," *Semiconductor Science and Technology* vol. 23, no. 6, pp. 064002, 2008.

[136] A. D. Bristow, N. Rotenberg, and H. M. Van Driel, "Two-photon absorption and Kerr coefficients of silicon for $850 - 2200\,\mathrm{nm}$," *Applied Physics Letters* vol. 90, no. 19, pp.191104, 2007.

[137] M. Nedeljkovic, R. Soref, and G. Z. Mashanovich, "Free-carrier electrorefraction and electroabsorption modulation predictions for silicon over the $114\,\mu\mathrm{m}$ infrared wavelength range," *IEEE Photonics Journal* vol. 3, no. 6, pp. 1171–1180, 2011.

[138] K. Ikeda, Y. Shen, and Y. Fainman, "Enhanced optical nonlinearity in amorphous silicon and its application to waveguide devices," *Optics Express* vol. 15, no. 26, pp. 17761–17771, 2007.

[139] P. M. Fauchet, D. Hulin, R. Vanderhaghen, A. Mourchid, and W. L. Nighan, "The properties of free-carriers in amorphous-silicon," *Journal of Non-Crystalline Solids* vol. 141, no. 1-3, pp. 76–87, 1992.

[140] D. J. Won, M. O. Ramirez, H. Kang, V. Gopalan, N. F. Baril, J. Calkins, J. V. Badding, and P. J. A. Sazio, "All-optical modulation of laser light in amorphous silicon-filled microstructured optical fibers," *Applied Physics Letters* vol. 91, pp.161112, 2007.

[141] P. Mehta, N. Healy, T. D. Day, J. R. Sparks, P. J. A. Sazio, J. V. Badding, and A. C. Peacock, "All-optical modulation using two-photon absorption in silicon core optical fibers," *Optics Express* vol. 19, no. 20, pp. 19078-19083, 2011.

[142] B. Kuyken, H. Ji, S. Clemmen, S. K. Selvaraja, H. Hu, M. Pu, M. Galili, P. Jeppesen, G. Morthier, S. Massar, L. K. Oxenlowe, G. Roelkens, and R. Baets, "Nonlinear properties of and nonlinear processing in hydrogenated amorphous silicon waveguides," *Optics Express* vol. 19, no. 26, pp. 146–153, 2011.

[143] C. Grillet, L. Carletti, C. Monat, P. Grosse, B. Ben Bakir, S. Menezo, J. M. Fedeli,and D. J. Moss, "Amorphous silicon nanowires combining high nonlinearity, fom and optical stability," *Optics Express* vol. 20, no. 20, pp. 22609–22615, 2012.

[144] G. W. Rieger, K. S. Virk, and J. F. Young, "Nonlinear propagation of ultrafast 1.5 μm pulses in high-index-contrast silicon-on-insulator waveguides," *Applied Physics Letters* vol. 84, no. 6, pp.900–902, 2004.

[145] X. Sang, E-K. Tien, and O. Boyraz, "Applications of two-photon absorption in silicon," *Journal of Optoelectronics and Advanced Materials* vol. 11, no. 1, pp.15–25, 2008.

[146] R. A. Street, *Hydrogenated Amorphous Silicon* Cambridge University Press, 1991.

[147] J. S. Sanghera, I. D. Aggarwal, L. B. Shaw, C. M. Florea, P. Pureza, V. Q. Nguyen, F. Kung, and I. D. Aggarwal, "Nonlinear properties of chalcogenide glass fibers," *Journal of Optoelectronics and Advanced Materials* vol. 8, no. 6, pp.2148–2155, 2006.

[148] O. Bayraz, T. Indukuri, and B. Jalali, "Self-phase-modulation induced spectral broadening in silicon waveguides," *Optics Express* vol. 12, no. 5, pp. 829–834, 2004.

[149] R. Dekker, A. Driessen, T. Wahlbrink, C. Moormann, J. Niehusmann, and M. Först, "Ultrafast Kerr-induced all-optical wavelength conversion in silicon waveguides using 1.55 μm femtosecond pulses," *Optics Express* vol. 14, no. 18, pp. 8336–8346, 2006.

[150] A. Boskovic, S. V. Chernikov, J. R. Taylor, L. Gruner-Nielsen, and O. A. Levring, "Direct continuous-wave measurement of n2 in various types of telecommunication fiber at 1.55 μm," *Optics Letters* vol. 21, no. 24, pp.1966–1968, 1996.

[151] M. Artiglia, E. Ciaramella, and B. Sordo, "Using modulation instability to determine kerr coefficient in optical fibers," *Electronics Letters* vol. 31, no. 12, pp.1012–1013, 1995.

[152] T. Kato, Y. Suetsugu, M. Takagi, E. Sasaoka, and M. Nishimura, "Measurement of the nonlinear refractive-index in optical-fiber by the cross-phase-modulation

method with depolarized pump light," *Optics Letters* vol. 20, no. 9, pp.988–990, 1995.

[153] R. Hui and M. S. O'Sullivan, *Fiber optic measurement techniques.* Amsterdam ; London: Elsevier/Academic Press, 2009.

[154] H. K. Tsang and Y. Liu, "Nonlinear optical properties of silicon waveguides," *Semiconductor Science and Technology* vol. 23, no. 6, pp.064007, 2008.

[155] A. Cowan, G. Rieger, and J. Young, "Nonlinear transmission of 1.5 μm pulses through single-mode silicon-on-insulator waveguide structures," *Optics Express* vol. 12, no. 8, pp. 1611–1621, 2004.

[156] A. C. Peacock, P. Mehta, P. Horak, and N. Healy, "Nonlinear pulse dynamics in multimode silicon core optical fibers," *Optics Letters* vol. 37, no. 16, pp.3351–3353, 2012.

[157] Q. Lin, J. Zhang, G. Piredda, R. W. Boyd, P. M. Fauchet, and G. P. Agrawal, "Dispersion of silicon nonlinearities in the near infrared region," *Applied Physics Letters* vol. 91, no. 2, pp.021111–021113, 2007.

[158] Q. Lin, O. Painter, and G. Agrawal, "Nonlinear optical phenomena in silicon waveguides: modeling and applications," *Optics Express* vol. 15, no. 25, pp.16604–16644, 2007.

[159] C. Koos, L. Jacome, C. Poulton, J. Leuthold, and W. Freude, "Nonlinear siliconon-insulator waveguides for all-optical signal processing," *Optics Express* vol. 15, no. 10, pp. 5976–5990, 2007.

[160] J. M. Dudley, G. Genty, and S. Coen, "Supercontinuum generation in photonic crystal fiber," *Reviews of Modern Physics* vol. 78, no. 4, pp. 1135–1184, 2006.

[161] J. Safioui, F. Leo, B. Kuyken, S.-P. Gorza, S. K. Selvaraja, R. Baets, P. Emplit, G. Roelkens, and S. Massar, "Supercontinuum generation in hydrogenated amorphous silicon waveguides at telecommunications wavelengths," *Optics Express* vol. 22, no. 3, pp. 3089–3097, 2014.

[162] A. Peacock, "Soliton propagation in tapered silicon core fibers," *Optics Letters* vol. 35, no. 21, pp.3697–3699, 2010.

[163] A. Peacock, "Mid-IR soliton compression in silicon optical fibers and fiber tapers," *Optics Letters* vol. 37, no. 5, pp.818–820, 2012.

[164] X. Gai, D.-Y. Choi, and B. Luther-Davies, "Negligible nonlinear absorption in hydrogenated amorphous silicon at 1.55 μm for ultra-fast nonlinear signal processing," *Optics Express* vol. 22, no. 8, pp. 9948–9958, 2014.

[165] A. Y. H. Chen, G. K. L. Wong, S. G. Murdoch, R. Leonhardt, J. D. Harvey, J. C. Knight, W. J. Wadsworth, and P. St. J. Russell, "Widely tunable optical parametric generation in a photonic crystal fiber," *Optics Letters* vol. 30, no. 7, pp.762–764, 2005.

[166] B. Kuyken, H. Ji, S. Clemmen, S. K. Selvaraja, H. Hu, M. Pu, M. Galili, P. Jeppesen, G. Morthier, S. Massar, L. K. Oxenlwe, G. Roelkens, and R. Baets, "Nonlinear properties of and nonlinear processing in hydrogenated amorphous silicon waveguides," *Optics Express* vol. 19, no. 26, pp. B146–B153, 2011.

[167] N. Vukovic and N. G. R. Broderick, "Method for improving the spectral flatness of the supercontinuum at 1.55 μm in tapered microstructured optical fibers," *Physical Review A* vol. 82, no. 4, pp.043840, 2010.

[168] G. Genty, S. Coen, and J. M. Dudley, "Fiber supercontinuum sources," *Journal of the Optical Society of America B* vol. 24, no. 8, pp.1771–1785, 2007.

[169] L. Yin, Q. Lin, and G. P. Agrawal, "Soliton fission and supercontinuum generation in silicon waveguides," *Optics Letters* vol. 32, no. 5, pp.391–393, 2007.

[170] A. M. Heidt, "Pulse preserving flat-top supercontinuum generation in all-normal dispersion photonic crystal fibers," *Journal of the Optical Society of America B* vol. 27, no. 3, pp.550–559, 2010.

[171] M. Sheik-Bahae, D. C. Hutchings, D. J. Hagan, and E. W. Van Stryland, "Dispersion of bound electron nonlinear refraction in solids," *IEEE Journal of Quantum Electronics* vol. 27, no. 6, pp. 1296-1309, 1991.

[172] S. M. Sze, *Physics of Semiconductor Devices* Wiley, 1981.

[173] B. Jalali, O. Boyraz, D. Dimitropoulos, and V. Raghunathan, "Scaling laws of nonlinear silicon nanophotonics," *Proc. SPIE 5730, Optoelectronic Integration on Silicon II* vol. 5730, pp. 41–51, 2005.

[174] R. Geiger, J. Frigerio, M. J. Sess, D. Chrastina, G. Isella, R. Spolenak, J. Faist, and H. Sigg, "Excess carrier lifetimes in Ge layers on Si," *Applied Physics Letters* vol. 104, no. 6, pp.062106, 2014.

[175] S. Stepanov and S. Ruschin, "Modulation of light by light in silicon-on-insulator waveguides," *Applied Physics Letters* vol. 83, pp.5151, 2003.

[176] D. Seo, J. M. Gregory, L. C. Feldman, N. H. Tolk, and P. I. Cohen, "Multiphoton absorption in germanium using pulsed infrared free-electron laser radiation," *Physical Review B* vol. 83, no. 19, pp. 195203, 2011.

[177] P. Dumon, G. Priem, L. R. Nunes, W. Bogaerts, D. Van Thourhout, P. Bienstman, T. K. Liang, M. Tsuchiya, P. Jaenen, S. Beckx, J. Wouters, and R. Baets,

"Linear and nonlinear nanophotonic devices based on silicon-on-insulator wire waveguides," *Japanese Journal of Applied Physics Part 1-Regular Papers Brief Communications and Review Papers* vol. 45, no. 8B, pp.6589-6602, 2006.

[178] A. C. Turner-Foster, M. A. Foster, J. S. Levy, C. B. Poitras, R. Salem, A. L. Gaeta, and M. Lipson, "Ultrashort free-carrier lifetime in low-loss silicon nanowaveguides," *Optics Express* vol. 18, no. 4, pp. 3582-3591, 2010.

[179] J. Liu, R. Camacho-Aguilera, J. T. Bessette, X. Sun, X. Wang, Y. Cai, L. C. Kimerling, and J. Michel, "Ge-on-Si optoelectronics," *Thin Solid Films* vol. 520, no. 8, pp. 3354–3360, 2012.

[180] T. K. Liang, H. K. Tsang, I. E. Day, J. Drake, A. P. Knights, and M. Asghari, "Silicon waveguide two-photon absorption detector at 1.5 μm wavelength for autocorrelation measurements," *Applied Physics Letters* vol. 83, pp.1323-1325, 2002.

[181] A. M. Heidt, Z. Li, J. Sahu, P. C. Shardlow, M. Becker, M. Rothhardt, M. Ibsen, R. Phelan, B. Kelly, S. U. Alam, and D. J. Richardson, *Optics Letters* vol 38, pp. 1615-1617 (2013).

[182] D. J. Moss, L. Fu, I. Littler, and B. J. Eggleton, "Ultrafast all-optical modulation via two-photon absorption in silicon-insulator waveguide," *Electron Letters* vol. 41, no. 10, pp. 320-321 , 2005.

[183] T. K. Liang, L. R. Nunes, T. Sakamoto, K. Sasagawa, T. Kawanishi, M. Tsuchiya, G. R. A. Priem, D. Van Thourhout, P. Dumon, R. Baets, and H. K. Tsang, "Ultrafast all-optical switching by cross-absorption modulation in silicon wire waveguides," *Optics Express* vol. 13, no. 24, pp. 7298-7303 , 2005.